

Design and Implementation of an Integrated Solar Panel Antenna for Small Satellites

Vernon Pete Davids
(Author)

**Dissertation submitted in fulfilment of the requirements for the degree
Doctor of Engineering in Electrical Engineering
in the Faculty of
Engineering and Built Environment
at the
Cape Peninsula University of Technology
(Bellville, South Africa)**

December 2019

Prof Robert Lehmensiek
(Supervisor)

CPUT copyright information

The dissertation/thesis may not be published either in part (in scholarly, scientific or technical journals), or as a whole (as a monograph), unless permission has been obtained from the University

Declaration

I, Vernon Pete Davids, declare that the contents of this dissertation represent my own unaided work, and that the dissertation has not previously been submitted for academic examination towards any qualification. Furthermore, it represents my own opinions and not necessarily those of the Cape Peninsula University of Technology.



Vernon Pete Davids

Date: 27 February 2020

Research outputs from this dissertation are:

- Davids, V. & Lehmensiek, R. 2014. The effects of a triple-junction solar cell on a dielectric resonator antenna. *Proceedings of the 8th European Conference on Antennas and Propagation (EuCAP)*, The Hague, Netherlands, 6–11 April 2014, The institute: 2928–2931.
- Davids, V. & Lehmensiek, R. 2016. A beam steerable back-to-back Yagi-Uda dielectric resonator antenna array. *Proceedings of the 10th European Conference on Antennas and Propagation (EuCAP)*, Davos, Switzerland, 10–15 April 2016, The institute: 1–4.
- Davids, V. P. & Lehmensiek, R. 2019. A steerable dielectric resonator antenna array with isoflux radiation pattern. *Microwave and Optical Technology Letters*, 61(10): 1–8.

Abstract

This dissertation presents a concept for a compact, low-profile, integrated solar panel antenna for use on small satellites in low Earth orbit. To date, the integrated solar panel antenna design approach has primarily been, patch (transparent or non-transparent) and slot radiators. The design approach presented here is proposed as an alternative to existing designs. A prototype, comprising of an optically transparent rectangular dielectric resonator was constructed and can be mounted on top of a solar panel of a Cube Satellite. The ceramic glass, LASF35 is characterised by its excellent transmittance and was used to realise an antenna which does not compete with solar panels for surface area.

Currently, no closed-form solution for the resonant frequency and Q-factor of a rectangular dielectric resonator antenna exists and as a first-order solution the dielectric waveguide model was used to derive the geometrical dimensions of the dielectric resonator antenna. The result obtained with the dielectric waveguide model is compared with several numerical methods such as the method of moments, finite integration technique, radar cross-section technique, characteristic mode analysis and finally with measurements. This verification approach was taken to give insight into the resonant modes and modal behaviour of the antenna. The interaction between antenna and a triple-junction gallium arsenide solar cell is presented demonstrating a loss in solar efficiency of 15.3%. A single rectangular dielectric resonator antenna mounted on a ground plane demonstrated a gain of 4.2 dBi and 5.7 dBi with and without the solar cell respectively. A dielectric resonator antenna array with a back-to-back Yagi-Uda topology is proposed, designed and evaluated. The main beam of this array can be steered can steer its beam ensuring a constant flux density at a satellite ground station. This isoflux gain profile is formed by the envelope of the steered beams which are controlled using a single digital phase shifter. The array achieved a beam-steering limit of $\pm 66^\circ$ with a measured maximum gain of 11.4 dBi.

The outcome of this research is to realise a single component with dual functionality satisfying the cost, size and weight requirements of small satellites by optimally utilising the surface area of the solar panels.

Keywords: integrated solar panel antenna, dielectric resonator antenna, transparent antenna, small satellites, beam-steering, Yagi-Uda array.

Dedication

In loving memory of my nephew

Darren Rhoda

27/12/2000 – 25/01/2016

Acknowledgements

This dissertation was completed under challenging circumstances and was made possible through the support of others. For this, I am exceedingly grateful and would like to acknowledge the contributions and support of:

- Prof Robert Lehmensiek (EMSS Antennas/CPUT/F'SATI) for his mentorship, intuitive discussions and trust. I am especially grateful for his patience and understanding.
- Prof Robert van Zyl (CPUT/F'SATI) and F'SATI for their financial assistance.
- My mother for her friendship, support and late-night coffees. My sister for her, sometimes excessive love. The rest of my family and friends for their love and moral support throughout my career.
- Dr Martin Letz (SCHOTT AG) for his help and discussions regarding ceramic glass as well as sponsoring the samples.
- Anneke Bester (Stellenbosch University) for assisting me with measurements.
- Dr Sias Mostert for his unorthodox way of encouragement by asking me daily "*Is die PhD al ingehandig?*" The Space Advisory Company for sponsoring the triple-junction solar cells as well as NewSpace Systems for the use of their clean room facilities.
- Susan Maas for always assisting in solutions to practical problems especially through organising the use of Stellenbosch University's CST MWS software.
- Mr Whaits and his technicians for assisting me with measurements and the use of the laboratory.
- Lastly my wife Dr Melissa Boonzaaier, thank you for your selfless support through the completion of my doctoral studies, amidst the completion of yours. I love you immensely.

Contents

Declaration	i
Abstract	ii
Dedication.....	iii
Acknowledgements.....	iv
Contents	v
Abbreviations.....	xi
Chapter 1 Introduction	1
1.1 Antenna concepts for solar panel integration.....	2
1.2.1 Integrated Solar Panel Antennas	2
1.2.2 Transparent Antennas.....	3
1.2.3 Dielectric Resonator Antennas.....	3
1.2.4 Transparent DRAs	5
1.2 About the Dissertation	6
1.3 Delineation	8
1.4 Layout of the Dissertation.....	8
Chapter 2 Theory of the Rectangular DRA.....	9
2.1 Introduction	9
2.2 Electric Polarization.....	10
2.3 Rectangular Dielectric Resonator.....	13
2.4 Dielectric Waveguide Model	14
2.5 Radiation Model and Q-factor.....	19
2.6 Conclusion	22
Chapter 3 Theoretical and Experimental Results	23
3.1 Introduction	23
3.2 Isolated Rectangular DRA in free-space.....	23
3.2.1 Isolated Dielectric Cube	24
3.3 Rectangular DRA on a ground plane	26
3.3.1 Probe Coupling.....	27
3.4 Characteristic Mode Analysis	29
3.5 Conclusion	35
Chapter 4 Integrated Solar Panel Antenna.....	36
4.1 Introduction	36
4.2.1 GaAs triple-junction Solar Cells	37
4.2 Effects of a GaAs Solar Cell on DRA.....	37
4.2.2 Parametric Study of the Solar Cell	37

4.2.3	Triple-junction Solar Cell Analysis	39
4.2.4	Single rectangular DRA measurements	42
4.3	Effects of the DRA on a GaAs Solar Cell	45
4.4	Conclusion	49
Chapter 5 A Beam-Steerable Back-to-Back Yagi-Uda DRA Array		50
5.1	Introduction	50
5.2	Antenna Coverage Pattern and Gain Requirement	50
5.3	Design Methodology	52
5.4	DRA Array Design	55
5.4.1	Optimisation of the Geometrical Parameters and Excitations	56
5.4.2	Design and Optimisation of the Impedance Matching Network	59
5.4.3	Mutual Coupling.....	62
5.4.4	Finite ground effects	64
5.4.5	Beam-Steering and Control	64
5.5	DRA Array Measured Results.....	65
5.6	Conclusion	68
Chapter 6 Conclusions and Recommendations		69
6.1	Responses to Research Questions	70
6.2	Recommendations	71
6.3	Future Work	71
Bibliography.....		72
Appendix A : Arduino Beam-Steering Sketch.....		79
A.1	maps_6bit	79

List of figures

Figure 1.1: Proposed ISPA concept (not to scale). (a) Probe-fed DRA on solar cell side view (b) Probe-fed DRA on solar cell top view	7
Figure 2.1: Rectangular DRA with probe feed	9
Figure 2.2: Macroscopic model of a dielectric showing electric polarization (a) $\vec{E} = 0$ and (b) $\vec{E} \neq 0$	10
Figure 2.3: Isolated rectangular DRA	13
Figure 2.4: Infinite rectangular dielectric waveguide	15
Figure 2.5: Cross-sectional field distribution of the rectangular dielectric waveguide	15
Figure 2.6: Resonant frequency of an isolated rectangular DRA for different aspect ratios and height, $b = 9$ mm	18
Figure 2.7: $TE_{11\delta}^z$ modal fields for the isolated rectangular DRA	19
Figure 2.8: Radiation Q-factor of an isolated rectangular DRA for different aspect ratios and height, $b = 9$ mm	20
Figure 3.1: RCS for an isolated rectangular DRA in free-space with a z -axis polarized incident plane wave. The scattered radiation pattern cuts for the $TE_{1\delta 1}^y$ mode are shown	24
Figure 3.2: The scattered electric field configuration in the xz -plane at $y = 0$ for the $TE_{1\delta 1}^y$ mode of an isolated rectangular DRA in free-space	24
Figure 3.3: RCS of the cubic DRA	25
Figure 3.4: Simulated $ S_{11} $ for the rectangular DRA on a ground plane	26
Figure 3.5: Electric field in the xz -plane at $y = 0$ for the $TE_{1\delta 1}^y$ mode of a rectangular DRA ...	26
Figure 3.6: Rectangular DRA on a finite ground plane with probe exciting the $TE_{\delta 1 1}^x$	27
Figure 3.7: Input reflection coefficient for the rectangular DRA fed with a coaxial probe positioned at different locations along the x -axis	28
Figure 3.8: Input reflections coefficient for a strip-fed rectangular DRA with various heights above an infinite ground plane	28
Figure 3.9: Eigenvalues for the candidate rectangular DRA on an infinite PEC ground plane	30
Figure 3.10: Modal significance of the candidate rectangular DRA on an infinite PEC ground plane	31
Figure 3.11: Characteristic angles for the candidate rectangular DRA on an infinite PEC ground plane	33
Figure 4.1: FEKO model of the rectangular DRA on top of a GaAs solar cell on an infinite PEC ground plane (Davids & Lehmsiek, 2014)	36
Figure 4.2: Resonant frequency for a rectangular DRA on top of a homogeneous solar cell model with various permittivity and thicknesses	38

Figure 4.3: Resonant frequency for a rectangular DRA on top of a homogeneous solar cell with the CMX and CMG coverglass types of various thicknesses	38
Figure 4.4: Cross-section of the transparent rectangular DRA on top of a triple-junction solar cell (Not to scale).....	39
Figure 4.5: Simulated $ S_{11} $ for a rectangular DRA placed on a GaAs solar cell without metallic contacts and on an infinite ground plane.....	40
Figure 4.6: Simulated $ S_{11} $ for a rectangular DRA placed on a GaAs solar cell with metallic contacts and on an infinite ground plane.....	40
Figure 4.7: Simulated surface currents of the rectangular DRA placed on top of a GaAs solar cell (top view).....	40
Figure 4.8: Simulated radiation pattern of the rectangular DRA, placed on an infinite ground plane (solid line) and placed on an infinite ground plane on top of a GaAs solar cell (dashed line). $\phi = 0^\circ$	41
Figure 4.9: Simulated radiation pattern of the rectangular DRA, placed on an infinite ground plane (solid line) and placed on an infinite ground plane on top of a GaAs solar cell (dashed line). $\phi = 90^\circ$	41
Figure 4.10: Single transparent DRA on top of a GaAs solar cell without electrical connections.....	42
Figure 4.11: $ S_{11} $ for a rectangular DRA placed on a GaAs solar cell on a 150 mm x 150 mm x 2.5 mm aluminium ground plane	43
Figure 4.12: Simulated and measured E-plane at 5.6 and 5.8 GHz, respectively, for the single rectangular DRA placed on a 150 mm x 150 mm x 2.5 mm aluminium ground plane ground. Without the GaAs solar cell (solid line) and with the GaAs solar cell (dash-dot line) between the DRA and ground plane	43
Figure 4.13: Simulated and measured H-plane at 5.6 and 5.8 GHz, respectively, for the single rectangular DRA placed on a 150 mm x 150 mm x 2.5 mm aluminium ground plane ground. Without the GaAs solar cell (solid line) and with the GaAs solar cell (dash-dot line) between the DRA and ground plane	44
Figure 4.14: Realised gain of the rectangular DRA placed on top of a 150 mm x 150 mm x 2.5 mm aluminium ground plane for the TE_{101}^y mode	44
Figure 4.15: Efficiencies of the GaAs solar cell vs transmittance of candidate glass types..	45
Figure 4.16: Solar cell efficiency test circuit.....	46
Figure 4.17: Solar cell efficiency test setup	47
Figure 4.18: Measured current and voltages of the GaAs solar cell, with and without the DRA; Case I: without DRA (solid line) and Case II: without DRA (dashed line).	47
Figure 4.19: Power output of the GaAs solar cell with and without the DRA; Case I: without DRA (solid line) and Case II: without DRA (dashed line)	48
Figure 5.1: Satellite link path with required radiation pattern relative to the ground station..	51
Figure 5.2: Required gain and slant range over elevation angle for a satellite in a 600 km orbit	52
Figure 5.3: Geometrical configuration of the back-to-back Yagi-Uda DRA array (Davids & Lehmensiek, 2016)	54
Figure 5.4: Top view of the fabricated back-to-back DRA array showing the DRA elements	55
Figure 5.5: Bottom view of the fabricated back-to-back DRA array.....	55
Figure 5.6: Optimisation algorithm for the back-to-back DRA array (Davids & Lehmensiek, 2019)	57

Figure 5.7: Simulated excitation phase angles of the back-back Yagi-Uda DRA array over all pointing angles	58
Figure 5.8: FEKO simulated $E_{(xz)}$ -plane of the back-to-back Yagi-Uda DRA array for different excitation angles, $\angle V_2$	59
Figure 5.9: CST MWS simulated $E_{(xz)}$ -plane of the back-to-back Yagi-Uda DRA array for different excitation angles, $\angle V_2$	59
Figure 5.10: Matching network topology.....	60
Figure 5.10: Input impedance over all excitation angles of the unmatched and matched Yagi-Uda DRA array at 5.6 GHz.....	61
Figure 5.11: Predicted mismatch loss over all excitation angles of the unmatched and matched Yagi-Uda DRA array at 5.6 GHz	61
Figure 5.12: Mutual coupling between E-plane and H-plane rectangular DRA elements	63
Figure 5.13: FEKO simulated $E_{(xz)}$ -plane of the H-plane configured back-to-back Yagi-Uda DRA array for different excitation angles, $\angle V_2$	63
Figure 5.14: Simulated $E_{(xz)}$ -plane for the back-to-back Yagi-Uda DRA array on top of different ground plane sizes	64
Figure 5.15: Measurement setup of the back-to-back Yagi-Uda DRA array in the rectangular anechoic chamber at the Stellenbosch University	66
Figure 5.16: Measured input reflection coefficient of the back-to-back Yagi-Uda DRA array over the full range of excitation phase angles	66
Figure 5.17: Measured gain in the $E_{(xz)}$ -plane of the back-to-back Yagi-Uda DRA array over the full range of excitation phase angles	67
Figure 5.18: Maximum achievable gain, G_{env} , of the back-to-back Yagi-Uda DRA and required gain, G_{req} . Also shown are the measured gain patterns for the excitation angles $\angle V_2 = [157.5^\circ, 247.5^\circ, 292.5^\circ, 106.9^\circ]$ corresponding to the beam-pointing angles $\theta_p = [0^\circ, 22^\circ, 44^\circ, 66^\circ]$	68
Figure A.1: Arduino UNO rev3 microcontroller board	79

List of tables

Table 2.1: Dimensions and Q-factor for the candidate isolated rectangular DRA.....	22
Table 3.1: Simulated resonance frequency, radiating bandwidth and quality factor of the first four modes of the candidate rectangular DRA	32
Table 3.2: Modal fields and radiation patterns for the candidate rectangular DRA on an infinite PEC ground plane	34
Table 3.3: Comparison of the simulated and measured rectangular DRA fundamental mode	35
Table 4.1: Load resistor values used to measure the I-V curve	46
Table 4.2: Measured Electrical Parameters of GaAs solar cell with and without DRA.....	48
Table 5.1: Relationship between the orbital parameters for a satellite in a 600 km orbit	52
Table 5.2: Geometrical dimensions of the DRA Yagi-Uda array.....	58
Table 5.3: Geometrical dimensions of the optimised impedance matching network	60
Table 5.4: Summary of the scanning performance of the back-to-back Yagi-Uda DRA array	67

Abbreviations

Abbreviations	Definition
μm	Micrometer
ACA	Active Collective Area
BFGS	Broyden-Fletcher-Goldfarb-Shanno
CMA	Characteristic Mode Analysis
CMS	Cerium Doped Glass
CMX	Cerium Dioxide Glass
CP	Circularly Polarised
CST	Computer Simulation Technology
dB	Decibel
dBi	Decibel Isotropic
DR	Dielectric Resonator
DRA	Dielectric Resonator Antenna
DWM	Dielectric Waveguide Model
EM	Electromagnetic
ESPAR	Electronically Steerable Parasitic Array Radiator
eV	Electron Volt
F'SATI	French South African Institute of Technology
FDTD	Finite-Difference Time-Domain
FEKO	<i>Feldberechnung für Körper mit beliebiger Oberfläche</i>
FEM	Finite Element Method
FF	Fill Factor
FIT	Finite Integration Technique
FR4	Flame Retardant glass-reinforced epoxy laminate PCB material
FTO	Fluorine-doped Tin Oxide
GaAs	Gallium Arsenide
GaInP	Gallium Indium Phosphide
Ge	Germanium
GHz	GigaHertz
IDE	Integrated Development Environment
ISPA	Integrated Solar Panel Antenna
ITO	Indium Tin Oxide
LEO	Low Earth Orbit
Mbps	Megabit per second
MEMS	MicroElectroMechanical System
MoM	Method of Moment

MWS	Microwave Studio
PBIL	Population Based Incremental Learning
PCB	Printed Circuit Boards
PEC	Perfect Electrical Conductor
P-POD	Poly-Picosatellite Orbital Deployer
RCS	Radar Cross-Section
RF	Radio Frequency
SEP	Surface Equivalence Principle
SMA	Sub-miniature version A
SmallSat	Small Satellite
SOLANT	SOLar ANTenna
TCM	Theory of Characteristic Modes
TE	Transverse Electric
TM	Transverse Magnetic
TT&C	Telemetry, Tracking & Command
U	Unit
UHF	Ultra High Frequency
V	Voltage
VEP	Volume Equivalence Principle
VHF	Very High Frequency
WLAN	Wireless Local Area Network

Chapter 1 Introduction

Technological advancements amid decreasing space programme budgets fuel the miniaturisation of spacecraft. The trend in space missions has evolved to consider low-cost smaller satellites, employed in constellations, over traditional single satellite missions (Hodges et al., 2017). A direct consequence of this miniaturisation trend resulted in the development of the modular CubeSat with the fundamental cubic unit of dimensions 10 cm x 10 cm x 10 cm and mass less than 1.33 kg (1U). CubeSats can be combined to form larger CubeSats and in this dissertation a 1U and 3U (30 cm x 10 cm x 10 cm) CubeSat are considered as case-studies. Furthermore, CubeSats and their payloads are rapidly increasing in complexity demanding higher data-rates for both Telemetry, Tracking & Command (TT&C) and payload communication links. This driving requirement has led to the development of spectral efficient S- and X-band transceivers capable of data rates up to 100 Mbps (Issler et al., 2014). For satellite communication links, antennas supporting these data rates require wide radiation pattern coverage, with moderate to high gain. Furthermore, strict space constraints on CubeSats make frequencies above S-band attractive for compact, multipurpose, low-profile antennas.

The main motivation for this research is to compliment the miniaturisation trends of satellites and the need to satisfy their low cost, communication, size and power requirements. This is accomplished by integrating two system components (i.e., a solar panel and antenna) into one presenting a low-profile assembly with dual functionality. The antenna was designed to operate in the amateur C-band (4 GHz to 8 GHz). The effect of a triple-junction solar cell on the antenna's performance was investigated numerically using full-wave Electromagnetic (EM) analyses, making extensive use of FEKO (Altair, n.d). Throughout the dissertation, validation of the results was accomplished through measurements or through an alternative numerical technique using CST Microwave Studio (CST Microwave studio, n.d). In the final chapter a back-to-back Yagi-Uda Dielectric Resonator Antenna (DRA) array capable of maximizing the contact time between a satellite in Low Earth Orbit (LEO) and a ground station is presented. The array utilises mutual coupling to aid in beam-steering between the broadside and end-fire direction. This array is intended for an Integrated Solar Panel Antenna (ISPA) concept and utilises the satellite-face which points towards earth as the mounting face for an ISPA. Solar panels typically are mounted on a satellite's surfaces which points towards the sun. It is proposed that the four ISPAs be mounted, one on each face of a small satellite

(such as a 3U). In this manner a spacecraft spinning around its roll-axis can maintain communication with any one of the ISPA's. This research holds exciting possibilities for future small satellites by proposing a compact multi-functional antenna.

1.1 Antenna concepts for solar panel integration

In the past, numerous antennas for modern small satellites have been developed (Gao et al., 2009). These conventional antenna elements are impractical on-board CubeSats due to space mission drivers such as strict space and weight limitations. Furthermore, the size and number of sensors and antennas mounted on a satellite are limited since the satellite's available power is dictated by maximizing the surface area of the solar panels. A solution is to use multi-purpose antennas. Lehmsiek (2012) demonstrated a multi-purpose shuttlecock antenna which utilises the physical structure of a nano-satellite's aerodynamic attitude-stabilization system. The structure is deployable and thus imposes the risk, as with all deployable antennas, of total mission failure should the deployment mechanism malfunction. A comprehensive review on recent antenna developments for Small Satellite (SmallSat) applications is given in Gao et al. (2018). Majority of these developments are deployable antennas with increased mechanical complexity. A good compromise between complexity and Radio Frequency (RF) performance are multi-purpose, low-profile antennas integrated with solar panels.

1.2.1 Integrated Solar Panel Antennas

The ISPA concept was first demonstrated by Tanaka et al. (1995) which mounted solar cells around and on top of a microstrip patch radiator. Subsequently, a space-qualified SOLar ANTenna (SOLANT) was demonstrated by Vaccaro et al. (2009) by demonstrating a 38.41 mm thick planar array of slot radiators. A similar design approach was applied to a CubeSat solar panel by Mahmoud (2010) and later by Fawole (2012). More compact assemblies are possible by replacing slot radiators with microstrip patch radiators (Vaccaro et al., 2000). To date, the ISPA approach has primarily been patch (transparent or non-transparent) and slot radiators arranged around, above or below solar cells with the main challenge being the complexity and cost of the assembly as well as the interference of the solar cells with the antenna performance and *vice versa*.

The ultimate level of integration can be attained when making the solar cell the radiator itself. Bendel et al. (2003) demonstrated this concept by exciting Polycrystalline solar cells with an aperture slot. To date, single-junction, polycrystalline solar cells have progressed to more advanced, multi-junction GaAs solar cells. These solar cells utilise multiple semiconductors configured according to their band gap energies to maximise the absorption of photons within

the light spectrum. GaAs cells are more efficient than Polycrystalline cells, but also more costly. The use of GaAs solar cells as an antenna element is yet to be investigated.

Another integration approach is to print antennas using conductive inks directly onto the solar panel's coverglass or transparent substrates placed on top of the solar panel. These integration methods produce shadowing and consequently limit the overall system efficiency. To overcome these challenges a solution is to use transparent antennas.

1.2.2 Transparent Antennas

For transparent patch antennas, two dominant methodologies are used, those made from transparent films and those constructed from meshed metallic surfaces (Yasin & Baktur, 2013). The transparent films most widely used include Indium Tin Oxide (ITO) and Fluorine-doped Tin Oxide (FTO) (Guan et al., 2007). Saberlin and Furse (2010) discussed the challenges of transparent antennas for use on small satellite solar panels. These challenges are related to achieving an optimum balance between sheet resistivity (related to radiation efficiency) and optical transparency (related to solar cell efficiency). To date, transparency limits for solar panel integration applications remain approximately at 90% (Yekan & Baktur, 2017). Concurrently, significant strides have been made in the field of nanotechnology and material science with the evolution of Graphene and its applications due to its promising optical, electrical and mechanical properties. Already this material was proposed as an alternative for transparent conductive films (Wu & Hao, 2014). The cost of Graphene currently does not warrant their use on CubeSat missions and was thus not considered at the commencement of this work. The approach in this dissertation is to find a suitable transparent dielectric material for realising a transparent DRA which also meet the design specifications.

1.2.3 Dielectric Resonator Antennas

The antennas mentioned above are metallic and at millimetre-wave frequencies conductor losses reduces the antenna efficiency due to skin effects. An antenna which does not suffer from conductor losses nor surface waves is the DRA. The DRA concept was first discussed by Richtmyer (1939) and demonstrated later by Gastine et al. (1967). A DRA is made of a high dielectric, low loss material and can take nearly any geometry with the most common being rectangular, cylindrical and hemispherical. Practically, the DRA is mounted on top of a ground plane and can accommodate various feeding mechanisms such as the coaxial probe, aperture-coupling, microstrip feedline and conformal strip (Luk & Leung, 2003). Advantages of the DRA include its small size, high radiation efficiency (by using low loss dielectric materials), wide bandwidth and the ability to obtain different radiation characteristics (by exciting different resonant modes).

Petosa and Ittipiboon (2010) gave a comprehensive review of the DRA with other excellent reviews by Mongia et al. (1994) and Petosa et al. (1998) which examined compact, wideband, low-profile, Circularly Polarised (CP) and high gain designs. Important requirements to consider for solar panel integration are DRAs with small size and moderate gain.

A simple technique to reduce a DRA's size is to use dielectric materials with a high dielectric constant (ϵ_r) since the physical size is proportional to $\epsilon_r^{-1/2}$ (Kishk & Huang, 2011). Accordingly, the impedance bandwidth is narrowed as since the Q-factor is directly proportional to the $\epsilon_r^{3/2}$ (Huynh et al., 2010). Kishk and Huang (2011) demonstrated size reduction techniques by exploiting symmetries found in the internal modal field configurations using either a finite electric conductor or finite magnetic conductor. The result is a bisected DRA with the same mode configuration and resonant frequency as the original sized DRA. This method is impractical for solar cell integration due to the non-transparency of the conducting planes needed. Transparent films or Graphene mentioned in section 1.2.2 could be utilised when pursuing this approach.

Other methods of size reduction include DRAs exploiting fractal (Semouchkina et al., 2002), tetrahedron, triangle (Kishk, 2002) and supershaped geometries (Simeoni et al., 2009), but these suffer from high fabrication costs. Many low-profile DRAs are of the multi-segment type, which increases the impedance bandwidth by introducing multiple resonances (Petosa et al., 1999). A thin segment of high ϵ_r is sandwiched between a ground plane and another segment with lower ϵ_r . Other multi-resonant methods include exciting two modes within the DRA (De Young & Long, 2006) or coupling to parasitic elements such as patch antennas (Coulibaly et al., 2008). Coulibaly et al. (2008) demonstrated an X-band DRA combined with a patch antenna achieving an overall assembly height of 4.61 mm and a bandwidth of 50%. These stacked designs, as a candidate topology, are still not as low profile. In addition, the lack of structural integrity imposes fabrication challenges.

Petosa and Thirakoune (2011) demonstrated a method of increasing the gain of a rectangular DRA by exciting and operating at higher-order modes. A gain of 10.2 dBi was reported operating at the $TE_{\delta 11}^x$ mode for a DRA height of 30 mm at 11 GHz. Higher order modes inherently exhibit narrow beamwidths and an increase in physical size. Nasimuddin and Esselle (2007) demonstrated a low-profile antenna comprising of a cross DRA on top of a microstrip patch with both elements placed inside a surface mounted short horn. A gain greater than 9 dBi was reported for an assembly with dimensions 8.61 mm \times 48.1 mm \times 43.1 mm. The DRA is a suitable candidate for antenna arrays due to its compact size,

average gain and favourable radiation modes (Kajfez & Kishk, 2002). For array designs, mutual coupling is important due to its effects on the antenna performance. Mutual coupling depends on the geometry and dimensions of the DRA elements, element spacing, number of elements, mode of operation and the feed arrangement (Luk & Leung, 2003). An advantage of DRA arrays over microstrip patch arrays is that the element spacing can be smaller than that of patch arrays. This gives rise to more compact array designs (Petosa et al., 1999).

The EM characteristics of DRAs are thus favourable as a candidate for an ISPA. Optical transparency is thus the only remaining requirement and a transparent dielectric material with high ϵ_r is necessary to construct a transparent DRA.

1.2.4 Transparent DRAs

Lim and Leung (2010) first proposed the concept of placing a transparent DRA on top of a solar cell. A transparent hemispherical and a rectangular DRA made of Borosilicate Crown K-9 (Pyrex) glass mounted on top of a solar cell was demonstrated. The antenna provides 4 dB more gain than existing transparent microstrip antennas. Since the authors have remained the main contributors of research into transparent DRAs (Leung et al., 2012). Examples of these contributions are aesthetic in nature such as a decorative glass swan and apple DRA as well as a dual-function glass DRA for use as a light cover (Leung et al., 2013). To achieve CP, inclined parasitic copper strips were placed on the walls of the DRA to perturb the fields. A transparent CP design was demonstrated using ITO coated transparent patches. Due to the losses associated with ITO, discussed in section 1.2.2, the antenna gain and efficiency were compared with that of a DRA with regular copper patches. The gain for the DRA with copper patches and DRA with ITO patches was ~ 2 dBi and ~ 1 dBi, respectively. The efficiency for the DRA with copper patches and DRA with ITO patches was 85% and 67%, respectively.

For wideband designs the multiple resonant technique, mentioned in section 1.2.3, for non-transparent DRAs was used by Fang and Leung (2014) and more recently by Sun et al. (2015). A dual band compact (12 mm x 12 mm x 5.1 mm) DRA was realised using a high dielectric, low loss, transparent glass (Mehmood et al., 2014). Dual band operation was achieved by using a T-shaped microstrip feed. To achieve a more compact design a dielectric with an even higher ϵ_r can be used. A similar design approach to the one presented in this dissertation was published by Rashidian et al. (2014). The authors proposed machining a transparent DRA out of a transparent acrylic sheet which is mounted on top of a solar cell serving as a protective layer. The antenna operates at Ku-Band and Wireless Local Area Network (WLAN) applications. The properties of acrylic that outweigh those of ceramic glass as a DRA are overshadowed by its low ϵ_r . This makes the size of a DRA made from acrylic

below 10 GHz impractical. To overcome this, Rashidian et al. (2014) used two conducting planes on the top and front face of the DRA (exploiting the internal field configuration) to make the antenna operate at 5.8 GHz. In this dissertation, the ϵ_r of the proposed material is sufficiently high to realise a low-profile antenna that meets the specifications of a launch vehicle of CubeSats (CubeSat Design Specification, 2014).

1.2 About the Dissertation

As mentioned in section 1.2.1, the mechanical requirements for CubeSats restrict the use of conventional antenna elements. This is partly due to the deployment mechanism called a Poly-Picosatellite Orbital Deployer (P-POD), which limits the height (from the satellite's surface) of all sensors, including antennas, to a maximum height of 6.5 mm (CubeSat Design Specification, 2014). The maximum height of the candidate antenna was determined by analysing a commercial off-the-shelf solar panel. The combined height of a CubeSat solar panel (standard FR4 PCB material included) with coverglass is 2 mm in total which gives the candidate DRA a restricted height of 4.5 mm. To allow for maximum design flexibility, a rectangular DRA was chosen. The characteristics of rectangular DRAs will be discussed later in this dissertation. Three candidate transparent dielectric materials were considered and are Borosilicate K9 (Pyrex), Sapphire and LASF35. The combination of using a high dielectric material (LASF35) and operating in the C-Band makes this attempt more feasible than previous reported DRA and solar cell integration attempts (Lim & Leung, 2010). The main concept is to mount the transparent DRA on top of the solar cell's coverglass (illustrated in Figure 1.1) which is fed by means of a coaxial probe. This is the first time that the LASF35 glass is proposed as a DRA for solar panel integration on SmallSat missions. To evaluate the antenna without the solar panel, it is mounted directly on top of an aluminium ground plane representing the face of a CubeSat.

The following research questions apply to this topic:

- Is it feasible to integrate a transparent DRA with a solar panel of a CubeSat to obtain a low-profile, lightweight, moderate gain antenna?
- What transparent dielectric material is most suitable as the DRA element?
- What effect does the solar panel have on the antenna performance?
- What effect does the antenna have on the solar panel?

The main contribution of this dissertation is to further complement the miniaturisation trends of SmallSats by proposing to combine two system components. These system components are solar panels and antennas. The antenna has no deployment mechanism and therefore reduce the risk of deployment failure. Other favourable characteristics are being low-profile, lightweight whilst maximising a SmallSat's power capabilities.

To further increase the communication capabilities of SmallSats a DRA array is proposed and demonstrated. This array has a back-to-back Yagi-Uda topology and can steer its beam ensuring a constant flux density at a satellite ground station. This isoflux gain profile is formed by the envelope of the steered beams which are controlled using a single digital phase shifter. The array achieved a beam-steering limit of $\pm 66^\circ$ with a measured maximum gain of 11.4 dBi.

This project contributes and expands the existing antenna developments (at S- and X-band) at the French South African Institute of Technology (F'SATI). The proposed antenna can easily be scaled to higher frequency bands, such as X-band, and will produce a more compact antenna.

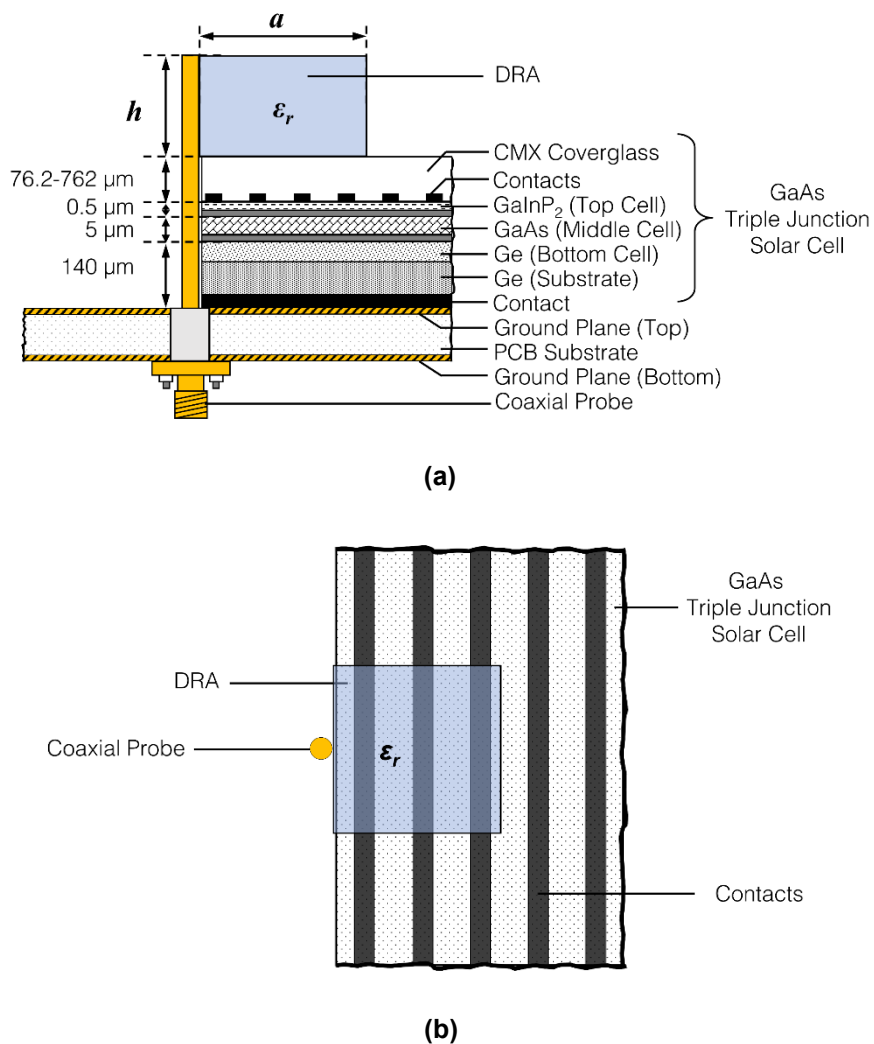


Figure 1.1: Proposed ISPA concept (not to scale). (a) Probe-fed DRA on solar cell side view (b) Probe-fed DRA on solar cell top view

1.3 Delineation

This research will only consider:

- Triple-junction GaAs solar cells.
- RF frequencies within the C-band, defined as 4 GHz – 8 GHz.
- The spectrum of light between 300 – 1900 nm considered for the solar cell operation, as well as the cover glass' transparency.
- Rectangular DRAs.
- A SmallSat in LEO, such as a nadir pointing 3U CubeSat.

1.4 Layout of the Dissertation

Chapter 1 introduced the research study and gave a brief background of the research problem. The theory of the rectangular DRA is discussed in Chapter 2 and discuss the popular Dielectric Waveguide Model (DWM). This analytical result is compared with numerical results, supplemented with measurements in Chapter 3. The proof of concept ISPA is detailed in Chapter 4. Numerical studies were performed to predict the effects of the solar cell on the DRA and vice versa. Chapter 5 involves the design and measurement results of a beam steerable back-to-back DRA array. Beam-steering is achieved using a combination of electromagnetic coupling and digital phase shifters. Finally, Chapter 6 consists of the findings, concluding remarks and recommendations.

Chapter 2 Theory of the Rectangular DRA

2.1 Introduction

Using a dielectric material of high ϵ_r and low loss, a DRA can take nearly any geometric shape. The most common and simplest geometries are rectangular, cylindrical and hemispherical DRAs. The rectangular DRA can be characterised by its width, a , depth d , height h and ϵ_r . Practically the rectangular DRA is typically mounted on top of a ground plane (see Figure 2.1). For an isolated (in free-space) rectangular DRA the ground plane is removed and the height becomes $b = 2h$. Different feeding arrangements are possible and include the coaxial probe, aperture coupling, microstrip feedline, co-planar feed, slotline, stripline and conformal strip (Luk & Leung, 2003).

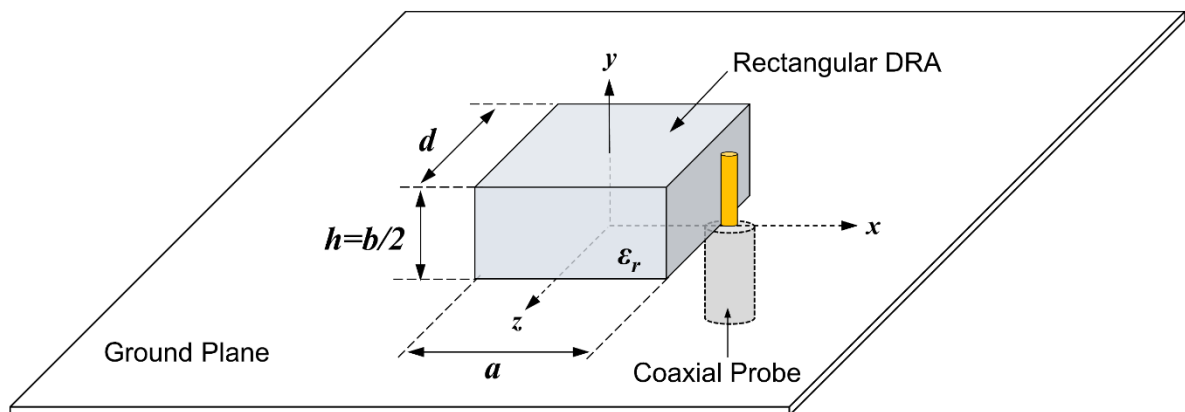


Figure 2.1: Rectangular DRA with probe feed

Theoretically, the resonant modes of spherical and cylindrical DRAs are well understood with that of the rectangular DRA still remaining to be both ambiguous and approximated. In contrast with its simple geometry, the rectangular DRA represents a complex EM boundary-value problem. Solving the resonant modes involves the solution of Maxwell's equations and enforcing the appropriate boundary conditions at each dielectric-air interface. The abrupt discontinuity at the interfaces allows a standing EM wave to be supported inside the dielectric volume at a specific resonant frequency. This resonant frequency is related to the size and dielectric properties of the dielectric body.

2.2 Electric Polarization

Prior to analysing the rectangular DRA, it is meaningful to explain the phenomenon of dielectric polarization since it gives insight into the EM resonance mechanism of the DRA. In dielectrics, the dominant charges are bound negative and positive charges held in place by atomic and molecular forces. Ideal dielectrics do not contain any free charge (unlike conductors) and the atoms and molecules are macroscopically neutral (illustrated in Figure 2.2a). Under an applied external electric field, \bar{E} , the individual positive (the nucleus of the atoms) and negative charges (the electron cloud around the atoms) shift an infinitesimal distance relative to the atom's centre. The result is the formation of induced electric dipoles, which align themselves with the applied field (this phenomenon is known as orientational polarization and is illustrated in Figure 2.2b).

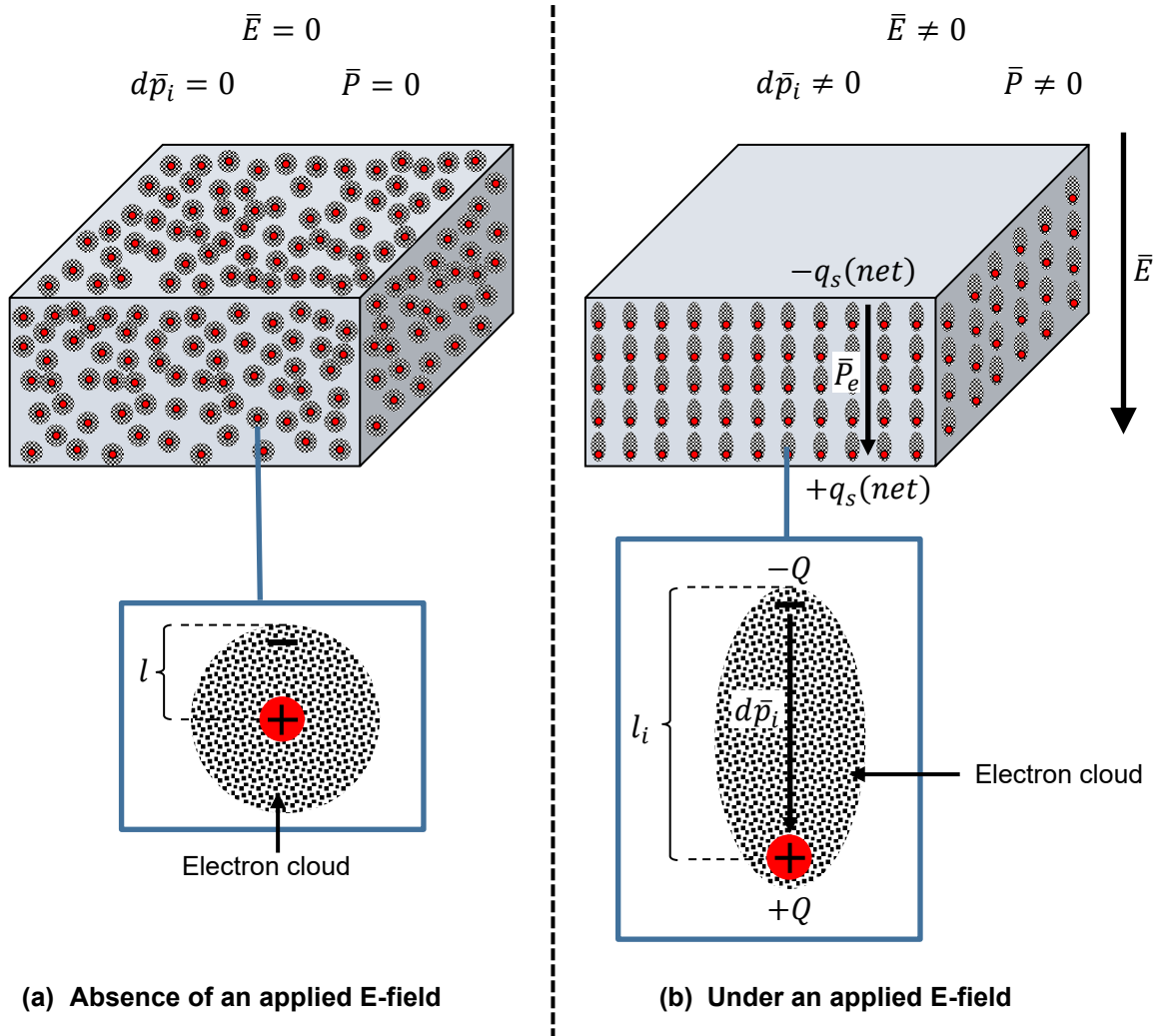


Figure 2.2: Macroscopic model of a dielectric showing electric polarization
 (a) $\bar{E} = 0$ and (b) $\bar{E} \neq 0$

The effect of each induced dipole is represented by a dipole with induced dipole moment $d\bar{p}_i$ given by (Balanis, 1989)

$$d\bar{p}_i = Ql_i , \quad (2.1)$$

where Q is the magnitude of each negative and positive charge whose centroids are displaced by a distance l_i . This phenomenon provides the ability of the dielectric material to store electric energy (potential energy), due to the shift against the restraining forces of their bound charges and external applied forces. Upon the removal of the applied field, the atoms return to their original state. The time required for the atoms to reach their original state is in the form of an exponential decay referred to as the relaxation time. Practically, the presence of the polarization dipoles is accounted for by introducing the electric polarization vector, \bar{P}_e , which augments the total electric flux density as

$$\bar{D} = \varepsilon_0\bar{E} + \bar{P}_e . \quad (2.2)$$

For linear dielectrics¹, \bar{P}_e is linearly related to the applied electric field as

$$\bar{P}_e = \varepsilon_0\chi_e\bar{E} , \quad (2.3)$$

where χ_e is referred to as the electric susceptibility (dimensionless quantity which may be complex). We can then rewrite (2.2) as

$$\bar{D} = \varepsilon_0\bar{E} + \bar{P}_e = \varepsilon_0\bar{E} + \varepsilon_0\chi_e\bar{E} = \varepsilon_0(1 + \chi_e)\bar{E} = \varepsilon\bar{E} , \quad (2.4)$$

where

$$\varepsilon = \varepsilon' - j\varepsilon'' = \varepsilon_0(1 + \chi_e) . \quad (2.5)$$

In (2.5) ε is the complex permittivity (also referred to as the dielectric constant) of the medium. The electric polarization vector changes with the polarity of the applied field. In turn the electric susceptibility is altered together with the dielectric constant. These parameters are also frequency depended. Furthermore, the imaginary part of the dielectric constant accounts for dielectric loss in the form of heat (due to damping of the vibrating dipole moments). Free-space as a medium is lossless since it only has a real-valued dielectric constant. The dielectric loss can also be considered as an equivalent conductor loss since in a material with conductivity, σ , a conduction current density will exist. This current density can be stated in an electromagnetic version of Ohm's law as (Pozar, 2011)

$$\bar{J} = \sigma\bar{E} , \quad (2.6)$$

substituting in the Maxwell-Ampere equation gives

¹ For strong E-fields or in a nonlinear material the relationship between \bar{P}_e and \bar{E} is nonlinear and \bar{P}_e can be represented by a power series of \bar{E} as $\bar{P}_e = \varepsilon_0(\chi_1\bar{E} + \chi_2\bar{E}^2 + \chi_3\bar{E}^3 + \dots)$. Here χ_i is the i -th order susceptibility which is then an $i + 1$ order tensor.

$$\begin{aligned}
\nabla \times \bar{H} &= j\omega\bar{D} + \bar{J} \\
&= j\omega\bar{E} + \sigma\bar{E} \\
&= j\omega\varepsilon'\bar{E} + (\omega\varepsilon'' + \sigma)\bar{E} \\
&= j\omega\left(\varepsilon' - j\varepsilon'' - j\frac{\sigma}{\omega}\right)\bar{E}. \tag{2.7}
\end{aligned}$$

This shows that the dielectric loss is comparable to conductivity loss. The term $(\omega\varepsilon'' + \sigma)$ can thus be considered as a total effective conductivity. Practically, the quantities of interest are the real relative permittivity (dielectric constant), ε_r ,

$$\varepsilon_r = \frac{\varepsilon'}{\varepsilon_0}, \tag{2.8}$$

and loss tangent, defined as

$$\tan \delta = \frac{\omega\varepsilon'' + \sigma}{\omega\varepsilon'}, \tag{2.9}$$

which is the ratio of the real to imaginary part of the total displacement current. Dielectric substrate manufacturers typically specify relative permittivity and loss tangent at a specific frequency. Furthermore, the refraction index is often given when manufacturers specify glass/ceramic materials. The refraction index is typically used in designs for optical application. The relationship between the dielectric constant and refraction index of a material is related by

$$\eta = \frac{c_0}{c} = \frac{\sqrt{\mu_r\varepsilon_r\mu_0\varepsilon_0}}{\sqrt{\mu_0\varepsilon_0}} = \sqrt{\mu_r\varepsilon_r}, \tag{2.10}$$

where μ_r and ε_r are the relative permeability and permittivity of the medium respectively, with μ_0 and ε_0 being the permeability and permittivity of free-space. For nonmagnetic materials, $\mu_r = 1$ the refraction index of a dielectric material can be defined as $\eta = \sqrt{\varepsilon_r}$.

Analogous to electric polarization, the mechanism describing magnetic materials is as a result to the alignment of magnetic dipoles (caused by small current loops associated with a spinning electron around the nucleus of an atom) under an applied magnetic field. The result is a magnetic polarization vector, \bar{P}_m , a complex magnetic susceptibility, χ_m , and finally the complex permeability, $\mu = \mu' - j\mu''$ of the medium.

Since Sapphire is an anisotropic material and considered as a candidate material for the ISPA, it should be explained that anisotropic materials have a \bar{P}_e which is not in the same direction as the applied electric field. The relationship in (2.6) for an anisotropic material takes the form as (Pozar, 2011)

$$\begin{bmatrix} D_x \\ D_y \\ D_z \end{bmatrix} = \begin{bmatrix} \epsilon_{xx} & \epsilon_{xy} & \epsilon_{xz} \\ \epsilon_{yx} & \epsilon_{yy} & \epsilon_{yz} \\ \epsilon_{zx} & \epsilon_{zy} & \epsilon_{zz} \end{bmatrix} \begin{bmatrix} E_x \\ E_y \\ E_z \end{bmatrix} = [\epsilon] \begin{bmatrix} E_x \\ E_y \\ E_z \end{bmatrix}. \quad (2.11)$$

The dielectric material proposed for the ISPA implementation is LASF35 (SCHOTT, n.d) and has a $\epsilon_r = 20$ and $\tan \delta = 0.0063$ specified at 6 GHz and is here treated to be isotropic and nonmagnetic.

2.3 Rectangular Dielectric Resonator

The isolated rectangular Dielectric Resonator (DR) has three independent dimensions and is shown in Figure 2.3.

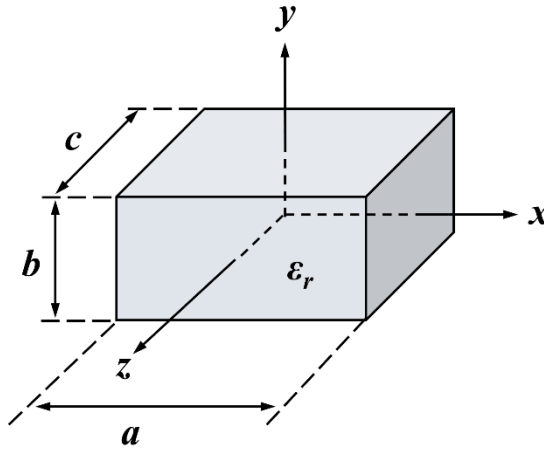


Figure 2.3: Isolated rectangular DRA

On the resonant modes, Van Bladel (1975) deduced that a DR of high permittivity and arbitrary shape can support both confined and nonconfined modes. These modes satisfy the magnetic wall approximations (Mongia et al., 1997)

$$\hat{n} \cdot \bar{D} = 0 \quad (2.12)$$

$$\hat{n} \times \bar{H} = 0, \quad (2.13)$$

where \bar{D} is the electric flux density, \bar{H} the magnetic-field intensity and \hat{n} the vector normal to the surface of the DRA wall. Confined modes satisfy both (2.12) and (2.13), while the nonconfined modes only satisfying (2.12). Only dielectric bodies of revolution (cylindrical and spherical DRAs) support confined modes whereas nonconfined modes are supported by

rectangular DRAs (Van Bladel, 1975). Confined and nonconfined modes of the lowest order (fundamental modes) radiate like electric and magnetic dipoles respectively. Okaya and Barash (1962) suggested that the rectangular DR can support Transverse Electric (TE) and Transverse Magnetic (TM) modes to any of the independent dimensions a (in x -axis), b (in y -axis) and c (in z -axis²). Research into rectangular DRAs by Mongia and Ittipiboon (1997) found that the lowest TM modes do not exist since they do not satisfy the magnetic wall condition (2.12).

Here and in the literature, the rectangular DRA is analysed using the same analysis of the TE modes in a rectangular DR. With reference to Figure 2.3, when the dimensions are such that $a > b > d$, the modes from lowest to highest resonant frequencies are the $TE^{z_{11\delta}}$, $TE^{y_{1\delta 1}}$ and $TE^{x_{\delta 11}}$ and radiate like z -, y - and x -directed magnetic dipoles respectively. The subscripts are known as mode indices and denote the number of field maxima in the x -, y - and z -direction. The theory and mode nomenclature, inside and outside the DRA is adopted from the Dielectric Waveguide Model (DWM).

2.4 Dielectric Waveguide Model

Marcatili (1969) proposed the DWM to determine the guided wavelength in rectangular dielectric guides. Figure 2.4 illustrates such a guide with infinite extent, width a in the x -direction, height b in the y -direction and wave propagation in the z -direction. The modal fields in the guide can be divided into $TE^{y_{mn}}$ and $TM^{y_{mn}}$ (where m and n denotes the number of variations in the standing wave pattern in the x - and y -direction, respectively). Figure 2.5 shows the cross-section of the guide where the EM problem consist of five homogenous regions which may be of different refractive indices. A complete solution for the field components in all the regions outside the resonator is not known. Marcatili (1969) introduced a simplification by assuming the fields vary sinusoidally inside (n_1) the guide while those in the regions n_2 , n_3 , n_4 and n_5 decay exponentially. In order to simplify the analysis, the fields in the shaded regions of Figure 2.5 are assumed to be zero.

² for an isolated dielectric resonator antenna this variable is labelled " d " in the z -axis.

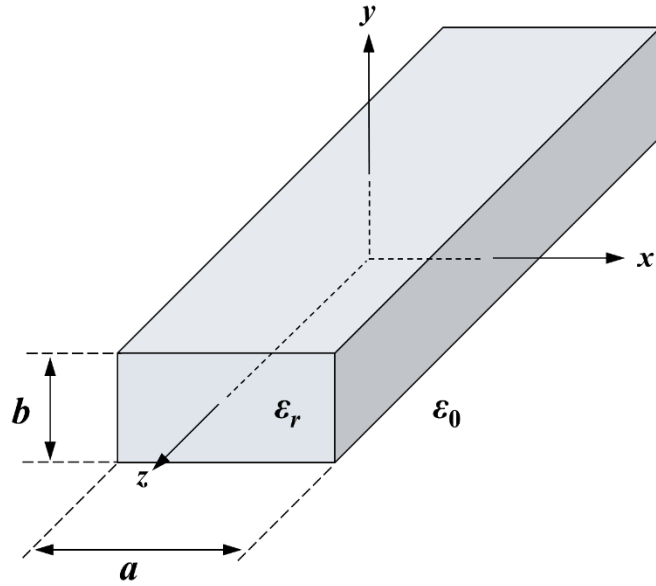


Figure 2.4: Infinite rectangular dielectric waveguide

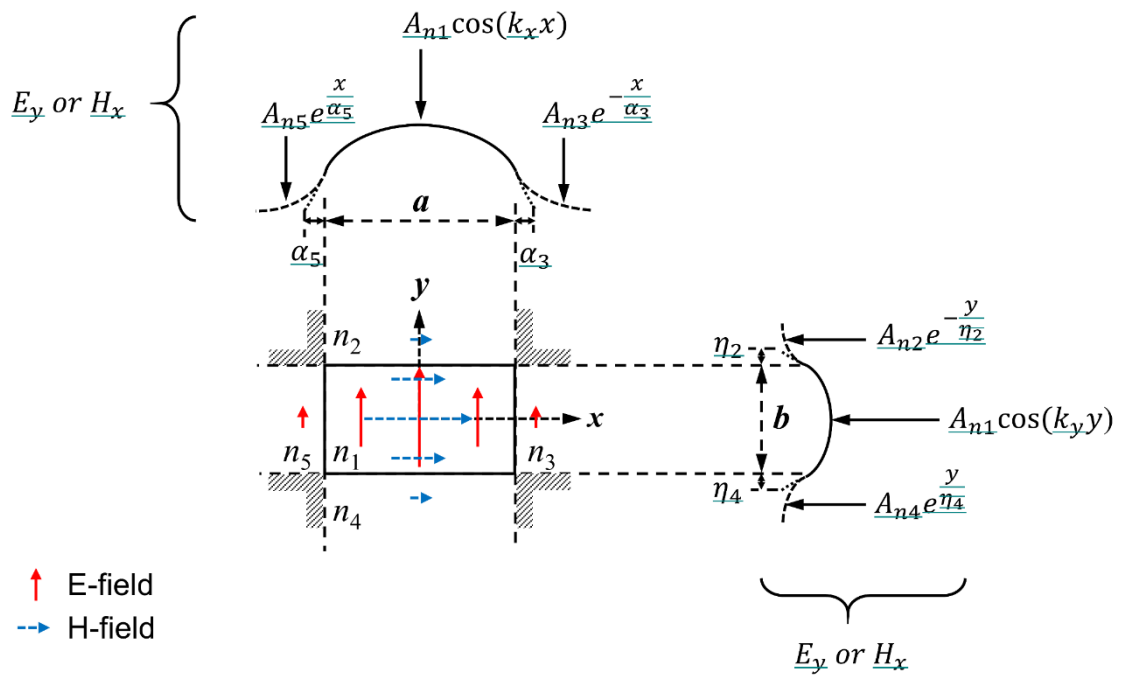


Figure 2.5: Cross-sectional field distribution of the rectangular dielectric waveguide

To determine the wavenumbers inside the guide, n_1 ($|x| \leq a/2$ and $|y| \leq b/2$), the fields are matched at the wall boundaries to give the wavenumbers in the x -, y -, and z -directions as

$$k_x = \frac{m\pi}{a} \left(1 + \frac{2}{ak_0\sqrt{\epsilon_r - 1}} \right)^{-1}, \quad (2.14)$$

$$k_y = \frac{n\pi}{b} \left(1 + \frac{2}{bk_0\sqrt{\epsilon_r - 1}} \right)^{-1}, \quad (2.15)$$

$$k_z = \sqrt{\varepsilon_r k_0^2 - k_x^2 - k_y^2}. \quad (2.16)$$

The attenuation constants, α (in the x -direction) and η (in the y -direction) outside n_1 ($|x| \geq a/2$ and $|y| \geq b/2$) are determined as

$$\alpha = \frac{1}{\sqrt{(\varepsilon_r - 1)k_0^2 - k_x^2}}, \quad (2.17)$$

$$\eta = \frac{1}{\sqrt{(\varepsilon_r - 1)k_0^2 - k_y^2}}, \quad (2.18)$$

where k_0 is the free-space wavenumber given by

$$k_0 = \frac{2\pi}{\lambda_0} = \frac{2\pi f_0}{c}, \quad (2.19)$$

where c is the speed of light in free-space, f_0 is the operating frequency, and λ_0 is the free-space wavelength. Since the fields are confined within the guide, for well-guided modes ($\varepsilon_r \gg \varepsilon_0$), a further approximation for the wavenumbers in the x - and y -directions can be made. Enforcing the boundary condition (2.12) on the four walls of the resonator parallel to the direction of propagation then equations (2.14) and (2.15) reduce to

$$k_x = \frac{m\pi}{a} = \frac{2\pi}{\lambda_x} \quad (2.20)$$

$$k_y = \frac{n\pi}{b} = \frac{2\pi}{\lambda_y} \quad (2.21)$$

This approximation is equivalent to assuming magnetic walls at $x = \pm a/2$ and $y = \pm b/2$. When the dielectric guide shown in Figure 2.4 is truncated at $z = \pm z/2$ to form a dielectric resonator the propagation constants and characteristic equations for the x - and y -direction stay unchanged and a standing wave pattern is set up inside the DR along the z -direction. For this structure then the lowest order TE mode is the $TE_{11\delta}^z$. The field configuration internal to the DRA for this mode is found as (Mongia & Ittipiboon, 1997)

$$E_x = Ak_y \cos(k_x x) \sin(k_y y) \cos(k_z z), \quad (2.22)$$

$$E_y = -Ak_x \sin(k_x x) \cos(k_y y) \cos(k_z z), \quad (2.23)$$

$$E_z = 0, \quad (2.24)$$

$$H_x = \frac{(k_x k_z)}{j\omega\mu_0} A \sin(k_x x) \cos(k_y y) \sin(k_z z), \quad (2.25)$$

$$H_y = \frac{(k_y k_z)}{j\omega\mu_0} A \cos(k_x x) \sin(k_y y) \sin(k_z z), \quad (2.26)$$

$$H_z = \frac{(k_x^2 + k_y^2)}{j\omega\mu_0} A \cos(k_x x) \cos(k_y y) \cos(k_z z), \quad (2.27)$$

where the wavenumbers k_x and k_y are derived from (2.20) and (2.21) respectively and A an arbitrary constant associated with the maximum amplitude of the internal fields. Furthermore, the wavenumbers, k_x , k_y and k_z satisfy the separation (constraint) equation

$$k_x^2 + k_y^2 + k_z^2 = \varepsilon_r k_0^2, \quad (2.28)$$

and

$$k_z \tan\left(k_z \frac{d}{2}\right) = k_{z0} = \sqrt{(\varepsilon_{r1} - \varepsilon_{r0})k_0^2 - k_z^2}. \quad (2.29)$$

where d is the length of the DRA and k_{z0} the free-space wavenumber in the z -direction. Equation (2.29) can also be written as

$$d = \frac{2}{k_z} \tan^{-1} \frac{k_{z0}}{k_z}. \quad (2.30)$$

For the $TE_{11\delta}^z$ mode the fractional half cycle of the field variation in the z -direction is given by

$$\delta = \frac{k_z}{\pi/d}. \quad (2.31)$$

The tangential components of the electric and magnetic fields in the direction of propagation are assumed continuous across the surface at $|z| = d/2$ giving the transcendental equation for k_z by (2.29) or written in the form (2.30). The resonant frequency is solved by substituting (2.20), (2.21) and the separation equation (2.28) into (2.29) and solving for k_z . The separation equation (2.28) is then solved for the free-space wavenumber, k_0 by

$$k_0 = \omega \sqrt{\varepsilon_0 \mu_0} = \frac{2\pi}{\lambda_0} = \frac{2\pi f_0}{c_0}. \quad (2.32a)$$

The resonant frequency is then solved as

$$f_0 = \frac{c_0}{2\pi} k_0 = \frac{c_0}{2\pi} \sqrt{\frac{k_x^2 + k_y^2 + k_z^2}{\epsilon_r}}. \quad (2.33b)$$

The analysis of the resonant frequencies for the $TE_{\delta 11}^x$ and $TE_{1\delta 1}^y$ modes are similar to that of the $TE_{11\delta}^z$ mode above. Using equation (2.33b) the resonant frequencies for an isolated rectangular DRA made from Pyrex ($\epsilon_r = 4.82$, $\tan \delta = 0.0054$), Sapphire ($\epsilon_r = 11.5$, $\tan \delta = 0.0001$) and LASF35 ($\epsilon_r = 20$, $\tan \delta = 0.0063$) are shown in Figure 2.6.

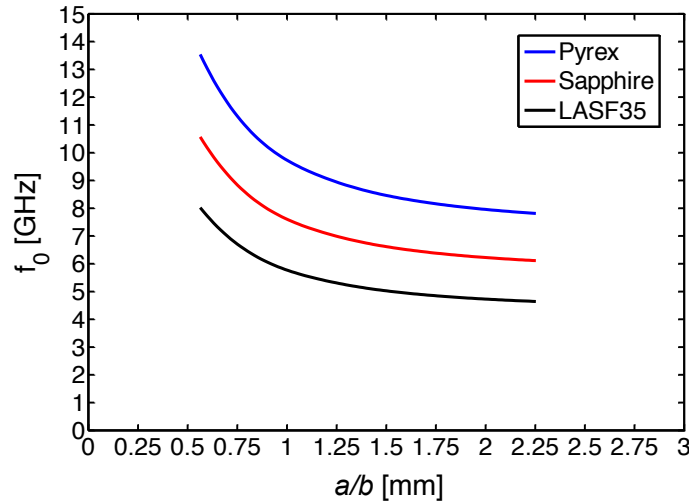


Figure 2.6: Resonant frequency of an isolated rectangular DRA for different aspect ratios and height, $b = 9$ mm

From Figure 2.6 it can be seen that LASF35 provides the most compact DRA with the lowest fundamental frequency over a DRA made from Pyrex or Sapphire. With the height of the DRA chosen as $h = b/2 = 4.5$ mm (limited by the CubeSat deployer restrictions and solar panel), a resonant frequency of 5.5 GHz was chosen as the design frequency which translates to a rectangular DRA with dimensions $a = d = 10.14$ mm and $b = 9$ mm for the LASF35. Using the same aspect ratio, the resonant frequencies for Sapphire and Pyrex is calculated as 7.25 GHz and 9.29 GHz respectively.

The modal fields for the $TE_{11\delta}^z$ mode are shown Figure 2.7. The H_z component of the H-field is dominant along the centre (into the page) of the DRA. Concurrently the E_x and E_y components of the E-field circulate around the H_z component. Furthermore, it can be seen that a metallic plane can practically be placed in the xz -plane ($y = 0$) and in the yz -plane ($x = 0$) without disturbing the field configuration and resonant frequency. Thus with the aid of the image theory, the isolated rectangular DRA can be halved such that $h = b/2$ when mounted on a ground plane (shown in Figure 2.1). Furthermore, when studying (2.23) it is evident that the E_y component of the E-field is a maximum when $z = 0$ and $|x| = a/2$. This

field configuration is characterised as the $TE^z_{11\delta}$ mode for a rectangular DRA on a ground plane.

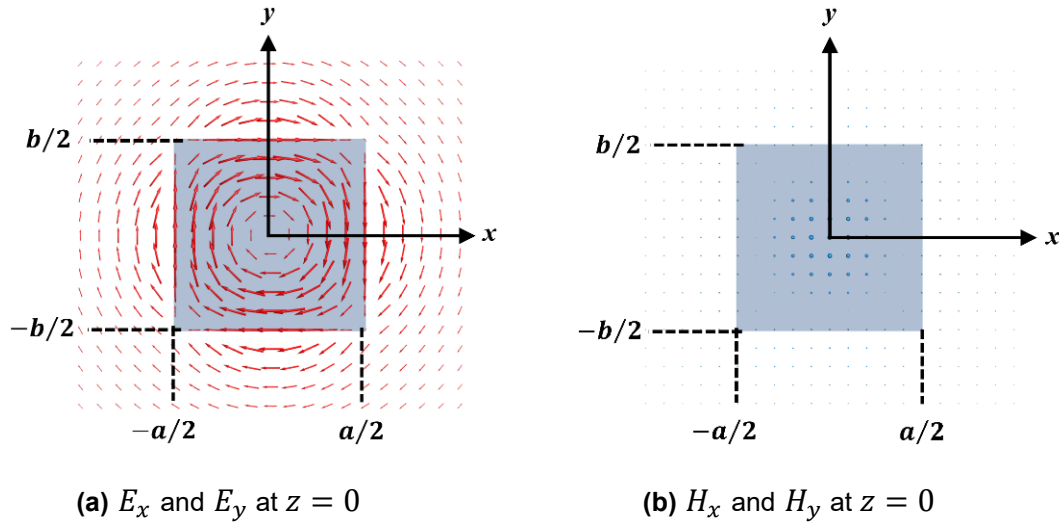


Figure 2.7: $TE^z_{11\delta}$ modal fields for the isolated rectangular DRA

The probe feed was chosen to excite the DRA since it simplifies the construction by placing the probe outside the DRA wall instead of inside the DRA. Since the DRA is made from ceramic glass, drilling an accurate hole inside the DRA imposes fabrication challenges. Furthermore, the amount of coupling is controlled by varying the probe length and position along the DRA wall.

2.5 Radiation Model and Q-factor

Since the fundamental modes, $TE^z_{11\delta}$, $TE^y_{1\delta 1}$ and $TE^x_{\delta 1 1}$ radiate like z -, y - and x -directed short magnetic dipoles respectively, the magnetic dipole model is commonly used to determine the Q-factor of rectangular DRAs. The derivation comes from the fact that a homogeneous dielectric body of dielectric constant, ϵ_r , in free-space radiates like a volume electric current of density \bar{J}_p given as (van Bladel, 1975)

$$\bar{J}_p = j\omega\epsilon_0(\epsilon_r - 1)\bar{E}, \quad (2.34)$$

where \bar{E} is the electric field intensity inside the DRA given by (2.22) to (2.24). For the fundamental mode the electric field components are tangential to the surface of the resonator and thus produces a DRA which radiates like a magnetic dipole of moment \bar{p}_m given as (Mongia & Ittipiboon, 1997)

$$\bar{p}_m = \frac{1}{2} \oint \bar{R} \times \bar{J}_p dv, \quad (2.35)$$

where \bar{R} is a vector from the origin of the DRA. Substituting \bar{J}_p as derived by (2.34) in (2.35) a closed-form expression for \bar{p}_m is derived as (Mongia & Ittipiboon, 1997)

$$\bar{p}_m = -\frac{j8A\omega\varepsilon_0(\varepsilon_r - 1)}{k_x k_y k_z} \sin\left(k_z \frac{d}{2}\right) \hat{z}. \quad (2.36)$$

Furthermore, the power radiated by a magnetic dipole of moment \bar{p}_m is given by

$$P_{rad} = 10k_0^4 |\bar{p}_m|^2, \quad (2.37)$$

As stated previously, for well guided modes (DRAs with high dielectric constants) the fields and thus stored electric energy is confined inside the DRA. The stored electric energy is found by (Mongia & Ittipiboon, 1997)

$$W_e = \frac{\varepsilon_0 \varepsilon_r a b d A^2}{32} \left(1 + \frac{\sin(k_z d)}{k_z d}\right) (k_x^2 + k_y^2). \quad (2.38)$$

At resonance the average stored magnetic and electric energies are identical and the radiation Q-factor can thus be determined by

$$Q = \frac{2\omega_0 W_e}{P_{rad}}. \quad (2.39)$$

Using equation (2.39) the radiation Q-factor is calculated for the isolated rectangular DRA in Figure 2.4 and is shown Figure 2.8 below.

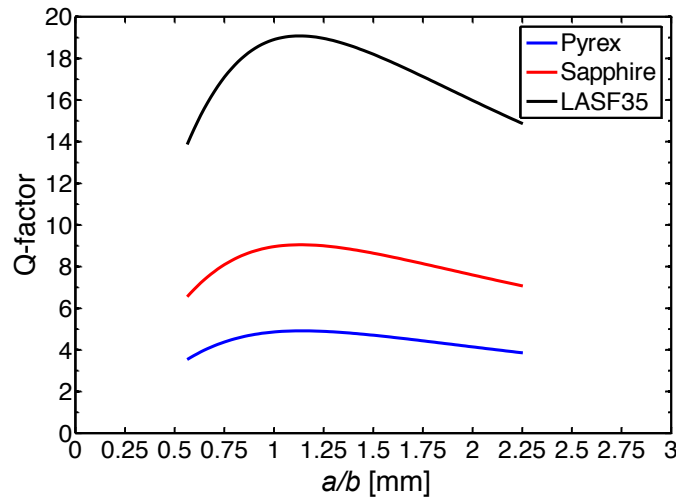


Figure 2.8: Radiation Q-factor of an isolated rectangular DRA for different aspect ratios and height, $b = 9$ mm

The Q-factor of the DRA is influenced by the feeding (coupling) mechanism which transfer energy to the DRA and load the Q-factor. An external Q-factor is defined in terms of the coupling factor as (Luk & Leung, 2003)

$$Q_{ext} = \frac{Q}{\rho}, \quad (2.40)$$

where ρ is the coupling factor with the loaded Q-factor determined as (Luk & Leung, 2003)

$$Q_L = \left(\frac{1}{Q} + \frac{1}{Q_{ext}} \right)^{-1} = \frac{Q}{1 + \rho}. \quad (2.41)$$

A coupling factor of $\rho = 1$ stipulates a condition of maximum power transfer (referred to as critical coupling) between the coupling port and the DRA. For $\rho < 1$ and $\rho > 1$ the DRA is said to be under and over coupled, respectively. The type of coupling port and its location determines the type of mode which will be excited, and the amount of power transferred to the mode. For the $TE_{11\delta}^z$ mode critical coupling was achieved at $z = 0$ and is characterised by a sharp resonance in the input reflection coefficient. The results of a coupling study for a 50Ω coaxial probe and the DRA are presented in section 3.3.1 and demonstrates the relationship between the probe location and its effect on the input reflection coefficient.

It is known that the rectangular DRA offers more design flexibility, with respect to bandwidth control, than other shapes since the bandwidth is dependent on the DRA's aspect ratio. The design flexibility comes from the fact that for a given resonant frequency and dielectric constant any two of the three dimensions can be chosen independently (Al-Zoubi & Kishk, 2009). Rectangular shaped DRAs are also much easier to fabricate thus reducing fabrication cost. Additive manufacturing has reached maturity to 3D-print complex shapes out of dielectrics and metals however this manufacturing technique was not considered for this dissertation

To illustrate the design flexibility offered by the rectangular DRA the Q-factors for various aspect ratios were calculated for rectangular DRAs made from Pyrex, Sapphire and LASF35. Again, the design frequency of 5.5 GHz was chosen. The results are summarised in Table 2.1. Furthermore, Figure 2.8 demonstrates the relationship between the dielectric constant and bandwidth showing that an increase in dielectric constant translates to an increase in stored energy and thus an increase in the radiation Q-factor. For very high dielectric constant values the Q-factor can be approximated by $\epsilon_r^{3/2}$. In this dissertation a low Q-factor is favoured since this translates to an increased radiation efficiency and bandwidth. From Table 2.1 the candidate rectangular DRA chosen for solar cell integration has dimensions $a = d = 10.14$ mm and $b = 9$ mm, with $\epsilon_r = 20$ and translates to a Q-factor of 19.1 and a bandwidth of 3.7%. This candidate is also the DRA with the highest Q-factor and smallest bandwidth however, it is the only candidate with an aspect ratio compact enough to satisfy the height specification of a CubeSat launch vehicle (CubeSat Design Specification, 2014).

Table 2.1: Dimensions and Q-factor for the candidate isolated rectangular DRA

a [mm]	b [mm]	d [mm]	a/b	d/b	f_0 [GHz]	Q	BW [%]
7.25	58	7.25	0.13	0.13	5.50	5	14.1
13.41	26.81	6.70	0.5	0.25	5.50	8	8.8
7.31	29.23	7.75	0.25	0.27	5.50	9.6	7.4
15.85	9.05	9.05	1.75	1.0	5.50	15.6	4.5
10.14	9	10.14	1.13	1.13	5.51	19.1	3.7
24.42	6.9	13.95	3.54	2.02	5.55	9.2	7.7

2.6 Conclusion

In this chapter, the theoretical background for the isolated DRA and rectangular DRA on a ground plane was shown. The design flexibility of the rectangular DRA was also demonstrated. The DWM is presented as a first-order method for calculating the resonant frequency and Q-factor. A candidate isolated rectangular DRA element was designed using the DWM which produced an element with size $a = d = 10.14$ mm and $b = 9$ mm. When placed on a ground plane the height of the DRA amounts to $h = b/2 = 4.5$ mm which satisfy the height constraint imposed by the CubeSat deployment mechanism. The DWM model does not take into effect the feeding mechanism and finite ground effects. In the following chapter, full-wave analysis is used to consider the above-mentioned effects.

Chapter 3 Theoretical and Experimental Results

3.1 Introduction

This chapter is devoted to practically validate the theoretical results discussed in the previous chapter. In the absence of a closed-form formulation for the rectangular DRA, validation is done through several numerical techniques, including a numerical technique based on the Theory of Characteristic Modes (TCM). Initially, the isolated rectangular DRA case is considered followed by the rectangular DRA on a rectangular ground plane. This validation is done to analyse the resonant modes prior to solar panel integration.

The shape and aspect ratio of a DRA dictates the modes supported by the structure. As shown in Chapter 2, for a given ϵ_r the radiation Q-factor and resonant frequency can be determined. Due to the lack of an exact solution for the resonant frequency, Q-factor, input impedance and radiation patterns, it is common practice to make use of one or more numerical techniques. These include both frequency and time domain techniques such as the Method of Moments (MoM) and Finite-Difference Time-Domain (FDTD) methods respectively. The FDTD method was used in (Semouchkina et al., 2002) to study the resonant modes of rectangular DRAs and confirmed the speculation by Mongia and Ittipiboon (1997) that the lowest TM mode ($TM_{11\delta}^z$) is not supported by rectangular DRAs. The lowest TE mode ($TE_{11\delta}^z$) is only supported by rectangular DRAs with a suitable aspect ratio.

3.2 Isolated Rectangular DRA in free-space

In van Bladel (1975), the excitation of DRAs by both interior volume sources and exterior incident fields was investigated analytically. The results were experimentally verified by means of a Radar Cross-Section (RCS) measurement in Mongia et al. (1992) and Trueman et al. (1994). Here, it shall be demonstrated that the resonant modes of a DRA can be determined from the viewpoint of a scattering problem utilising the RCS method numerically. The geometric parameters for the antenna shown in Figure 3.1 are $a = 9.31$, $b = 18.62$ mm, and $d = 4.6$ mm with $\epsilon_r = 37.84$. These dimensions were chosen as this was often analyzed in the literature (Mongia & Ittipiboon, 1997). In addition Figure 3.1 shows the rectangular DRA with an incident field polarized with the electric field parallel to the z -axis with the plane wave incident on the yz -face. Also shown is the simulated RCS using the MoM and the Finite

Integration Technique (FIT). The fundamental mode ($TE_{1\delta 1}^y$) occurs at 4.3 GHz and the higher order modes, $TE_{1\delta 3}^y$, $TE_{2\delta 3}^y$ and $TE_{1\delta 5}^y$, at 5.81 GHz, 7.53 GHz and 7.96 GHz respectively. Furthermore, Figure 3.1 shows the radiation pattern of the $TE_{1\delta 1}^y$ mode. The electric field in the xz -plane for the $TE_{1\delta 1}^y$ mode is shown in Figure 3.2.

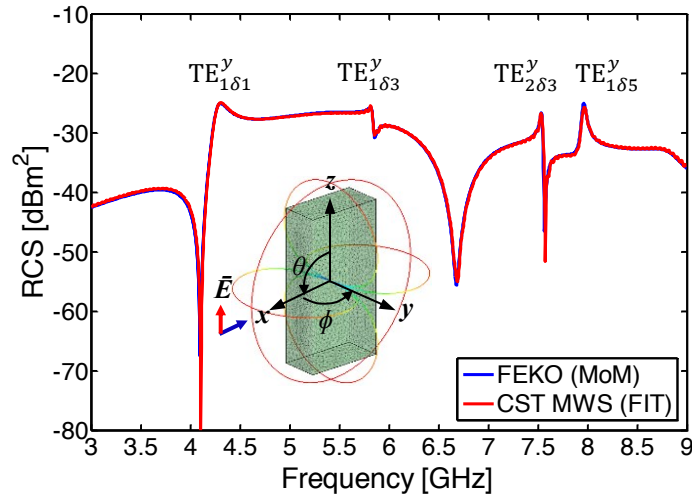


Figure 3.1: RCS for an isolated rectangular DRA in free-space with a z -axis polarized incident plane wave. The scattered radiation pattern cuts for the $TE_{1\delta 1}^y$ mode are shown

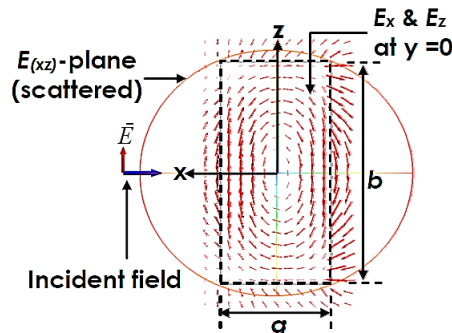


Figure 3.2: The scattered electric field configuration in the xz -plane at $y = 0$ for the $TE_{1\delta 1}^y$ mode of an isolated rectangular DRA in free-space

A summary of the RCS results of the LASF35 ceramic glass candidate is given later in this chapter and summarised with results obtained with other numerical results.

3.2.1 Isolated Dielectric Cube

The theory of Van Bladel (1975) concludes that, at the resonant frequencies, the scattering cross-section of a dielectric body with high dielectric constant ($\epsilon_r \rightarrow \infty$) is independent of its shape, mode number, and dielectric constant. As stated earlier, the modes of an arbitrary shaped dielectric resonator of very low dielectric constant are of the nonconfined type which does not satisfy the magnetic wall condition at the surface of the resonator (Mongia & Ittipiboon, 1997). However, if the dielectric resonator is a body of revolution (such as the

cylindrical or spherical type), some of the modes of the dielectric resonator can well support the confined type, which satisfy the condition of the magnetic wall.

Scattered fields from a Dielectric Resonator (DR) can be computed from the multipole expansion method (Van Bladel, 1975) and when $\epsilon_r \rightarrow \infty$, the term that contributes to the scattering for the nonconfined modes is the “magnetic dipole” term (Mongia et al., 1992). If the incident magnetic field is parallel to the direction of the induced magnetic dipole moment in the DR then the scattering RCS of the resonator at the resonant frequencies of the nonconfined modes is given by Van Bladel (1975)

$$\sigma = \frac{3}{2\pi} \lambda_0^2, \quad (3.1)$$

where σ is the RCS of the DR, λ_0 is the free-space wavelength corresponding to the resonant frequency of the nonconfined mode of the dielectric body. The three lowest order TE modes (one in each axis) are supported by the rectangular DRA, as shown in Chapter 2. Using FEKO a dielectric cube, also previously studied by Trueman (1993), was excited by a plane wave polarized with the electric field parallel to the z -axis and incident on the yz -face of the dielectric cube. The plane wave could have been polarised to any of the faces since all the resonant modes are degenerate. Figure 3.3 shows the FEKO predicted RCS compared with the measured result of Trueman (1993). The results for this study are summarised later in Table 3.3 and compared with the results obtained using supplementary numerical techniques.

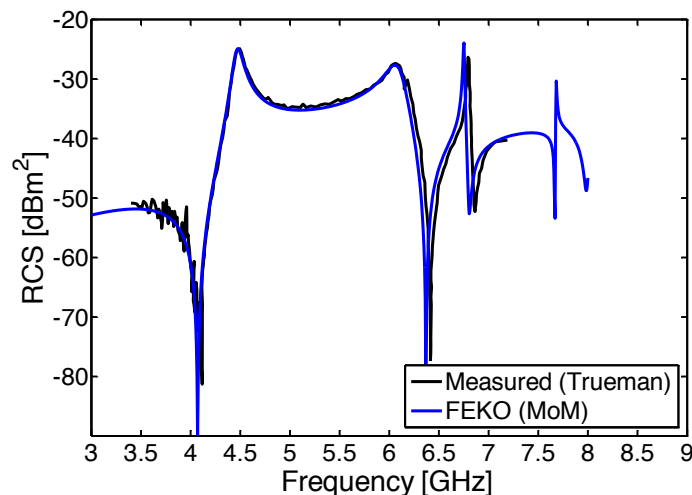


Figure 3.3: RCS of the cubic DRA

The resonant frequency of the fundamental mode occurs at 4.49 GHz with the FEKO predicted result calculated as 4.48 GHz. Furthermore, the measured and predicted results compare well and confidence was gained in predicting the resonant modes of isolated rectangular DRAs using this RCS technique.

3.3 Rectangular DRA on a ground plane

The modes excited for a DRA placed on a ground plane are commonly the TE modes. As stated previously, the isolated DRA in Figure 3.1 can be geometrically halved in the $z = 0$ plane (i.e., height of DRA, $h = b/2$) and mounted on a ground plane of infinite extent resulting in an electromagnetically equivalent DRA. Initially a copper strip feed of width 1 mm and length 6.5 mm was used to feed this DRA. Figure 3.4 shows the reflection coefficient calculated with both the MoM and FIT, with the $TE_{1\delta}^y$ resonant at 4.1 GHz. This correlates with the $TE_{11\delta}^z$ mode in Mongia and Ittipiboon (1997) which exhibited a resonant frequency of 4.25 GHz (note the DRA orientation in the numerical models is taken with the height in the z -direction. In the literature the height is taken in the y -direction). The small shift in resonant frequency between the published result and that presented here is attributed to the feeding mechanism used (a probe is used in the published data and here a strip is used). Furthermore, the differences between the types of solvers are very small.

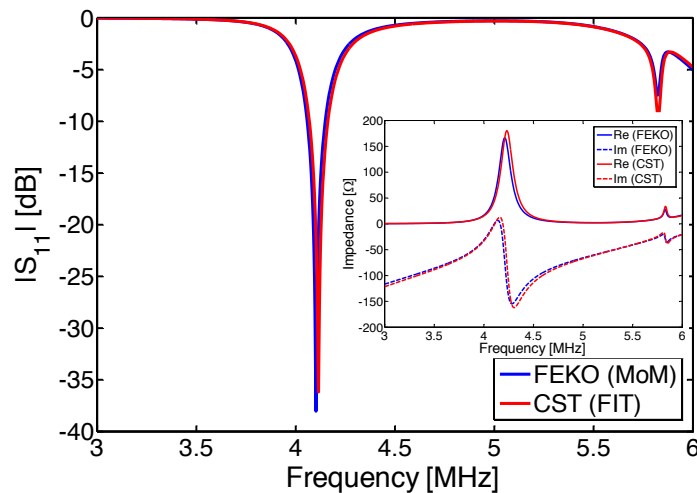


Figure 3.4: Simulated $|S_{11}|$ for the rectangular DRA on a ground plane

The resulting electric field is shown in Figure 3.5 and is equivalent to that shown in Figure 3.2 apart from the fields perturbed by the feeding strip. Also shown is the radiation pattern for the xy -plane for the $TE_{1\delta}^y$ mode. As expected, this is like the pattern for the isolated DRA in section 3.2 but here an infinite ground plane was used.

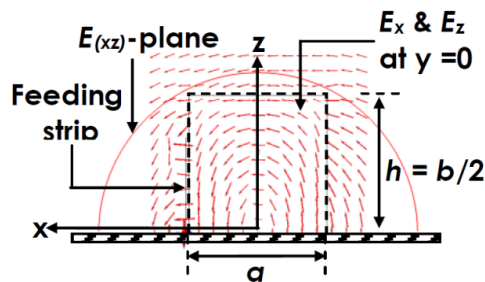


Figure 3.5: Electric field in the xz -plane at $y = 0$ for the $TE_{1\delta}^y$ mode of a rectangular DRA

3.3.1 Probe Coupling

Energy can be coupled to the DRA by observing the expressions for the field distributions (2.22) to (2.27) it can be seen that for the $TE_{11\delta}^z$ mode the E_x component is maximum at $|y| = b/2$ and $z = 0$ whilst the E_y component is maximum at $|x| = a/2$ and $z = 0$. This mode can thus be excited by having the probe positioned as in Figure 3.6, showing the FEKO model. A $50\ \Omega$ coaxial probe (4-hole SMA flange mount with extended dielectric) was used to feed the DRA with diameter, $d_p = 0.65$ mm and probe length, $l_p = 6.5$ mm. For convenience of creating the model, the height dimension, b , is taken in the z -axis.

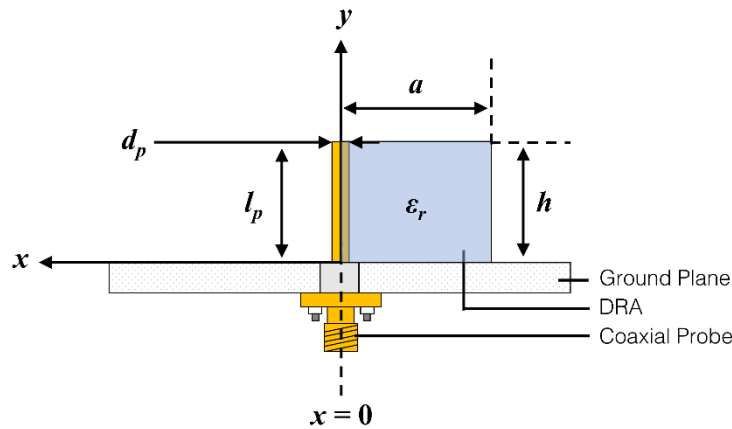


Figure 3.6: Rectangular DRA on a finite ground plane with probe exciting the $TE_{\delta 11}^x$

The probe introduces a loading effect which influences the total Q-factor and should be taken into consideration. Practically the probe can be positioned inside or outside the DRA with the coupling to a particular resonant mode controlled by the probe length and position. As a point of interest and to gain confidence in the coaxial probe model a parametric study was performed in order to achieve critical coupling. The varied parameter was the probe position with the initial position being half outside and half inside ($x = 0$) the DRA as shown in Figure 3.6). Critical coupling was achieved for the probe placed at a distance $1.5p_r$ outside the DRA, where p_r is the probe radius. The input reflection coefficient for this study is shown in Figure 3.7.

Since the DRA is intended to be mounted on top of a solar cell, it is useful to investigate the effect of an air-gap between the DRA and the ground plane. This particular analysis was done in FEKO using a copper strip instead of a coaxial probe with the results shown in Figure 3.8. The input reflection coefficient for the copper strip is comparable to the coaxial probe when the DRA is placed flush on the ground plane. The copper strip also aids the investigation of the effects of a GaAs solar cell on the DRA discussed in section 4.2.

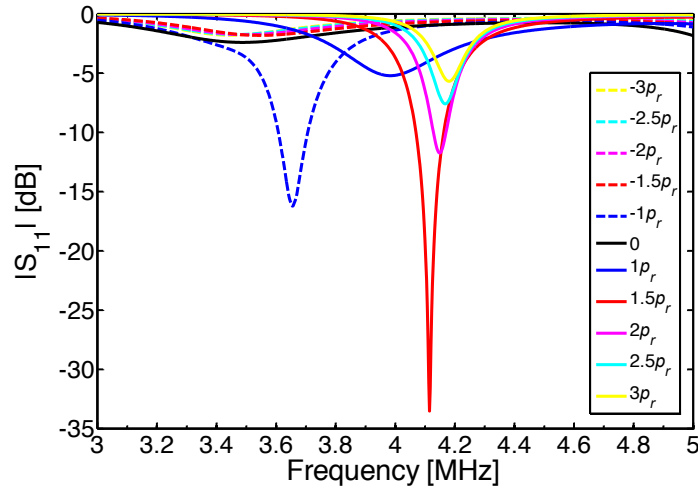


Figure 3.7: Input reflection coefficient for the rectangular DRA fed with a coaxial probe positioned at different locations along the x -axis

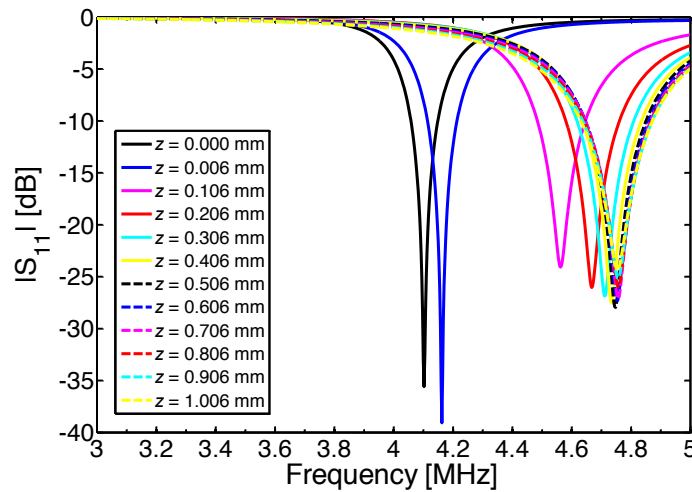


Figure 3.8: Input reflections coefficient for a strip-fed rectangular DRA with various heights above an infinite ground plane

The conclusion is that the resonant frequency increases with an increase in the air-gap. This is consistent with published data (Junker et al., 1994). The effect of the air-gap lowers the effective dielectric constant which in turn lowers the radiation Q-factor and therefore increases the resonant frequency. This frequency shift is particularly severe for DRAs with high dielectric constants since the internal fields are highly confined and the dependence on the ground plane is critical to maintain the field configuration of the fundamental mode (shown in Figure 3.5). For this particular study, it is observed that the resonant frequency measured by Mongia and Ittipiboon (1997) and the FEKO simulated result occurs at 4.25 GHz and 4.12 GHz, respectively. Using the DWM (discussed in section 2.4) the resonant frequency is determined as 4 GHz. The results of this exercise are summarised in Table 3.3. Mongia and Ittipiboon (1997) suggested that the effect of the probe on the

resonant frequency amounts to less than 2%. However, the fact that the authors used the DWM, which is an approximation, should be considered.

3.4 Characteristic Mode Analysis

The rectangular DRA has not enjoyed comprehensive practical use up until recently. The reason being the vague understanding of their resonant modes. The theory of characteristic modes is a relatively new technique to analyse DRAs. The most attractive attribute of this technique is the physical insight they give into the radiating phenomena of an EM problem. Here, the Theory of Characteristic Modes (TCM) is utilised to give insight into the radiation mechanism of the resonant modes of a rectangular DRA.

TCM, as applied to metallic structures, have received much research attention since its inception by Garbacz (1965). Harrington and Mautz (1971) later refined and expanded the theory to dielectric and magnetic bodies. Of late, modal analysis have received attention, specifically within the design of Multiple-Input Multiple-Output antennas for modern cellular networks. Practically, the Characteristic Mode Analysis (CMA³) has only recently been utilised for EM problems involving dielectrics (Bernabeu-Jiménez et al., 2014). Bernabeu-Jiménez et al. (2014) has reported the use of TCM for the design of a rectangular DRA. In this dissertation the TCM is considered as another numerical method to determine the resonant frequency of modes inside the rectangular DRA, in the absence of a closed-form solution.

The foundation of the CM theory is the decomposition of the total surface current distribution \bar{J}_T into orthogonal weighted eigencurrents, \bar{J}_n (Cabedo-Fabrés et al., 2007)

$$\bar{J}_T = \sum_{n=1}^N \alpha_n \bar{J}_n. \quad (3.2)$$

In (3.2), α_n is the complex weighted factor (modal weighting coefficient) of the n^{th} normalised eigencurrent to be determined. For the case of dielectrics these eigencurrents can be, surface currents obtained by the Surface Equivalence Principle (SEP) or, polarization currents obtained by the volume equivalence principle (VEP). In this dissertation and in FEKO the latter was used, specifically a hybrid MoM with VEP solution which employs a tetrahedral mesh to model the dielectric and its properties. Subsequently the modal fields inside the DRA are derived from the eigencurrents. Furthermore, the eigencurrents are real and independent of any source and only depends on the shape and size of the DRA. The

³ Here TCM and CMA are used interchangeably and in FEKO the term CMA is used.

current mode is calculated by the weighted eigenvalue equation as (Cabedo-Fabrés et al., 2007)

$$X(\bar{J}_n) = \lambda_n R(\bar{J}_n), \quad (3.3)$$

where λ_n are the eigenvalues, \bar{J}_n are the eigenfunctions or eigencurrents, X and R are the imaginary and real part of the impedance operator

$$Z = R + jX. \quad (3.4)$$

Since X and R in (3.3) are real and symmetrical matrices the eigenvalues are real and determine the reactive power of the n^{th} mode. The TCM thus gives physical insight into the radiation characteristics of an antenna structure through the interpretation of the respective surface current modes. FEKO has introduced an efficient solution to solve the generalised eigenproblem of (3.3) which is based on an iterative eigensolver (Ludick et al., 2012). The eigenvalues of the first six modes of the candidate rectangular DRA, mounted on an infinite Perfect Electric Conductor (PEC) ground plane, are shown in Figure 3.9. The DRA is made from LASF35 with dimensions, $a = d = 10.14$ mm, $h = 4.5$ mm, and $\epsilon_r = 20$.

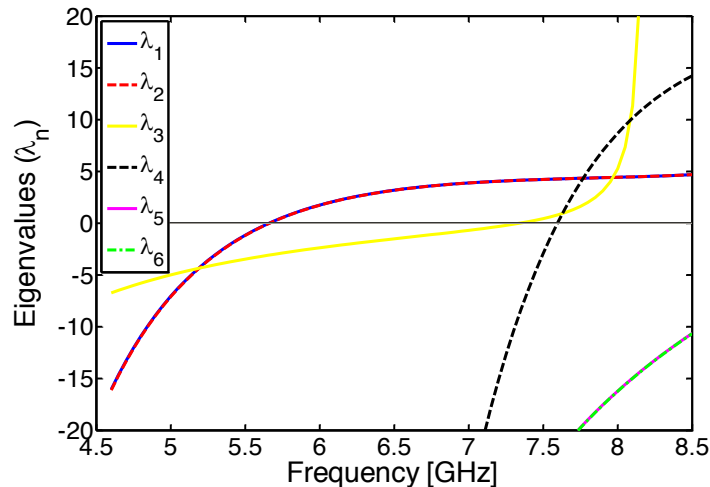


Figure 3.9: Eigenvalues for the candidate rectangular DRA on an infinite PEC ground plane

It is observed that the eigenvalues start negative, resonate and then remain positive. The sign of the eigenvalues determine the type of stored reactive power inside the DRA as follows: for $\lambda_n < 0$, the mode is storing electric energy, for $\lambda_n > 0$, the mode is storing magnetic energy and for $\lambda_n = 0$ the mode is resonant and thus radiates when excited. Therefore, a desired antenna system is where surface current modes with eigenvalues close to zero are mainly excited. Without any excitation and a feed's loading effects on the DRA's impedance, the resonant frequencies of the resonant modes of a DRA can thus be accurately determined. Furthermore, the accuracy of the CMA technique is independent of

the dielectric constant of the DRA. The accuracy of the DWM increases as the dielectric constant of a DRA increases.

In Figure 3.9 it can be seen that two modes have the exact same eigenvalues over frequency and is termed degenerated modes (modes with the same resonant frequency but different field configurations). This is due to the geometry of the rectangular DRA having two sides with identical length, $a = d = 10.14$ mm. By choosing the dimensions carefully, degenerate modes can be avoided. This is not possible for cylindrical and spherical DRAs since degenerate modes are always present (Mongia & Ittipiboon, 1997). Degeneracy is often unwanted since it increases the cross-polarization level of the intended mode and thus degrades the antenna's performance. For space communication applications, mode degeneracy can be beneficial since exciting two orthogonal modes allows for a CP antenna.

An alternative representation of the eigenvalues is the modal significance which is inversely dependent upon the eigenvalues and is stated as (Cabedo-Fabrés et al., 2007)

$$MS_n = \left| \frac{1}{1 + j\lambda_n} \right|. \quad (3.5)$$

The modal significance represents the normalised amplitude of the current modes. The normalised amplitude, similarly to the eigenvalues, only depends on the shape and size of a conducting or dielectric body and does not account for any excitation. The modal significance of the first six current modes of the candidate rectangular DRA are shown in Figure 3.10. Radiating modes are associated with a modal significance of unity.

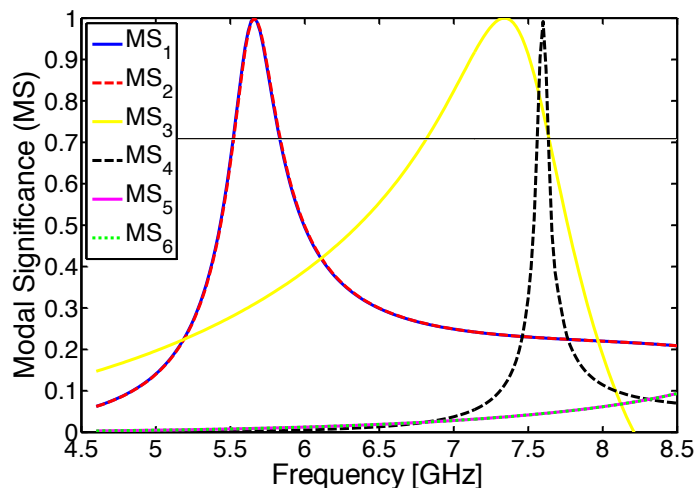


Figure 3.10: Modal significance of the candidate rectangular DRA on an infinite PEC ground plane

It is possible to determine the radiation bandwidth of each mode by translating the modal significance, half-power (*HP*) where the radiated power of the mode is half the power radiated at resonance and is stated as

$$MS_{HP_n} = \left| \frac{1}{1 + j\lambda_n} \right| = \frac{1}{\sqrt{2}} = 0.707. \quad (3.6)$$

The radiation bandwidth of the mode can then be expressed as the fractional bandwidth as

$$BW_n = \frac{f_U - f_L}{f_{res}}, \quad (3.7)$$

where f_U and f_L are the upper and lower frequencies respectively, with f_{res} being the resonant frequency. Furthermore, the modal quality factor can also be derived from the fractional bandwidth as

$$Q_{rad_n} = \frac{1}{BW_n}, \quad (3.8)$$

provided $Q_{rad_n} \gg 1$. The calculated radiation characteristics of the candidate rectangular DRA is summarised in Table 3.1 below.

Table 3.1: Simulated resonance frequency, radiating bandwidth and quality factor of the first four modes of the candidate rectangular DRA

Mode	f_{res} (GHz)	BW (%)	Q_{rad}
1	5.67	5.53	18.1
2	5.67	5.53	18.1
3	7.36	11.3	8.9
4	7.6	1	102.7

Where f_{res} is the resonant frequency, BW the bandwidth and Q_{rad} the resonant Q-factor of the n^{th} mode, respectively. In Table 3.1, modes 1 and 2 are degenerate (have the same resonant frequency) which is due to the equal two sides of the DRA. Both these modes are characterised by having their gain peaks toward zenith. The higher-order modes have difference characteristics to the fundamental modes and also have their maximum gain peaks towards the horizon.

Another representation of the eigenvalues is the characteristic angle defined as (Cabedo-Fabrés et al., 2007)

$$\alpha_n = 180^\circ - \tan^{-1} \lambda_n. \quad (3.9)$$

The characteristic angle represents the phase angle between a characteristic current, \bar{J}_n and the associated characteristic field, \bar{E}_n . From (3.9) it is observed that a mode is a good

radiator when $\alpha_n = 180^\circ$ and predominately stores, magnetic energy when $\alpha_n \approx 90^\circ$ and electric energy when $\alpha_n \approx 270^\circ$. It is also possible to determine the radiation bandwidth of a mode from the characteristic angles. The characteristic angles for the first six modes for the candidate rectangular DRA are shown in Figure 3.11.

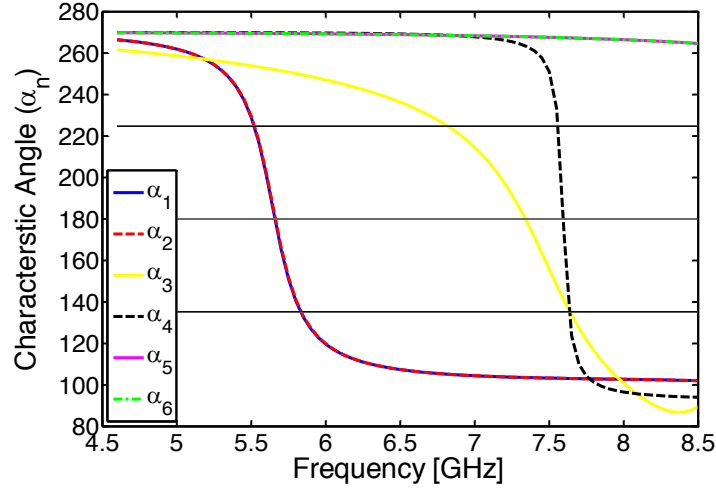


Figure 3.11: Characteristic angles for the candidate rectangular DRA on an infinite PEC ground plane

As can be deduced, for some wideband antenna structures the curves generated for the eigenvalues and modal significance can slowly approach the zero crossing or the maximum of unity respectively. For these wideband structures, the characteristic angle can impose difficulties to visually interpret the resonant frequency of a particular mode. It is due to the aforementioned reason that the characteristic angle representation is preferred as it is the most intuitive. Finally, the characteristic fields (modal fields) are obtained from the eigencurrents in equation (3.3) written as (Cabedo-Fabrés et al., 2007)

$$\begin{aligned}
 E_n(\bar{J}_n) &= Z(\bar{J}_n) & (3.10) \\
 &= R(\bar{J}_n) + jXR(\bar{J}_n) \\
 &= R(\bar{J}_n)(1 + j\lambda_n).
 \end{aligned}$$

The modal fields of the first six characteristic modes for the candidate rectangular DRA is shown in Table 3.2 below.

The resonant frequency for the candidate rectangular DRA and DRAs in literature, is summarised in Table 3.3. It is seen that the theoretical (DWM) values are between 4% to 6% lower than the measured values. Furthermore, the CMA and RCS are accurate methods to determine the natural (no loading effect from the feeding mechanism) resonant frequencies and Q-factors. The MoM is an accurate method to determine the resonant frequencies of DRAs including the loading effects of the feeding mechanism.

Table 3.2: Modal fields and radiation patterns for the candidate rectangular DRA on an infinite PEC ground plane

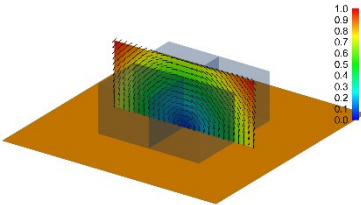
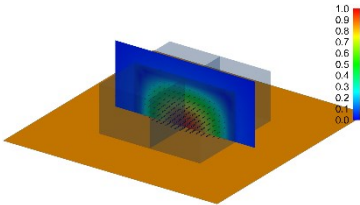
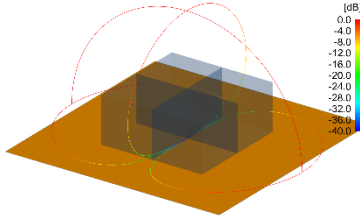
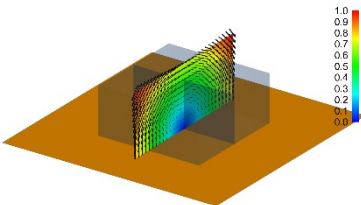
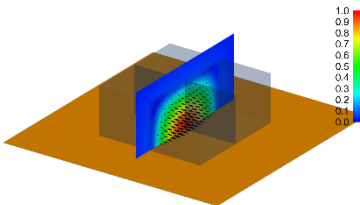
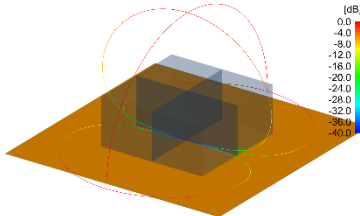
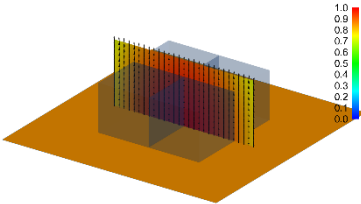
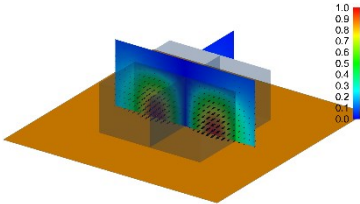
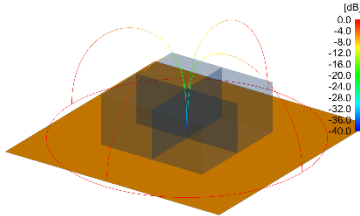
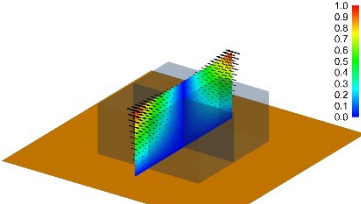
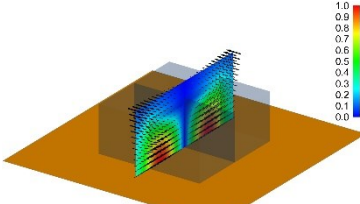
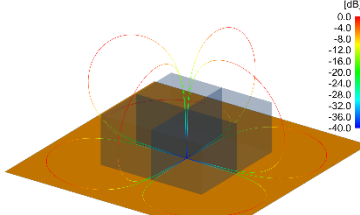
Mode Index	Resonant Mode	Modal fields		Modal radiation pattern
		E-field	H-field	
1	$TE^x_{\delta 11}$ (5.67 GHz)			
2	$TE^y_{\delta 11}$ (5.67 GHz)			
3	$TM^z_{11\delta}$ (7.36 GHz)			
4	$TM^z_{22\delta}$ (7.6 GHz)			

Table 3.3: Comparison of the simulated and measured rectangular DRA fundamental mode

Design	DWM [GHz]	Measured [GHz]	Error [%]	CMA (Simulation)		RCS (Simulation)		Probe feed (Simulation)	
				f_0 [GHz]	Error [%]	f_0 [GHz]	Error [%]	f_0 [GHz]	Error [%]
A	5.51	5.8	-5	5.67	-2.8	5.54	-0.5	5.58	-1.3
B	4.0	4.25	-5.9	4.27	-6.3	4.3	-7	4.12	-2.9
C	4.3	4.49	-4.2	4.48	-4	4.48	-4	4.45	-3.4

A⁴: $\epsilon_r = 20$, $\tan \delta = 6.3e^{-3}$, $a = 10.14$ mm, $b/2 = 4.5$ mm, $d = 10.14$ mm

B⁵: $\epsilon_r = 37.84$, $\tan \delta = 0.17e^{-3}$, $a = 9.31$ mm, $b/2 = 9.31$ mm, $d = 4.6$ mm

C⁶: $\epsilon_r = 37.84$, $\tan \delta = 0.17e^{-3}$, $a = 8.97$ mm, $b/2 = 4.485$ mm, $d = 8.97$ mm

Similar to the literature, the error in Table 3.3 is with reference to the DWM. A much more accurate result is achieved comparing the simulated and measured resonant frequency. With reference to Table 3.3, design A is the candidate DRA while designs B and C are those prototyped in literature. The measured results for designs B and C represent published data.

3.5 Conclusion

In this chapter the fundamental resonant modes of rectangular DRAs of different sizes were determined using various numerical methods. In general, a closer agreement for the resonant frequency is achieved with numerical techniques as compared to the DWM. The RCS method was used as a method to determine the resonant frequency since it eliminates probe effects. Currently, publications are mainly devoted to describing the geometry and its radiation behaviour of rectangular DRAs, with the design procedure not receiving as much consideration. CMA was used here to give physical insight into the radiation behaviour and resonant modes of the DRA as well as paying attention to the physics of the EM problem. Furthermore, CMA modes are in agreement with the RCS modes due to the polarization alignment of the eigencurrents and the incident waves.

⁴ This work

⁵ Mongia & Ittipiboon (1997)

⁶ Trueman et al. (1993)

Chapter 4 Integrated Solar Panel Antenna

4.1 Introduction

In this section, the electromagnetic effect that a triple-junction Gallium Arsenide (GaAs) solar cell has on a rectangular DRA is studied. The effect of the DRA on the solar cell's efficiency was measured. To prove the ISPA concept, a rectangular DRA with a dielectric constant, ϵ_r , of 37.84 was chosen, as this was often analyzed in the literature (Mongia & Ittipiboon, 1997, Trueman et al., 1995) and since access to a transparent dielectric material was not yet available. Note that a transparent material is preferred for maximum power transfer to the solar cell and for the power efficiency tests the LASF35 glass was sourced. A FEKO model of a rectangular DRA on top of a GaAs is shown in Figure 4.1. Like the previous section, various computational EM analysis techniques were used to analyze the models due to the model complexity. In FEKO, the MoM solver (with SEP) or hybridised MoM with the Finite Element Method (FEM) were used. This is to efficiently model the radiating metallic structures (solar cell contacts, antenna feed and DRA), using the MoM, while FEM is used for modeling the inhomogeneous structure of the multi-junction solar cell. The FEKO results are then compared with a time domain technique solver based on the FIT in CST.

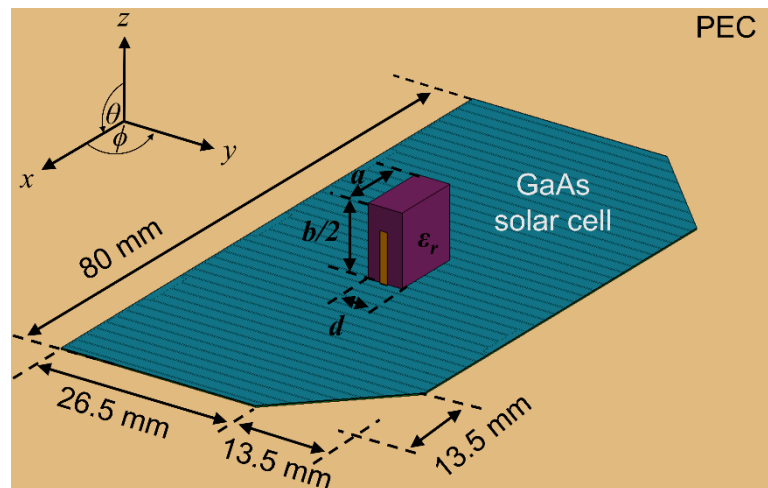


Figure 4.1: FEKO model of the rectangular DRA on top of a GaAs solar cell on an infinite PEC ground plane (Davids & Lehmsiek, 2014)

4.2.1 GaAs triple-junction Solar Cells

Triple-junction GaAs solar cells are made of three sub-cells, GaInP₂, GaAs and Ge. These sub-cells each have specific band gap energies and combined they absorb different parts of the solar spectrum giving a collective conversion efficiency of ~30%. The GaInP₂ sub-cell with a band gap energy of 1.42 eV absorbs the highest energy photons in the ultraviolet to visible part (300 nm – 660 nm) of the solar spectrum. The GaAs sub-cell has a band gap energy of 1.42 eV and absorbs high energy photons in the near-infrared part (660 nm – 880 nm) of the spectrum. Ge has a band gap energy of 0.67 eV and absorbs the lower energy photons in the infrared part (880 nm – 1900 nm) of the spectrum (Burnett, 2002). A 76.2 μm to 762 μm thick coverglass is bonded on top of the solar cell to protect it against cosmic radiation. This coverglass is made from fused-silica or specially formulated ceria doped glass types like CMX, CMG and CMO (Jones et al., 2006). Various anti-reflection and conductive coatings are applied to improve the conversion efficiency of the solar cell. The dielectric material that makes up the DRA is bonded on top the coverglass. It is thus important that the optical and mechanical properties of the DRA match those of the coverglass. The dielectric material should also have a wide transparency range (300 nm – 1900 nm) and high transmissibility (which will be discussed in section 4.3).

4.2 Effects of a GaAs Solar Cell on DRA

4.2.2 Parametric Study of the Solar Cell

To characterize the solar cell and its effects on the DRA, a parametric study was performed using a simplified model for the solar cell. The solar cell (including coverglass) was modelled as one homogeneous dielectric layer with an equivalent relative permittivity, $\epsilon_{r(eq)}$, given by (Chaudhary et al., 2010)

$$\epsilon_{r(eq)} = \frac{\epsilon_{r1}d_1 + \epsilon_{r2}d_2 + \epsilon_{r3}d_3 + \dots + \epsilon_{rn}d_n}{d_1 + d_2 + d_3 + \dots + d_n}, \quad (4.1)$$

where ϵ_{rn} and d_n are the relative permittivity and thickness of the n^{th} dielectric layer. Using equation (4.1), the resonant frequency for a rectangular DRA on top of a homogeneous solar cell model with various relative permittivity and thicknesses was simulated. The equivalent relative permittivity was varied in the range from 4 to 22 and the solar cell's total thickness, H_{SC} , was varied from 0.1 mm to 1 mm. The results, using the hybrid MoM/FEM method, are shown in Figure 4.2 and show that with an increase in the solar cell thickness the resonant frequency of the fundamental mode increases. When the thickness is kept constant and the permittivity of the solar cell is increased, the resonant frequency decreases.

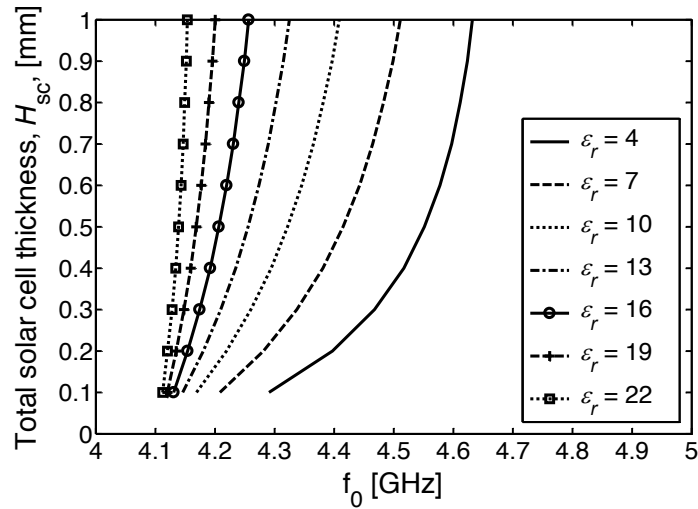


Figure 4.2: Resonant frequency for a rectangular DRA on top of a homogeneous solar cell model with various permittivity and thicknesses

As stated previously, the coverglass can be customized to suit a specific user requirement by selecting different coverglass types, anti-reflective coatings and glass thicknesses. Here, two glass types were investigated, CMX and CMG. A two-layer model that models the solar cell and glass separately will present a more accurate model than above. The solar cell thickness of 0.1455 mm (i.e., $H_{sc} = d_2 + d_3 + d_4$) was modelled as a homogeneous layer with an equivalent relative permittivity of 15.84. The coverglass thickness was varied from 0.05 mm to 1.05 mm and a relative permittivity of 4 and 6.7 were used for the CMX and CMG coverglass types respectively. The results of the hybrid MoM/FEM analyses are shown in Figure 4.3. The resonant frequency for the CMX coverglass is approximately 0.1 GHz higher than that of the CMG coverglass due to the higher dielectric constant of the CMG glass.

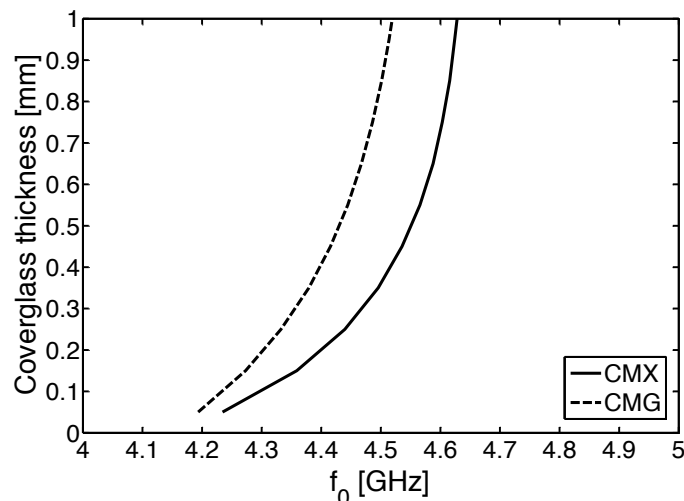


Figure 4.3: Resonant frequency for a rectangular DRA on top of a homogeneous solar cell with the CMX and CMG coverglass types of various thicknesses

4.2.3 Triple-junction Solar Cell Analysis

In this section, a GaAs solar cell with a cell area of 30.18 cm^2 is modelled. Initially the metallic contacts (illustrated in Figure 4.4) within the solar cell were not included in the model. With reference to Figure 4.4, the first sub-cell is constructed of GaInP_2 with a permittivity of $\epsilon_{r3} = 9.39$ and thickness of $d_2 = 0.5 \text{ }\mu\text{m}$. The second sub-cell is a GaAs cell with permittivity of $\epsilon_{r4} = 13.1$ and thickness $d_3 = 5 \text{ }\mu\text{m}$. The third cell is a Ge cell with permittivity of $\epsilon_{r5} = 16$ and thickness of $d_4 = 140 \text{ }\mu\text{m}$ ⁷. A $76.2 \text{ }\mu\text{m}$ to $762 \text{ }\mu\text{m}$ (customer specified) thick coverglass is bonded on top of the solar cell to protect it against cosmic radiation⁸. All analyses in this section use the same geometric parameters for the DRA as in section 3.3. The DRA material, LASF35, also offers radiation resistance suitable for space applications with a lifespan of up to 10 years⁹. This is far beyond the operational lifespan of CubeSats.

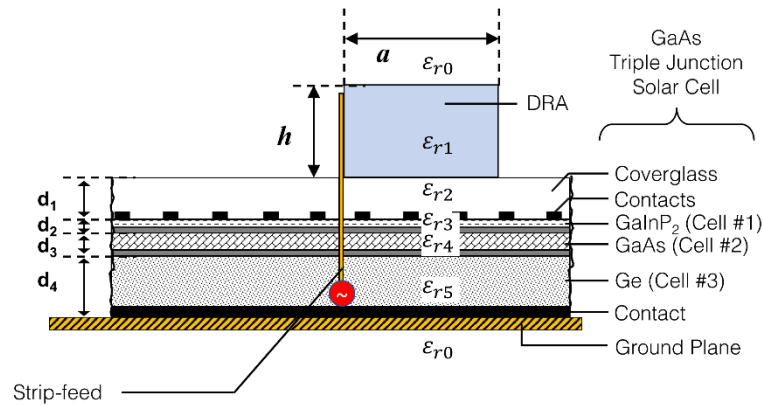


Figure 4.4: Cross-section of the transparent rectangular DRA on top of a triple-junction solar cell (Not to scale)

The solar cell was modelled as a homogeneous layer with a relative permittivity of 15.84 combined with a ceria doped CMX coverglass with thickness of $76.2 \text{ }\mu\text{m}$ and relative permittivity of 4 was used. The input reflection coefficient for this case is shown in Figure 4.5 and shows a shift in resonance from 4.1 GHz to 4.25 GHz and 4.27 GHz for the FEKO and CST models, respectively. The results above are consistent with the parametric study performed in section 4.2.2.

Finally, a model that includes the metallic contacts in the solar cell was modelled in both FEKO and CST. The input reflection coefficient of the model is shown in Figure 4.6 and shows additional resonances slightly above the resonant frequency. These are due to currents on the metallic contacts which can thus influence the radiation performance of the DRA.

⁷ <http://www.siliconfareast.com/sigegaas.htm>

⁸ http://www.azurspace.com/images/pdfs/HNR_0002490-00-03.pdf

⁹ http://glassfab.com/wp-content/uploads/2015/08/Schott_Optical_Cat.pdf

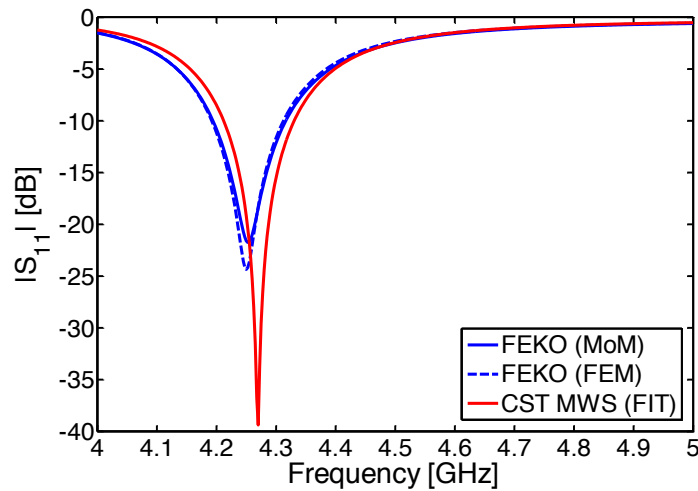


Figure 4.5: Simulated $|S_{11}|$ for a rectangular DRA placed on a GaAs solar cell without metallic contacts and on an infinite ground plane

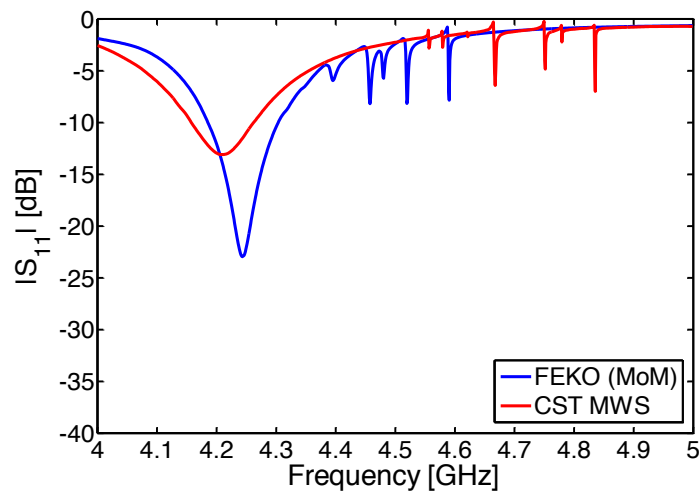


Figure 4.6: Simulated $|S_{11}|$ for a rectangular DRA placed on a GaAs solar cell with metallic contacts and on an infinite ground plane

The simulated surface currents for this configuration, at the identified resonances, are shown in Figure 4.7. The position and orientation of the DRA on the solar cell and the exact geometric parameters of the contacts will determine the frequencies of these resonances. For example, rotating the DRA by 90° around the z -axis will shift the resonances to higher frequencies, or by shortening (although not practical) the contact lengths in the y -axis will also shift the resonances to higher frequencies. Care thus needs to be taken when designing the DRA on a solar cell to prevent the contacts influencing the DRA.

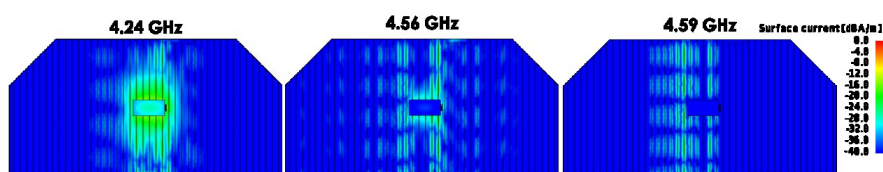


Figure 4.7: Simulated surface currents of the rectangular DRA placed on top of a GaAs solar cell (top view).

The radiation patterns are shown in Figure 4.8 and Figure 4.9. The radiation patterns are very similar to the case of the DRA without a solar cell, i.e., mounted on a ground plane. This then supports the feasibility of placing a transparent DRA on top of a triple-junction GaAs solar cell.

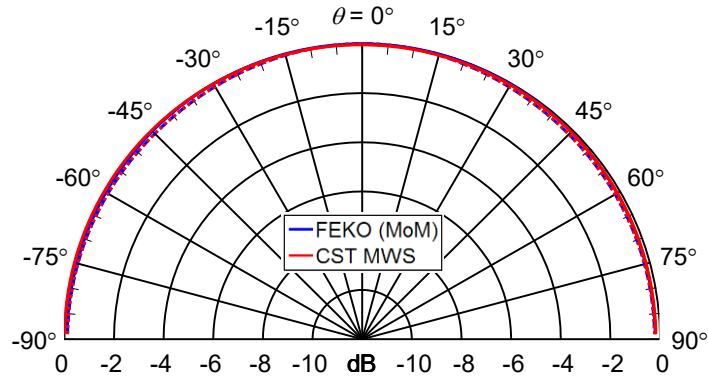


Figure 4.8: Simulated radiation pattern of the rectangular DRA, placed on an infinite ground plane (solid line) and placed on an infinite ground plane on top of a GaAs solar cell (dashed line). $\phi = 0^\circ$

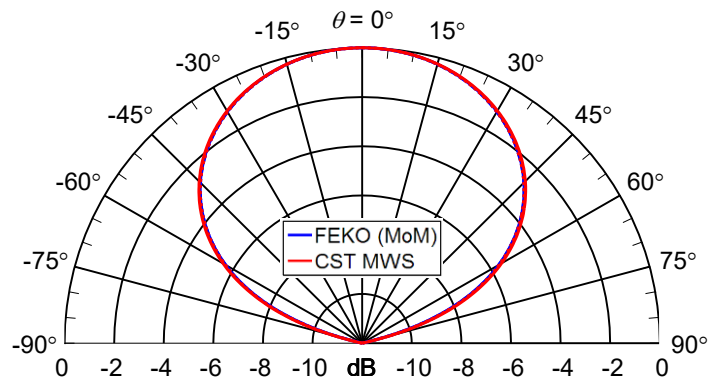


Figure 4.9: Simulated radiation pattern of the rectangular DRA, placed on an infinite ground plane (solid line) and placed on an infinite ground plane on top of a GaAs solar cell (dashed line). $\phi = 90^\circ$

As stated previously, the probe-feed was considered for its practical benefits over the aperture feed, initially pursued at conception of this dissertation. The aperture concept was to etch an aperture on both the cathode of the solar cell and the ground plane of the solar cell's PCB. The slot was orientated with the slot's E-field orthogonal to the metallic contacts (anode) of the solar cell and can propagate unperturbed through the cell and thus excite the $TE_{1\delta 1}^y$ mode in the DRA. Although simulation results seemed promising, the space needed for a cavity on the inside of the CubeSat was discouraging and this feeding arrangement was abandoned.

4.2.4 Single rectangular DRA measurements

Due to the high cost of space solar cells, TrisolX Solar Wings were sourced as a proof of concept. These solar cells are cut-off 28% Azurspace space-qualified solar cell wafer¹⁰. A single cell was mounted directly on a 2.5 mm aluminium panel using standard Kapton tape as isolation and is shown in Figure 4.10.

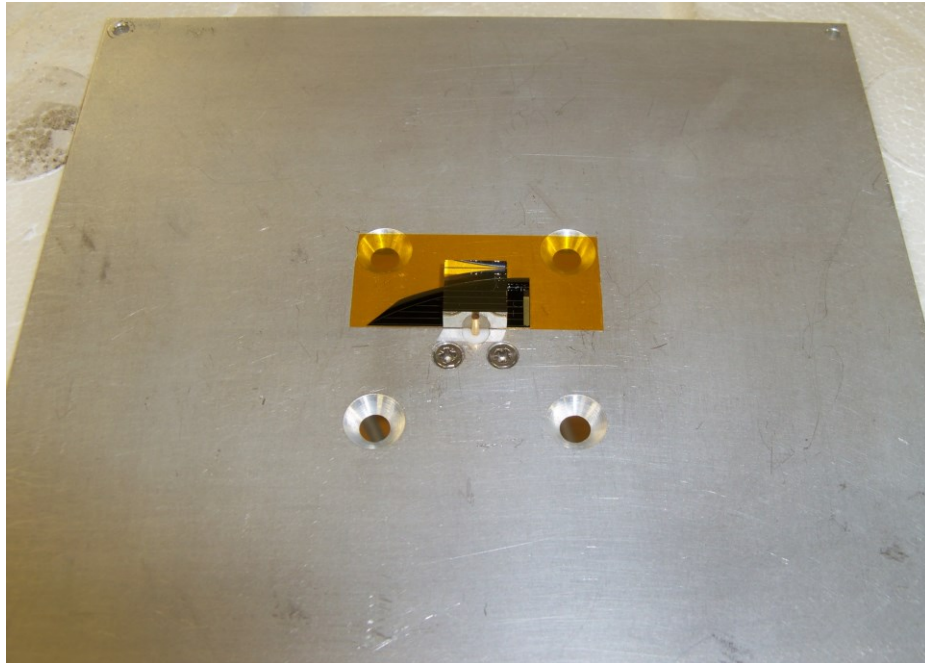


Figure 4.10: Single transparent DRA on top of a GaAs solar cell without electrical connections

The measured input reflection coefficient for the single element is shown in Figure 4.11. The antenna was measured with and without the presence of the solar cell underneath the DRA. An attempt to simulate the TrisolX Solar Wings solar cell in FEKO was not made and the simulated result is therefore absent. The simulation model comprises of the rectangular DRA without (solar cell) on top of a 150 mm x 150 mm x 2.5 mm aluminium ground plane.

The simulated and measured resonant frequencies are 5.6 and 5.8 GHz, respectively. Relative to the DWM an upward shift of 1.7% and 5.2% was observed for both the simulated and measured resonant frequencies, respectively. It should be noted that the DWM is an approximation and does not take into effect the inductive loading caused by the coaxial probe. A frequency shift of less than 2% is thus consistent with that found in literature (Mongia & Ittipiboon, 1997). The frequency shift in the measured result can be attributed to both probe effects and air gaps (Luk & Leung, 2003) introduced by two countersunk screws which the DRA partially rest on. Four countersunk screws are used to secure the coaxial probe, in the form of a Sub-miniature version A (SMA) connector, to the aluminium ground plane (seen in Figure 4.10).

¹⁰ <http://www.trisolx.com>

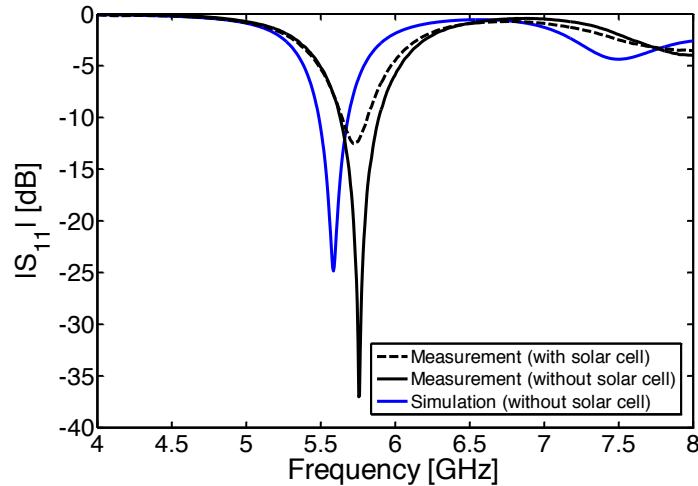


Figure 4.11: $|S_{11}|$ for a rectangular DRA placed on a GaAs solar cell on a 150 mm x 150 mm x 2.5 mm aluminium ground plane

The test setup for the far-field patterns and gain measurements was an anechoic chamber at Alaris Antennas (formerly Poynting Antennas). A VNA was used over the frequency range 4 GHz to 8 GHz with the antenna mounted vertically in the chamber. An azimuth sweep was done for both cases with and without the solar cell. For the gain measurement the gain transfer method was used to calculate the boresight gain using an A-INFO standard gain horn as a gain reference. An identical A-INFO horn was used as a source antenna throughout the measurements. The co-pol E -plane for the DRA with and without the solar cell is shown in Figure 4.12. The H -plane is shown in Figure 4.13. These patterns are plotted at 5.6 GHz and 5.8 GHz respectively and are similar to that of a short magnetic dipole.

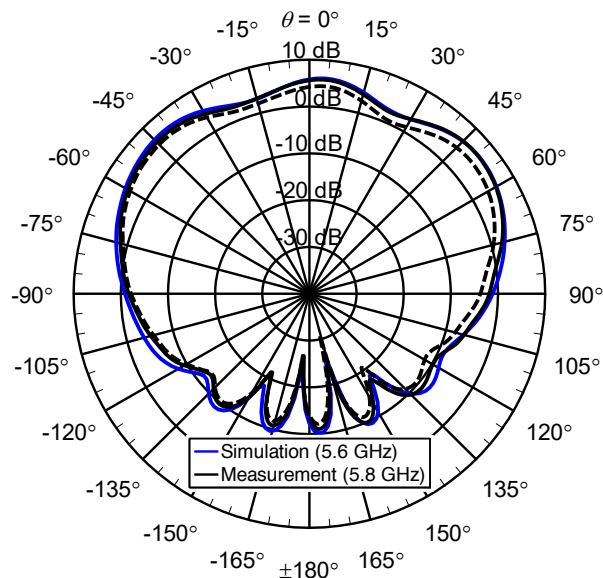


Figure 4.12: Simulated and measured E-plane at 5.6 and 5.8 GHz, respectively, for the single rectangular DRA placed on a 150 mm x 150 mm x 2.5 mm aluminium ground plane ground. Without the GaAs solar cell (solid line) and with the GaAs solar cell (dash-dot line) between the DRA and ground plane

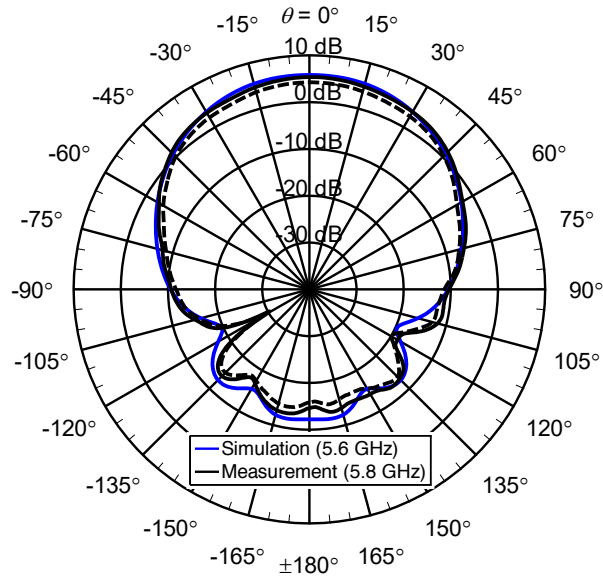


Figure 4.13: Simulated and measured H-plane at 5.6 and 5.8 GHz, respectively, for the single rectangular DRA placed on a 150 mm x 150 mm x 2.5 mm aluminium ground plane ground. Without the GaAs solar cell (solid line) and with the GaAs solar cell (dash-dot line) between the DRA and ground plane

The realised gain for the DRA with and without the solar cell is shown in Figure 4.14. The peak simulated gain, without the solar cell, amounts to 5.83 dBi at 5.6 GHz. The peak measured gain, without the solar cell, amounts to 5.7 dBi at 5.8 GHz. For the case with the solar cell, the peak measured gain reduced by 1.5 dB to 4.2 dBi at 5.8 GHz. The reduction in gain correlates with a combination of mismatch loss, seen in Figure 4.11, and dielectric loss of the solar cell.

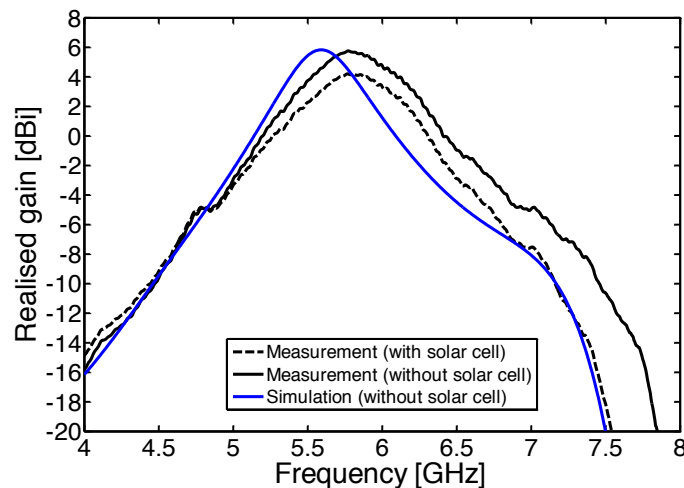


Figure 4.14: Realised gain of the rectangular DRA placed on top of a 150 mm x 150 mm x 2.5 mm aluminium ground plane for the TE_{101}^y mode

The above experiment demonstrated that the effect of the solar cell on the DRA's electromagnetic performance was minimal. An experiment investigating the effect of the DRA on the solar cell's efficiency followed.

4.3 Effects of the DRA on a GaAs Solar Cell

It is important to match the transmittance of the transparent dielectric material to the spectral response of the solar cell. The published spectral response for both the solar cell (AZUR SPACE, n.d) and the candidate glass materials are plotted on top of one another and is shown in Figure 4.15. Figure 4.15 shows the individual responses of each sub-cell with the colours corresponding to the wavelengths in the optical spectrum. The glass types with increasing refractive indexes are Borosilicate crown glass (P-BK7), Sapphire (Al_2O_3) and LASF35 (Lanthanum dense flint).

The transmittance shown in Figure 4.15 includes the losses attributed to multiple reflections and material absorption losses for a 4.5 mm thick substrate. As can be seen, the losses incurred by LASF35 is the highest which is typical of high index glass types. Also, lowest refractive index glass types (such as P-BK7) show high transmittance down to short wavelengths in the ultraviolet range. Ideally a glass candidate with good transmittance in the same spectral range as the solar cell is preferred however this constitutes a bigger antenna due to the low dielectric constant. To reduce the reflections and absorption of high index glass anti-reflective coatings and surface treatments are often used. These techniques were not employed in this dissertation however, the interested reader is referred to the glass manufacturer, SCHOTT, for further information¹¹.

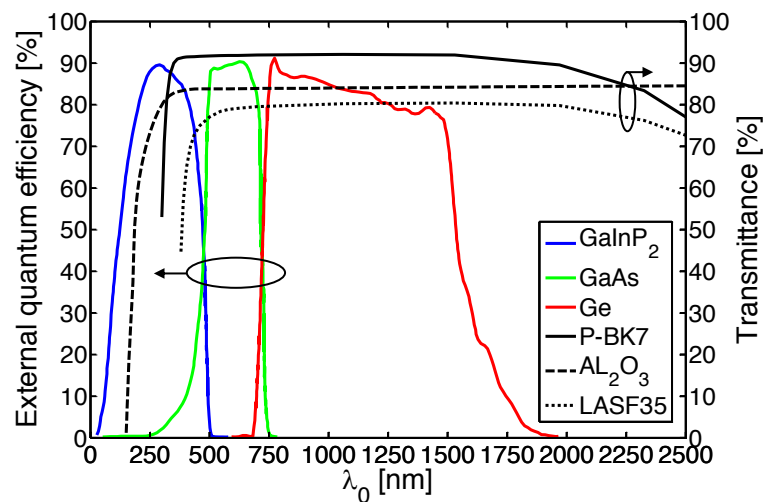


Figure 4.15: Efficiencies of the GaAs solar cell vs transmittance of candidate glass types

To measure the effect of the transparent DRA on the solar cell's efficiency, a test circuit was constructed. The circuit consists of a single TrisolX Solar Wings solar cell mounted on a

¹¹ Information on anti-reflection coatings [12 February 2020]:

https://www.schott.com/advanced_optics/english/products/optical-components/optical-filters/interference-filters/ar-filters.html.

Information on optical filter glass [12 February 2020]:

https://www.schott.com/d/advanced_optics/8c2cb5d1-4fa1-4b55-ad43-fef20ad89ad4/1.14/schott-catalog-optical-filter-glass-2020-row.pdf.

prototyped PCB. The solar cell was electrically connected to a collection of load resistors to measure the voltage and then determine the current to produce the I-V curves of the solar cell. The electrical circuit diagram of the solar cell prototype PCB is shown in Figure 4.16.

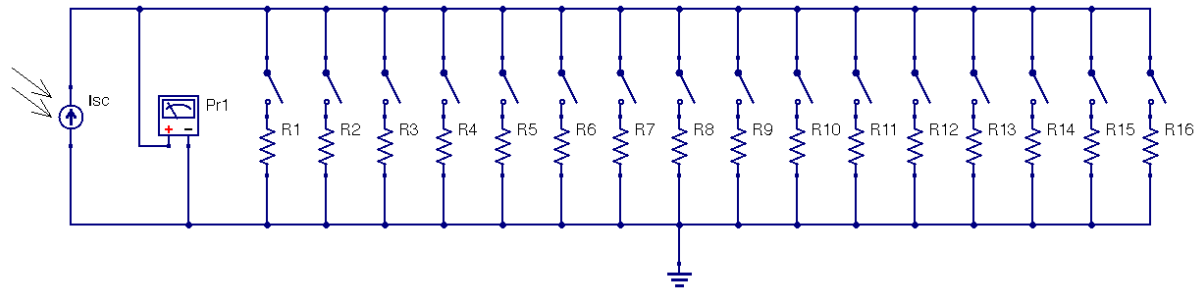


Figure 4.16: Solar cell efficiency test circuit

From the solar cell's datasheet and using Ohm's law, the I-V curve data was used to determine the corresponding load impedances. Standard resistor values as close as possible to the calculated impedances were sourced and their values given in Table 4.1.

Table 4.1: Load resistor values used to measure the I-V curve

Resistor	R ₁	R ₂	R ₃	R ₄	R ₅	R ₆	R ₇	R ₈	R ₉	R ₁₀	R ₁₁	R ₁₂	R ₁₃	R ₁₄	R ₁₅	R ₁₆
Ohm [Ω]	18	22	47	68	100	120	150	180	200	240	270	330	470	680	820	1k

In the absence of a professional solar simulator, the ISPA was exposed to direct sunlight with a voltage measurement taken, for each load resistor, for case I (the solar cell without the DRA) and then for case II (the solar cell with the DRA placed on top). The measurement was done using a Fluke 115 digital multimeter to measure the voltage drop across the surface mounted load resistors, which all are connected to a common ground and switched in and out of the circuit manually throughout the measurement. The Fluke 115 has a resolution of 1 mV for a voltage range of 6 V. The test setup is shown in Figure 4.17 and was positioned so as to ensure normal incidence and took place on the premises of the South African National Antenna Test Range, Paardefontein on 09/12/2017. The weather on the day was 28°C with passing clouds. The test commenced at a time where no visible clouds passed in front of the sun which was 13:00 pm and concluded at 13:10 pm.

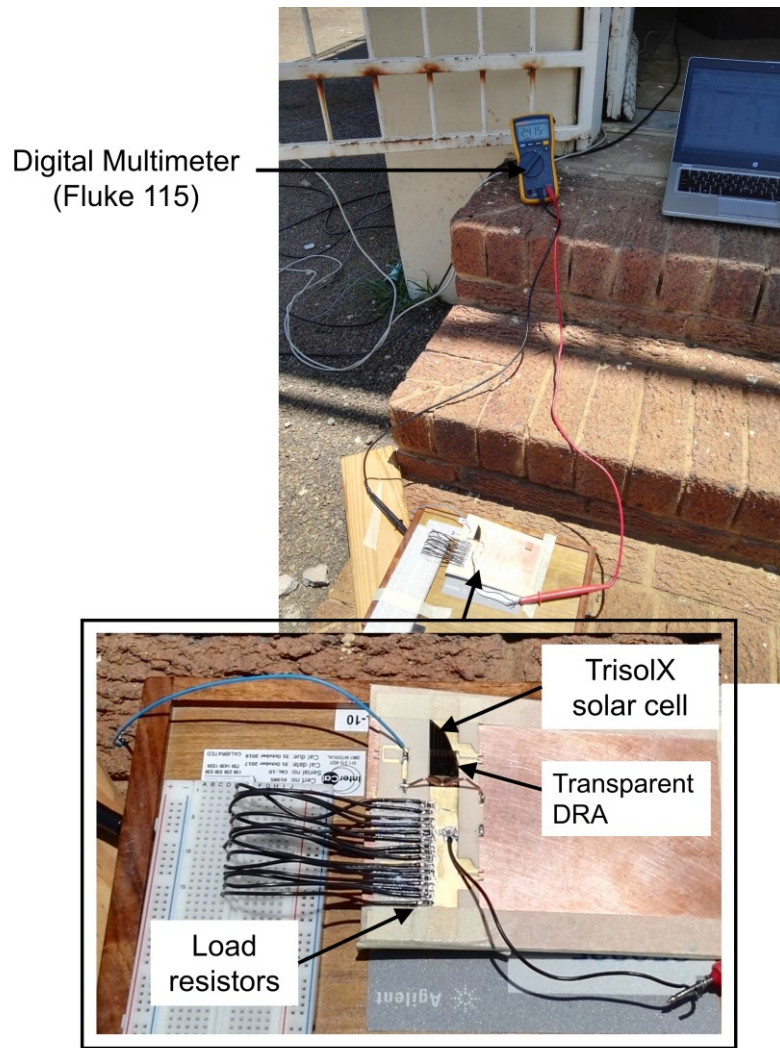


Figure 4.17: Solar cell efficiency test setup

Figure 4.18 shows the measured results obtained for the I-V curves. The power produced by the solar cell is calculated by the formula, $P = IV$ and is shown in Figure 4.19.

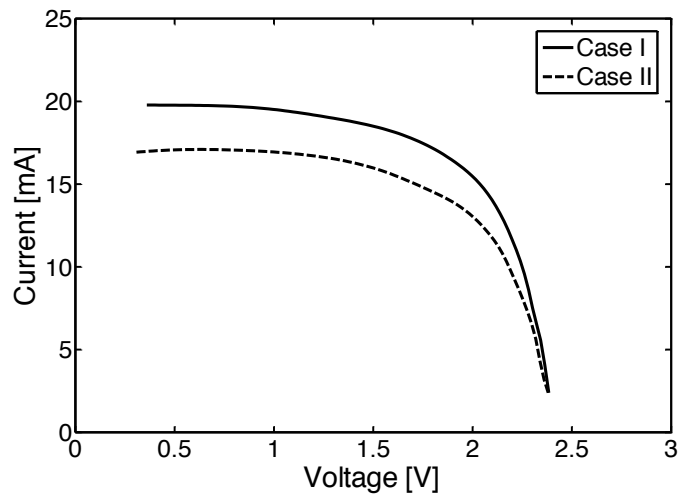


Figure 4.18: Measured current and voltages of the GaAs solar cell, with and without the DRA; Case I: without DRA (solid line) and Case II: without DRA (dashed line).

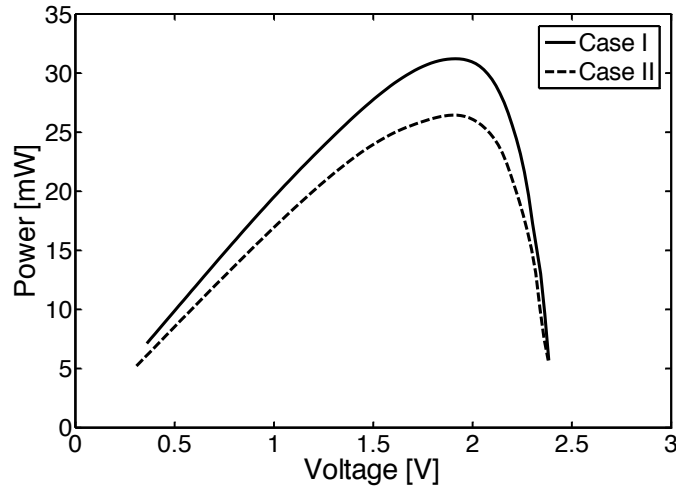


Figure 4.19: Power output of the GaAs solar cell with and without the DRA; Case I: without DRA (solid line) and Case II: with DRA (dashed line)

As can be seen from Figure 4.18 and Figure 4.19 the results shows that the DRA has an effect on the performance of the solar cell. A parameter signifying the quality of the solar cell is the Fill Factor (FF). This parameter is essentially a comparison of the maximum power to the theoretical power that the solar cell can produce. The FF is determined as (Baquedano et al., 2017)

$$FF = \frac{(I_{mp} \times V_{mp})}{(I_{sc} \times V_{oc})}. \quad (4.2)$$

Another qualitative parameter is the solar efficiency of the solar cell, defined as ratio of the output power compared to the solar power input. The output power is often taken at the maximum power point. The input power is taken as the product of the irradiance of the incident light, G , and the Active Collective Area (ACA). The solar efficiency can be determined as (Baquedano et al., 2017)

$$\eta = \frac{P_{out}}{P_{in}} = \frac{P_{mp}}{P_{in}} = \frac{(I_{sc} \times V_{oc} \times FF)}{(G \times ACA)}. \quad (4.3)$$

The measured results are summarised in Table 4.2 confirming the practical use of LASF35 as a transparent DRA for integrated solar panel antennas.

Table 4.2: Measured Electrical Parameters of GaAs solar cell with and without DRA

Configuration	V_{oc} [V]	V_{mp} [V]	I_{mp} [mA]	P_{mp} [mW]	FF [%]	η [%]
Datasheet	2.62	2.33	14.6	33.9	78.54	26.12
Case I (without DRA)	2.40	1.91	16.3	31.2	66.20	24.01
Case II (with DRA)	2.39	1.90	13.9	26.4	65.62	20.34

In Table 4.2, V_{oc} is the open-circuit voltage, V_{mp} and I_{mp} are the voltage and current at the maximum power point, P_{mp} . The solar efficiency, η was calculated with the input power, G of

Air Mass (AM) 1.5 global standard which defines 1 Sun as 100 mW/cm^2 . The ACA for the TrisolX Solar Wings is 1.3 cm^2 . The datasheet stipulates a solar efficiency of 28% however, using (4.3) an efficiency of 26.12% was calculated using the datasheet's I-V curve. The measured FF and efficiency for Case I is not identical to that presented in the datasheet. The difference can be attributed to the test conditions. For this reason, Case I is taken as the reference state with a measured efficiency of 24%. For Case II the efficiency measured 20.34%. Confirmation of this result is required and a test using a professional sun simulator is proposed.

4.4 Conclusion

The effect of a triple-junction solar cell on the radiation performance of a rectangular DRA was investigated by means of full-wave computational electromagnetic analyses and measurements. Various numerical techniques were used for the analyses and validation of the results, namely a MoM/SEP and MoM/FEM hybrids in FEKO, as well as the FIT in CST. The resonant frequency of the fundamental TE_{101}^y mode of a rectangular DRA on a ground plane shifted slightly higher in frequency when placed on top of a triple-junction solar cell. This is due to probe loading and air-gaps introduced by the mounting screws of the feed connector. A reduction in the realised gain is seen which is attributed to a combination mismatch loss and dielectric loss of the solar cell.

A parametric study of the solar cell showed that even for a large range of solar cell parameters the shift in resonant frequency is relatively small. Coupling to the metallic contacts in the solar cell can cause resonances which could interfere with the DRA. The frequencies of these resonances are a function of the geometrical parameters of the metallic contacts and the DRA's position and orientation on the solar cell. It can be expected that the DRA's performance is most effected when positioned so that the resonant mode's E-fields are aligned with the metallic contacts of the solar cell, thus allowing for more energy to couple from the DRA to the solar cell.

In the absence of a professional solar simulator, the effect of the DRA on the solar cell was measured using an experimental test setup. A difference in solar efficiency of 4% was observed between the case of a bare solar cell and the case with the DRA placed on top of the solar cell. Some difference could not be quantified due to the limited test setup. This loss in efficiency can be attributed to absorption and reflection losses inherent to high index (refractive index) glass types such as LASF35.

Chapter 5 A Beam-Steerable Back-to-Back Yagi-Uda DRA Array

5.1 Introduction

For satellite communications, the preferred radiation coverage pattern is the shaped conical or “isoflux” pattern. The isoflux pattern is characterised by an increased gain at low elevation angles to compensate for the increased path loss, related to the larger distance between a ground station and spacecraft.

CubeSat missions lacking a high-precision attitude determination and control system typically make use of low gain VHF/UHF monopoles or dipoles (ISIS, n.d). This is due to the pointing accuracies needed by high-gain antennas. To support high data rates, antennas with medium gain and wide coverage are preferred. Isoflux antennas such as nondeployable helices and horns (Ravanelli et al., 2010) are impractical on-board CubeSats due to their physical size. These conventional radiators are often miniaturized (Hebib et al., 2011; Choi et al., 2013) but at frequencies below X-band (8 GHz to 12 GHz), miniaturization efforts are challenging.

To reduce the cost of phased arrays, pattern reconfigurable antennas often use reactive elements in conjunction with parasitic radiating elements to achieve beam-steering (Nikkhah et al., 2013). In the previous chapters the EM properties of a single rectangular DRA was investigated which demonstrated a measured gain of > 5 dBi. To increase this gain, the DRA can be operated at higher-order modes (Petosa & Thirakoune, 2011) or combined with several DRA elements to form a DRA array (Kishk, 2003). Combining mutual coupling into the design of arrays can lead to favourable radiation characteristics, such as the Yagi-Uda antenna. In this chapter the design methodology and measured results for a back-to-back Yagi-Uda DRA array is reported. Initially, the antenna coverage and gain requirement for the array had to be derived.

5.2 Antenna Coverage Pattern and Gain Requirement

The orbital parameters of a LEO satellite continuously change throughout its orbit. The communication system’s gain, as seen from a ground station, is related to the slant range by the R_d^{-2} law, where R_d is the slant range between a ground station and a satellite. The required antenna coverage pattern and required gain (G_{req}) is dependent on the spacecraft’s

orbital height, H_{sat} , and elevation angle, θ_{gs} . As the spacecraft travels from zenith ($\theta_{gs} = 90^\circ$) to horizon ($\theta_{gs} = 0^\circ$) the slant range and path loss varies from a minimum to a maximum. The corresponding antenna gain must thus progressively increase to a maximum at the horizon to compensate for this increase in path loss. The relationship between the slant range, R_d , the elevation angle, θ_{gs} , and the beam-pointing angle, θ_p , is given in equations (5.1) and (5.2) respectively.

$$R_d = \sqrt{(R_e + H_{sat})^2 - R_e^2 \cos^2(\theta_{gs})} - R_e \sin(\theta_{gs}), \quad (5.1)$$

$$R_d = (R_e + H_{sat}) \cos(\theta_p) - \sqrt{R_e^2 - (R_e + H_{sat})^2 \sin^2(\theta_p)}, \quad (5.2)$$

where R_e is the Earth radius. The orbital parameters are illustrated in Figure 5.1 showing how the required antenna gain varies with the satellite at different positions in its orbit. Furthermore, the beam-pointing angle is defined from the nadir-axis.

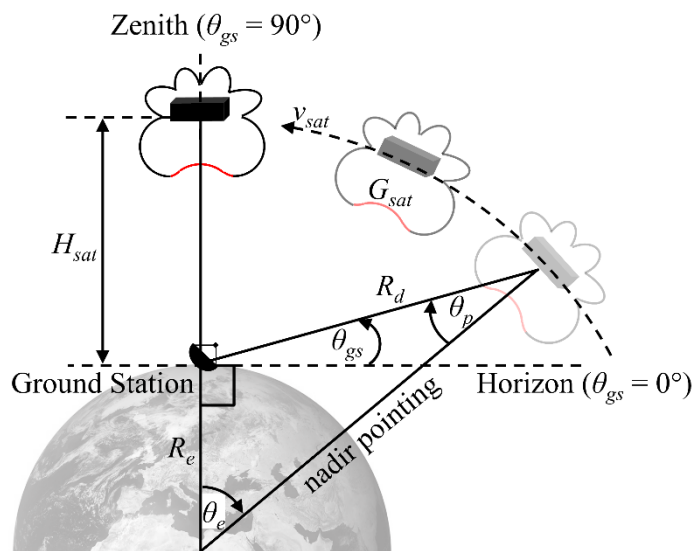


Figure 5.1: Satellite link path with required radiation pattern relative to the ground station

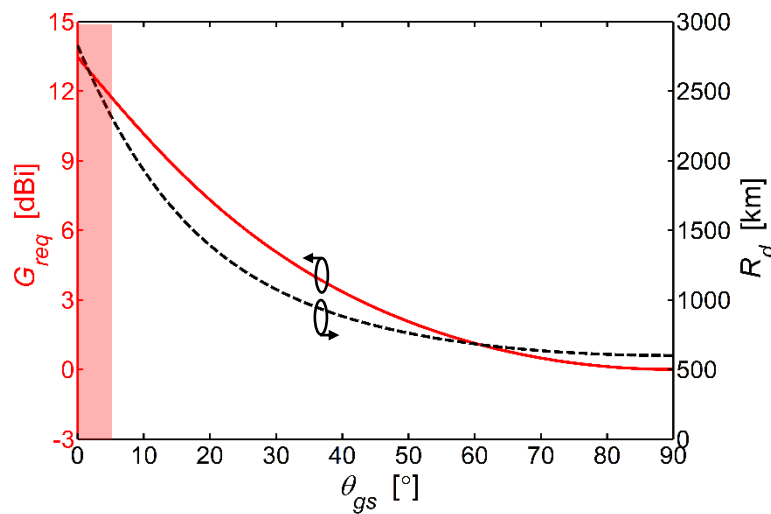
Table 5.1 shows how the orbital parameters vary from the horizon to zenith. Here a ground station height of zero was assumed. The path loss column shows that, for a satellite in a 600 km orbit, the required gain variation from zenith to the horizon is 13.47 dB. From the spacecraft antenna's point of view, i.e., the beam-pointing angle, θ_p , this translates to a maximum gain at 66.1° and a minimum gain at 0° . This results in an antenna beam coverage of 132.2° .

Since the minimum required gain is mission specific and obtained from a link-budget, the gain presented here is the normalised (to zenith pointing) antenna gain pattern.

Table 5.1: Relationship between the orbital parameters for a satellite in a 600 km orbit

Elevation angle, θ_{gs} [°]	Slant range, R_d [km]	Beam-pointing angle, θ_p [°]	Path loss, L [dB]	Required gain, G_{req} [dBi]
0	2819	66.1	176.4	13.47
5	2328	65.6	174.7	11.78
15	1626	62.0	171.6	8.66
30	1075	52.3	168.0	5.07
45	815	40.3	165.6	2.66
60	683	27.2	164.1	1.13
75	619	13.7	163.2	0.27
90	600	0	162.9	0

It is worth mentioning that practically the ground station is unable to communicate with the satellite when it is at the horizon ($\theta_{gs} = 0^\circ$). This is due to terrestrial obstructions and the ground station's antenna positioner limits. An elevation angle of 5° was thus used as the horizon limit, which translates to a maximum required gain of 11.78 dBi. The required gain profile and slant range relative to the ground station is shown in Figure 5.2.

**Figure 5.2: Required gain and slant range over elevation angle for a satellite in a 600 km orbit**

An antenna with the radiation characteristics as stated above is said to have an isoflux coverage pattern. The geometry and excitation phase of the array presented here were optimised to generate an isoflux pattern formed by the gain envelope of the peak gains for all possible steered beams.

5.3 Design Methodology

The radiation performance of a DRA array depends on the geometry and dimensions of the DRA elements, their spacing, excitation, feeding arrangements and operating modes. By varying the excitation phase and or amplitude of the elements in the array the radiation

pattern can be controlled and steered (Balanis, 2005:283). Pattern reconfigurable antennas, as used in radar systems, is used to discriminate between signals from intended sources whilst avoiding unwanted interferers from other directions.

In traditional phased arrays, beam-steering is accomplished by employing expensive phase shifters for each driven element. To minimize the cost of phased arrays, through minimizing the amount of phased shifters, pattern reconfigurable arrays implemented in microstrip typically employ reactive elements such as varactors, PIN diodes or RF Microelectromechanical System (MEMS) switches to introduce a phase shift (Gray et al., 1998).

To further reduce the cost, the amount of driven elements in the array can be reduced by using parasitic radiators such as the Yagi-Uda antenna (Uda & Mushiake, 1954). The Yagi-Uda antenna consists of a linear end-fire array of resonant elements comprising of a driven element, which couples energy electromagnetically to a number of parasitic elements operating as directors or reflectors. The amplitude and phase of the coupled current on the parasitic elements are controlled by their geometry and position relative to the driven element. The elements are typically metallic wires or microstrip patch elements.

Recently, DRAs were considered as elements in a Yagi-Uda array (Hesselbarth et al., 2013; Kishk, 2005). In Hesselbarth et al. (2013) Yagi-Uda DRA arrays with two and three elements showed a simulated directivity of 6 dBi and 8 dBi, towards end-fire, respectively. In Kishk (2005) two Yagi-Uda DRA arrays with broadside radiation patterns showed gains of 2.7 dBi and 3.6 dBi for a two and three element array respectively. The elements were stacked on top of each other above a ground plane. By placing the parasitic elements (directors) next to the driven element, the radiation pattern can be controlled and scanned between broadside and end-fire using reactive loading (Nikkhah et al., 2013). This array is limited to a scan angle of $\pm 30^\circ$. There is merit in using a back-to-back Yagi-Uda array configuration to extend the scanning limits and gain of the array. The radiation performance of a back-to-back Yagi-Uda dipole array was reported in (Lehmensiek & Khotso, 2014). The array achieved a scanning range of up to $\pm 60^\circ$, $\pm 70^\circ$ and $\pm 80^\circ$ for an array with no director, one director and two directors respectively.

In this dissertation, a back-to-back Yagi-Uda DRA array mounted on a perfect electrically conducting ground plane was designed. The FEKO model of this array is shown in Figure 5.3.

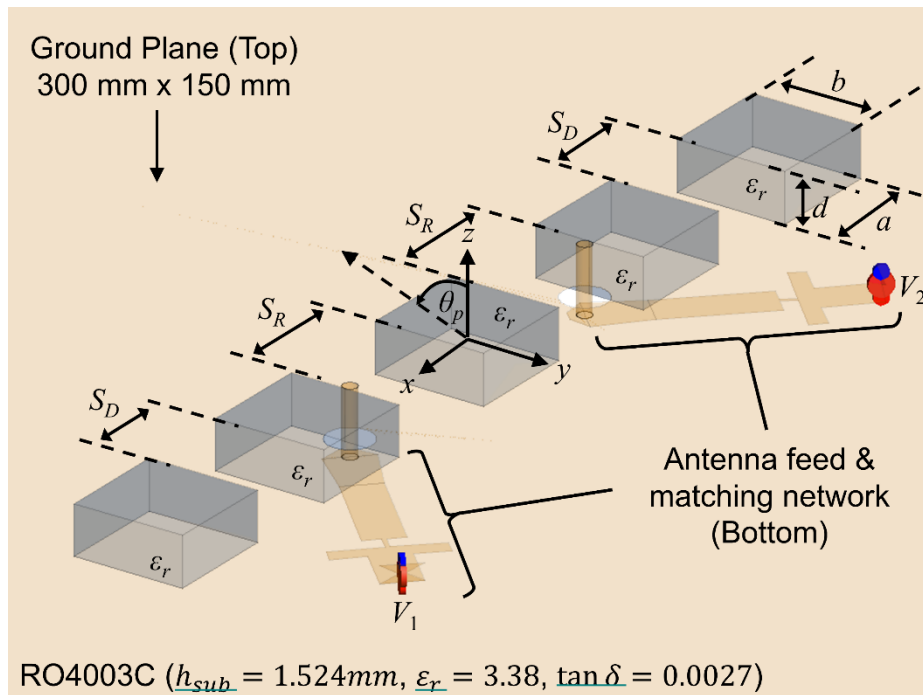


Figure 5.3: Geometrical configuration of the back-to-back Yagi-Uda DRA array (Davids & Lehmensiek, 2016)

The scanning performance for DRA arrays can vary depending on the operating mode and whether the elements are coupled in the H-plane or E-plane. The proposed DRA array has its elements coupled in the E-plane. This array will be mounted on the solar panel of a small satellite (3U CubeSat) to form an ISPA (Davids & Lehmensiek, 2016). This mechanical configuration limits the feeding mechanism to two probe-fed driven elements. The probes are each connected to a beamforming network on the bottom layer of a double-sided PCB with the top layer serving as the ground plane of the array.

In Figure 5.3 one element is excited with a voltage, $V_1 = 1\angle 0^\circ V$, and the other voltage source has $V_2 = 1\angle 0^\circ V$. Through optimisation the phase of V_2 is determined as a function of the beam-pointing angle, θ_p . The pointing angle is defined from the z -axis in the E-plane of the array. A satellite mounted antenna that can optimise its gain pattern as the orbital properties of the satellite change during an over-pass is highly favoured to maximise the contact time between the satellite and ground station. The effect of the antenna pattern on the communication time between a nadir pointing Low Earth Orbit (LEO) satellite and a ground station was previously investigated in (Khotso et al., 2011). This concept is employed here by optimizing the antenna gain pattern for constant flux density at a satellite ground station thus maximizing the contact time between a satellite in LEO and a ground station.

5.4 DRA Array Design

The proposed array consists of five identical transparent DRA elements with a common reflector, a driven element in the $+x$ -axis and another in the $-x$ -axis, both at a distance S_R away from the reflector. Each driven element has one parasitic DRA element as director at a distance S_D away. For ease of manufacturing all the DRA elements are geometrically identical with the same dimensions as the DRA designed in section 4.2.4. The driven elements are excited with voltages, V_1 and V_2 . The probes are in turn connected to a feeding network on the bottom layer of a Rogers RO4003 ($\epsilon_r = 3.38$, $\tan \delta = 0.0027$) substrate and fixed to a 300 mm \times 150 mm aluminium ground plane. Shown in Figure 5.4 and Figure 5.5 is the top and bottom side of the fabricated array, respectively.

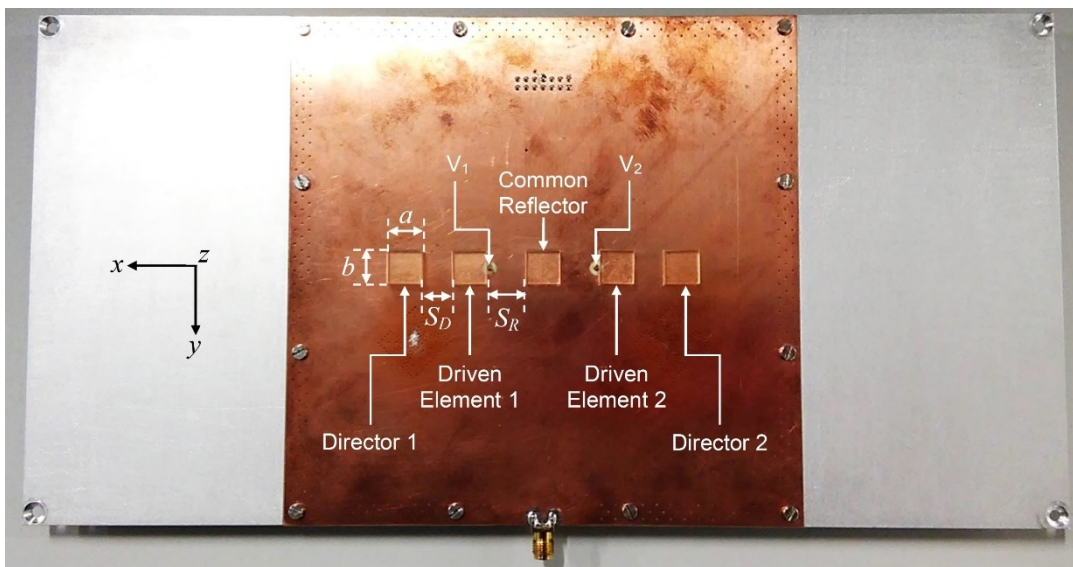


Figure 5.4: Top view of the fabricated back-to-back DRA array showing the DRA elements

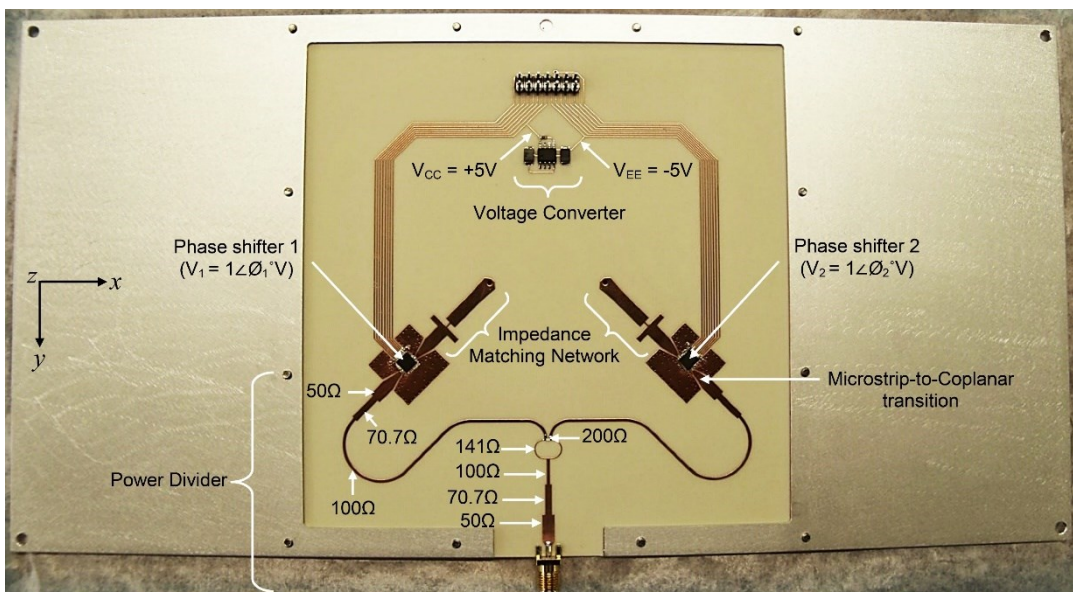


Figure 5.5: Bottom view of the fabricated back-to-back DRA array

Through a hybrid optimisation process, illustrated in Figure 5.6, $\angle V_2$ (the phase of excitation V_2) is determined as a function of the beam-pointing angle, θ_p . A secondary output of the first optimisation step is the geometrical parameters of the array such as the element spacing. The second optimisation step involves the optimisation of the dimensions of the impedance matching network. This hybrid optimisation algorithm is similar in approach to that used in (Lehmensiek & Khotso, 2014) where it was shown that when varying the amplitude or phase only, similar performance is achieved when compared to the case where both amplitude and phase are varied.

5.4.1 Optimisation of the Geometrical Parameters and Excitations

To simplify the design, the magnitude of the excitations $|V_1|$ and $|V_2|$ is kept constant, and since the array is symmetric, only $\angle V_2$ needs to be optimised as a function of the beam-pointing angle, θ_p . The beam-pointing angle is defined from the z-axis in the $E(xz)$ -plane of the array. The excitation phase $\angle V_2$ was determined by an exhaustive grid search in the range $\angle V_2 = [0^\circ, 360^\circ]$ using a grid of 37 equi-spaced points. The gain pattern, in the xz -plane, was calculated for each $\angle V_2$ using the MoM solver in FEKO. Subsequently, the maximum gain over pointing angle was determined in the range $\theta_p = [0^\circ, \theta_m]$ given any possible grid point phase excitation, where $\theta_m = 65.6^\circ$ (the maximum required pointing angle for a satellite at height 600 km). From these set of gain curves the envelope, i.e., maximum gain, over θ_p is determined.

The objective of the geometric parameters optimizing step is then to maximize the minimum of this gain envelope, G_{env} , curve weighted by the slant range path loss, L_0 . The resulting optimised excitation angles are given in Figure 5.7. Here the MoM results are validated with the FIT in CST MWS.

The Population-Based Incremental Learning (PBIL) algorithm (Baluja, 1994) combined with the Nelder-Mead algorithm (Nelder & Mead, 1965) constitutes the hybrid optimisation strategy implemented within MATLAB. The former is a global search algorithm with the latter being a downhill method. This hybridised implementation ensures for both high exploration and fast learning since the PBIL algorithm is a combination of genetic algorithms and competitive learning.

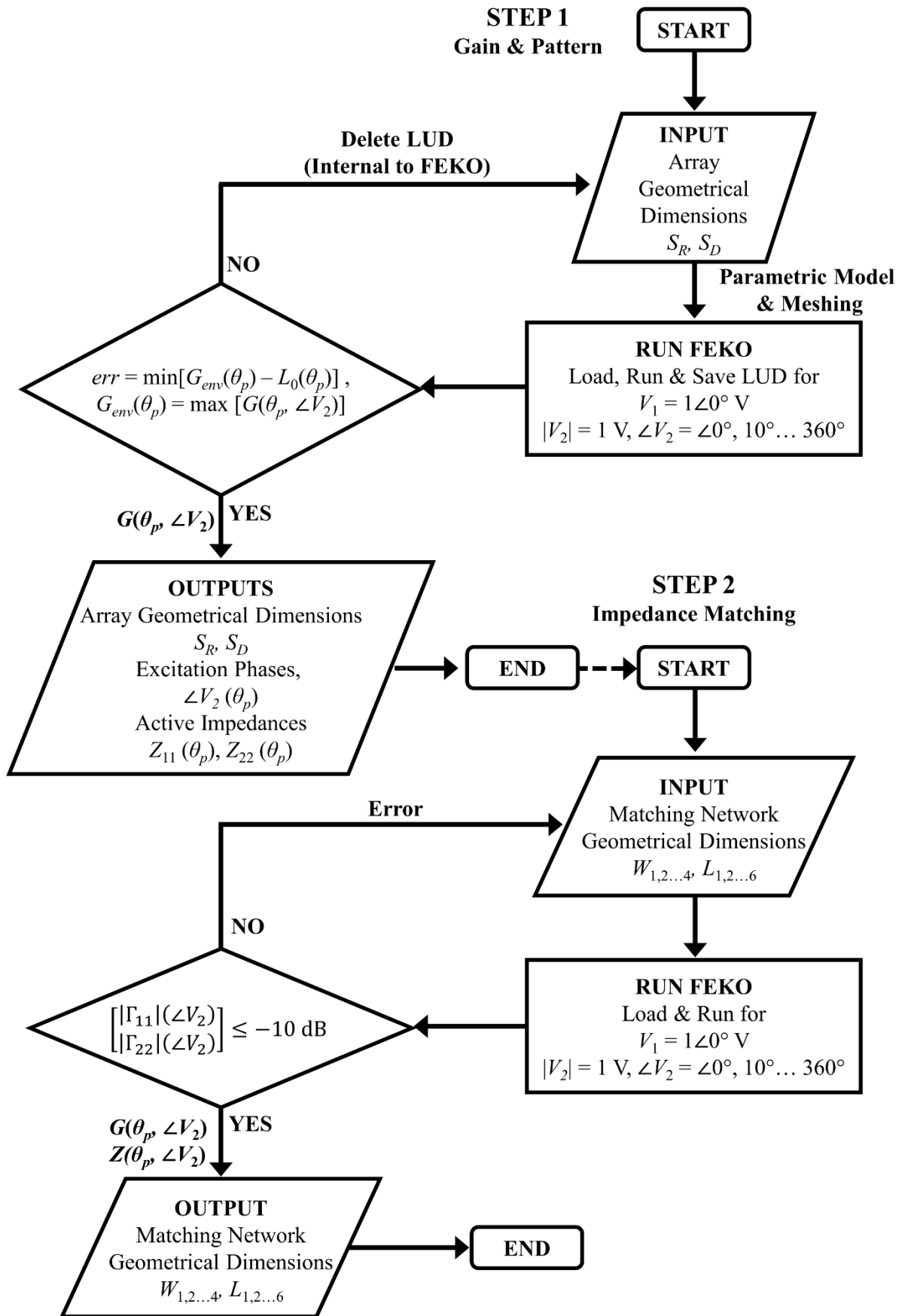


Figure 5.6: Optimisation algorithm for the back-to-back DRA array (Davids & Lehmensiek, 2019)

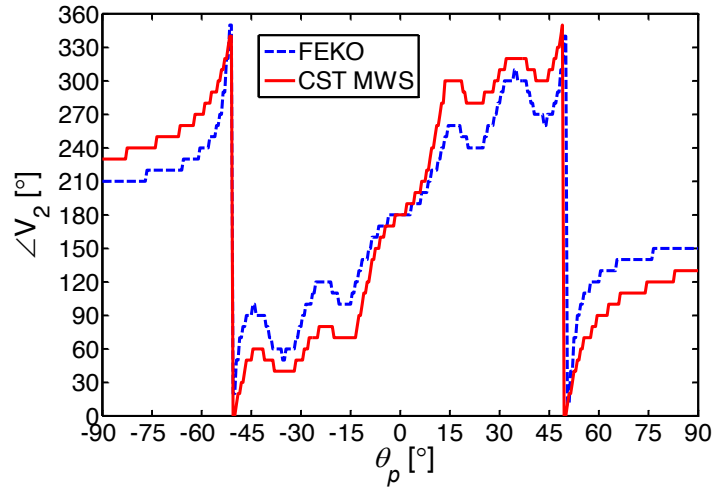


Figure 5.7: Simulated excitation phase angles of the back-back Yagi-Uda DRA array over all pointing angles

Due to the size of the EM problem and to reduce the computation time, the LU-decomposition matrix of the system of linear equations, associated with the MoM, is saved (in FEKO¹²). For this step the geometry of the model remains unchanged with the LU-decomposition matrix reused for each $\angle V_2$ excitation sweep. Table 5.2 gives then the optimised dimensions of the array for the geometrical parameters defined in Figure 5.4.

Table 5.2: Geometrical dimensions of the DRA Yagi-Uda array

Parameter	Dimensions	
	[mm]	$[\lambda_0]$
λ_0	53.76	1
S_R	11.32	0.211
S_D	8.86	0.165

Figure 5.8 and Figure 5.9 shows the simulated, FEKO and CST MWS far-field patterns over the beam-pointing angle for various excitation phase angles, $\angle V_2$, respectively. For pointing angles toward end-fire the gain increases to a maximum, near horizon ($\theta_{gs} = 5^\circ$), of 11.4 dBi and 10.2 dBi for FEKO and CST MWS respectively. As can be seen in Figure 5.8 and Figure 5.9, the far-field patterns are symmetric around the excitation phase angle, $\angle V_2 = 180^\circ$ (see Figure 5.7). From these set of gain curves the envelope, i.e., maximum gain, over θ_p is used to compare with the required gain pattern for a CubeSat in LEO. Furthermore, the dashed lines in Figure 5.8 and Figure 5.9 show the isoflux pattern formed by the envelope of the peak gains of the steered beams. The design approach presented here thus only require one phase shifter to point to all possible scan angles. This further reduces a small satellite's power budget while increasing its communication capabilities.

¹² FEKO allows for the saving of the MoM solution coefficients for large models where a particular problem, requiring multiple different excitations, is solved repeatedly.

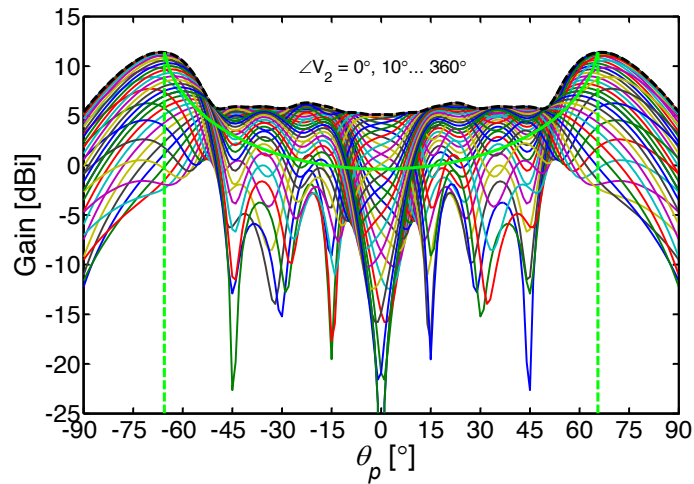


Figure 5.8: FEKO simulated $E_{(xz)}$ -plane of the back-to-back Yagi-Uda DRA array for different excitation angles, ΔV_2

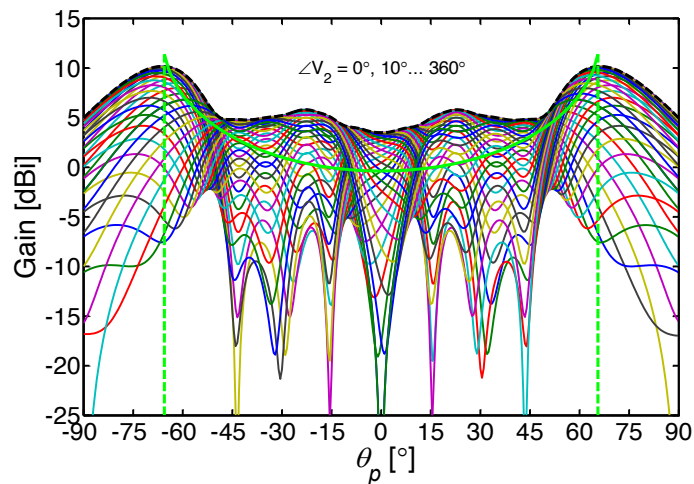


Figure 5.9: CST MWS simulated $E_{(xz)}$ -plane of the back-to-back Yagi-Uda DRA array for different excitation angles, ΔV_2

5.4.2 Design and Optimisation of the Impedance Matching Network

The matching network connects each feed-probe to a 6-bit digital phase shifter (MACOM MAPS-011008) via a simple L-section matching. The L-section matching network topology is shown in Figure 5.10 and uses two reactive elements consisting of a series inductor and shunt capacitor. To exploit symmetry in the electro-magnetic computations the shunt capacitor was divided in two, each with half the reactance of the equivalent single shunt capacitor. Figure 5.10 also shows the transition from lumped elements to the microstrip implementation of the matching network. Once the microstrip implementation of the matching network was derived, the network had to be optimised to accommodate the antenna impedance over all the phase states of the array.

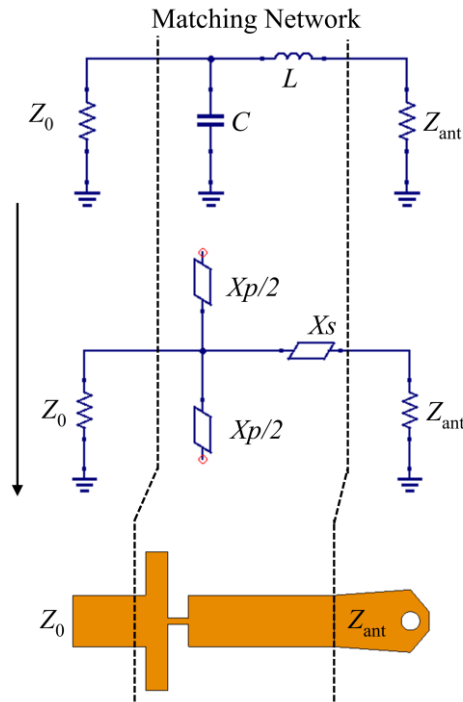


Figure 5.10: Matching network topology

The second optimisation step utilises the active impedance (also called the scan impedance), obtained from the first optimisation step (discussed in the previous section) to optimise the matching network. Again, a hybrid optimisation algorithm was used to determine the impedances (widths) and lengths of the transmission-line sections. This consisted of a combination of a global search algorithm, PBIL, and a reinforcement learning algorithm, the Broyden-Fletcher-Goldfarb-Shanno (BFGS) as implemented in Lehmensiek and Khotso (2014). Table 5.3 gives the optimised parameters of the matching network.

Table 5.3: Geometrical dimensions of the optimised impedance matching network

Geometrical configuration	Parameter	Dimensions		
		[mm]	$[\lambda_0]$	
	λ_g	28.35	1	
	W_{50}	3.56	0.126	
	W_1	1.28	0.045	
	W_2	4.34	0.153	
	W_3	0.41	0.015	
	W_4	1.54	0.054	
	L_1	1.28	0.045	
	L_2	5.25	0.185	
	L_3	10	0.353	
	L_4	1.42	0.050	
	L_5	9.59	0.338	
	L_6	5	0.176	
		Microstrip-to-CPW transition		
		Phase shifter		

The expected impedance (at the 50Ω transmission line end) for the unmatched and matched array is shown in Figure 5.11. It is apparent that the driven element is not well matched over all the excitation phases. By incorporating the optimised matching network between the phase shifter and the microstrip-to-coaxial feed a better impedance match for all excitation phases can be achieved.

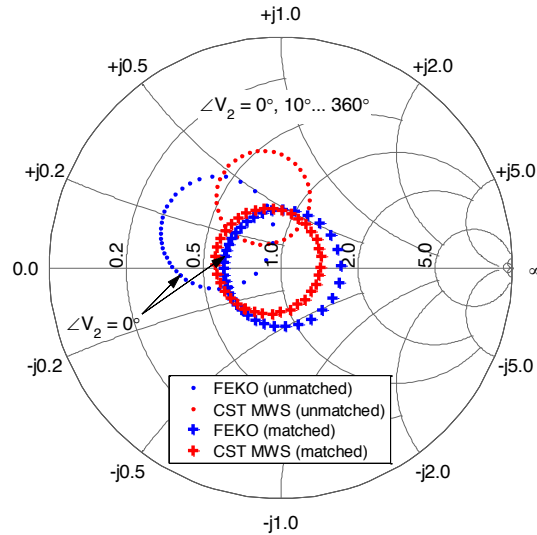


Figure 5.11: Input impedance over all excitation angles of the unmatched and matched Yagi-Uda DRA array at 5.6 GHz

The expected gain loss due to the mismatch is shown Figure 5.12. For the matched case the mismatch loss is less severe, as compared to the unmatched case, and more uniform over the range of excitation phase angles.

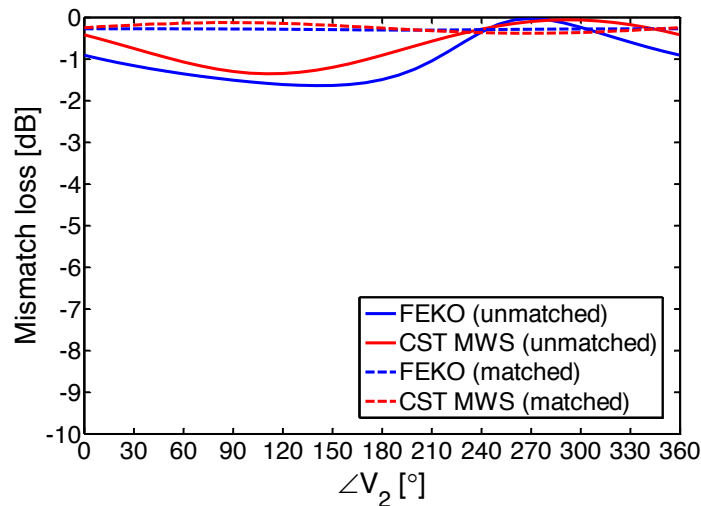


Figure 5.12: Predicted mismatch loss over all excitation angles of the unmatched and matched Yagi-Uda DRA array at 5.6 GHz

The differences between the CST MWS and FEKO results are due to the two different numerical methods and mesh types used, their quality and their efficacy in modelling the critical sections such as the impedance matching network and microstrip to coax transitions.

A volume mesh was used in CST MWS and a surface mesh in FEKO. In this dissertation numerous convergence tests were performed for the CST MWS model using both the time domain and frequency solver in combination with different mesh types. The most efficient and accurate result was obtained using the frequency solver with a tetrahedral mesh. Since the complete simulation of the array involves 37 runs to calculate all the far-field patterns, a compromise was made between the quality of the mesh, simulation speed and accuracy.

The layout of the beamforming is such that the matching network connects to the output port of the 6-bit phase shifter through a microstrip-to-coplanar transition. An identical microstrip-to-coplanar transition connects the input port of the phase shifter to a 50Ω transmission line. Both phase shifters are then connected to an equal-split Wilkinson power divider. The input port of the power divider terminates into an edge-launch SMA connector. This constitutes the array's implemented feeding network and is shown in Figure 5.5.

5.4.3 Mutual Coupling

The scanning performance for DRA arrays can vary depending on the operating mode and whether the elements are coupled in the H-plane or E-plane. The proposed DRA array has its elements coupled in the E-plane (see Figure 5.3). Alternatively, the elements could have also been configured in the H-plane. The coupling and radiation characteristics for the H-plane array are different from that of the E-plane array. In this dissertation the element, spacing, excitation current and phase is not identical, as would be the case for a conventional linear array. This is key to achieving a measured maximum beam-pointing angle of 66° .

The results of a numerical study of the mutual coupling for both an E-plane and H-plane 2×1 array configuration is shown Figure 5.13. It is observed that the mutual coupling for H-plane arrays decreases more rapidly than E-plane arrays with an increase in element spacing. For the E-plane array the coupling level decrease by approximately $1/d$ while that of the H-plane decrease by $1/d^2$. This result is very similar to the coupling characteristics of cylindrical DRAs (Chair et al., 2005). The active impedance of arrays coupled in the E-plane and H-plane vary greatly for different element spacing due to the confined nature of the mode inside the DRA (Guo et al., 1999).

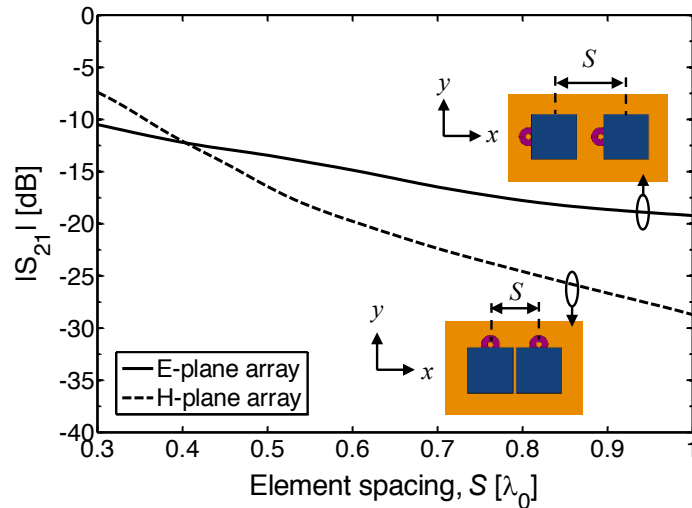


Figure 5.13: Mutual coupling between E-plane and H-plane rectangular DRA elements

The array configuration shown in Figure 5.3, with its optimised geometrical parameters, was used to investigate its radiation performance limits when fed in the E-plane and the H-plane. The FEKO result for the E-plane array was shown in Figure 5.8. The H-plane array result is shown in Figure 5.14. In Figure 5.14 the matching network was not included. For the H-plane array a decrease in gain was observed for beam-pointing angles toward the end-fire direction resulting in an array which fails to satisfy the required gain profile. The scanning limits for the H-plane DRA array is significantly less than the E-plane array which can be attributed to the internal field configuration of the driven elements and the stronger coupling between elements for element spacing below $0.4\lambda_0$. These results correlate with those obtained by Nikkhah (2013) where the element spacing was $0.2\lambda_0$.

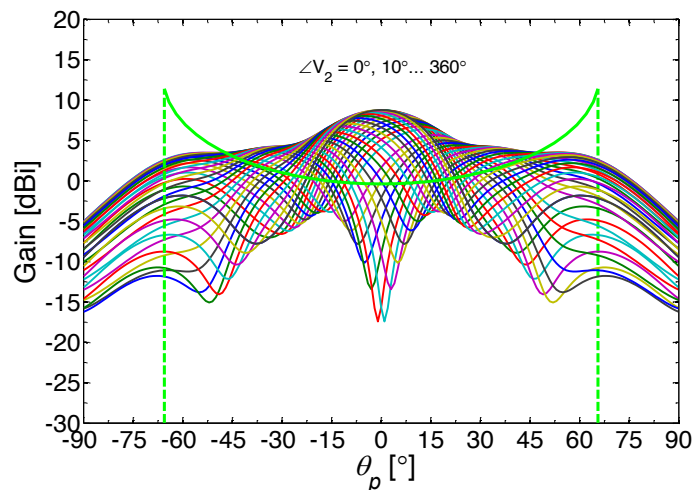


Figure 5.14: FEKO simulated E(xz)-plane of the H-plane configured back-to-back Yagi-Uda DRA array for different excitation angles, $\angle V_2$

5.4.4 Finite ground effects

CubeSats are standardised in dimensions of “U” measuring 10 cm x 10 cm x 10 cm. Since the ISPA is intended to be mounted on a CubeSat (with the most common sizes being 1U to 12U), the effect of the ground plane size on the radiation performance of the array was performed. Figure 5.15 shows the predicted radiation patterns for the excitation angle $\angle V_1 = \angle V_2 = 0^\circ$ for the various ground plane sizes. Since the EM problem is symmetric, only the positive theta angles are shown and discussed further.

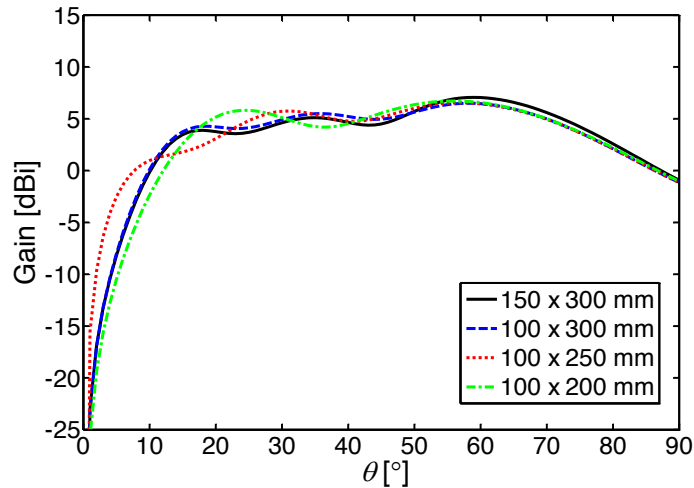


Figure 5.15: Simulated E(xz)-plane for the back-to-back Yagi-Uda DRA array on top of different ground plane sizes

The maximum pointing angle is preferred and therefore a ground plane size of 150 mm x 300 mm was chosen. It should be noted that the same scan angle can be achieved with the 100 mm x 300 mm ground plane but with 0.5 dB lower gain. The ripple present in the gain pattern is due to edge diffraction effects of the finite ground plane. This study made use of an infinitely thin PEC ground plane within FEKO.

5.4.5 Beam-Steering and Control

As mentioned earlier, beam-steering is accomplished through a beam-steering network consisting of the impedance matching network, connected to two MACOM MAPS-011008 digital phase shifters and fed by a Wilkinson power divider. The phase shifters are controlled by an Arduino UNO rev3 which is based on an ATmega328P with 14 digital Input/Outputs (Figure A.1). Two of these pins are designated for serial communication and are not used. The remaining 12 digital Input/Output pins are split equally between two port registers, PORTB (pins 8, 9, 10, 11, 12, 13) and PORTD (pins 2, 3, 4, 5, 6, 7). Two control registers, DDRB and DDRD, control whether the port registers function as inputs or outputs. Phase commands can be sent from a computer running MATLAB or using the built-in serial monitor within the Arduino Integrated Development Environment (IDE) version 1.6.3.

An Arduino sketch was written providing each phase shifter with the correct 6-bit sequence as per the datasheet truth table and is given in Appendix A. Inputting a value 0 to +63 in the serial monitor address phase shifter A and in turn steers the beam between $\theta_p = -90^\circ$ to $+90^\circ$. By inputting a value 0 to -63 in the serial monitor, phase shifter B is addressed and steers the beam between $\theta_p = +90^\circ$ to -90° . The input values translate to an excitation phase, $\angle V_2 = 0^\circ$ to 360° with a 5.6° step size (6-bit resolution of the digital phase shifter).

5.5 DRA Array Measured Results

The radiation performance of the back-to-back Yagi-Uda DRA array was measured inside an anechoic chamber at the University of Stellenbosch with the setup shown in Figure 5.16. The setup consists of the control computer running MATLAB R2013a which is connected to an Arduino Uno responsible for setting the excitation phase on either phase shifter A or B. Once the phase instruction was set an elevation cut is then measured. This corresponds to 64 individual E-plane cuts due to the 5.625° phase resolution of the 6-bit phase shifters. Two sets of 64 individual E-plane cuts were measured corresponding to the steered beams of each phase shifter. For clarity only results of phase shifter A is further discussed, due to the symmetry in the design.

An Agilent N5242A was used to measure the patterns and gain over a frequency range 4 GHz to 8 GHz. The three-antenna method (Balanis, 2005:1031) was used to measure the gain of the array. The three antennas are the; AUT (antenna A), NSI-RF-RGP-10 (antenna B) and Standard gain horn (antenna C). The corresponding distances are $D_{AB} = 1$ m, $D_{AC} = 1.3$ m and $D_{BC} = 1.1$ m which satisfy the far-field condition.

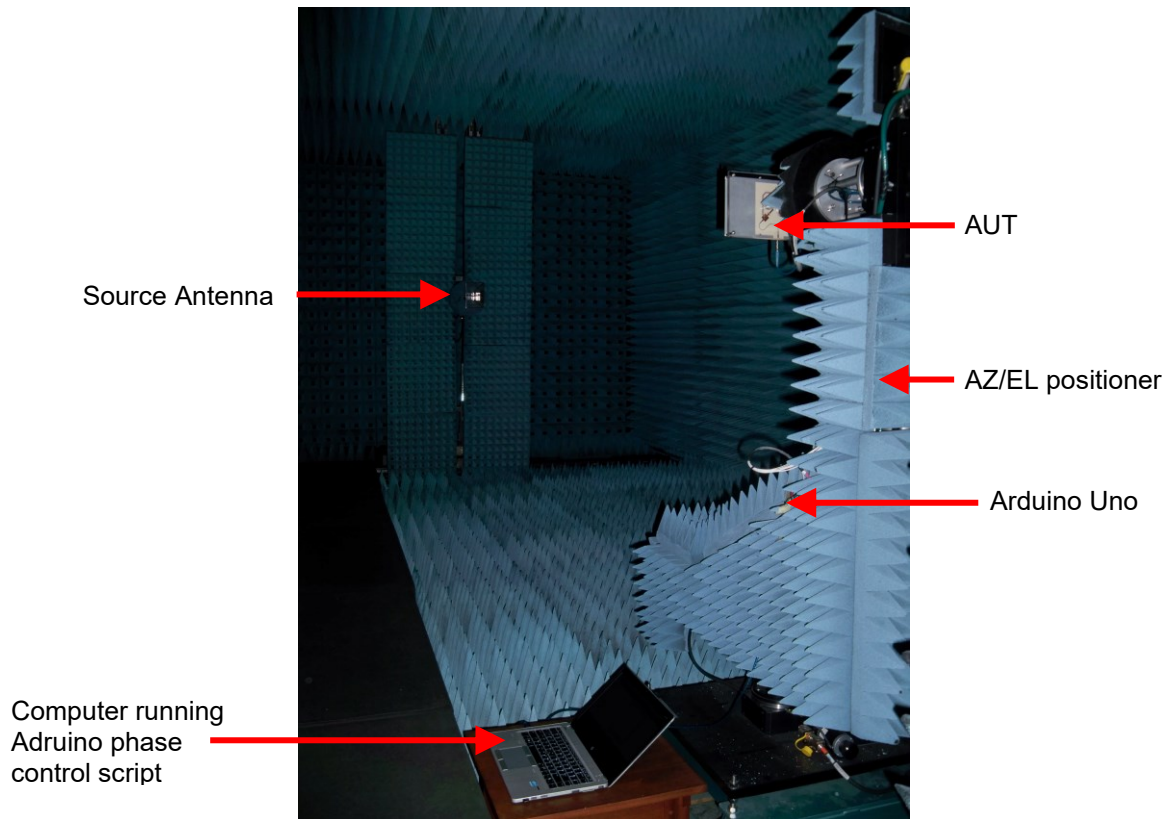


Figure 5.16: Measurement setup of the back-to-back Yagi-Uda DRA array in the rectangular anechoic chamber at the Stellenbosch University

The measured input reflection coefficient of the back-to-back Yagi-Uda DRA array is shown in Figure 5.17 over the excitation angles. A good impedance match is observed between 5.74 GHz and 6 GHz.

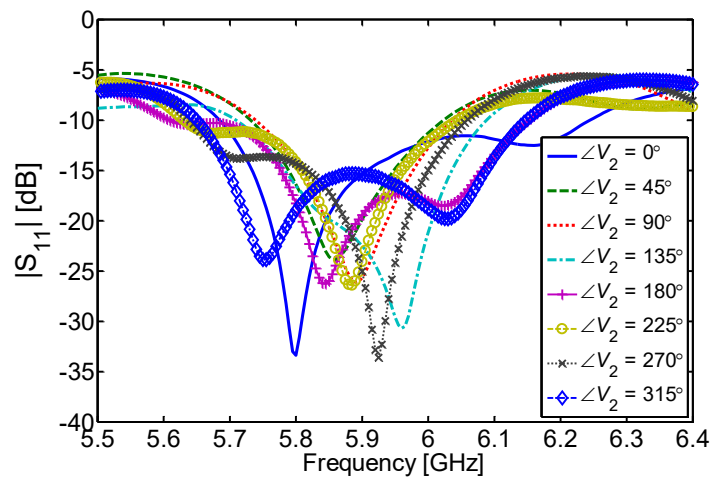


Figure 5.17: Measured input reflection coefficient of the back-to-back Yagi-Uda DRA array over the full range of excitation phase angles

The measured far-field patterns corresponding to the same excitation angles in Figure 5.17 is shown in Figure 5.18.

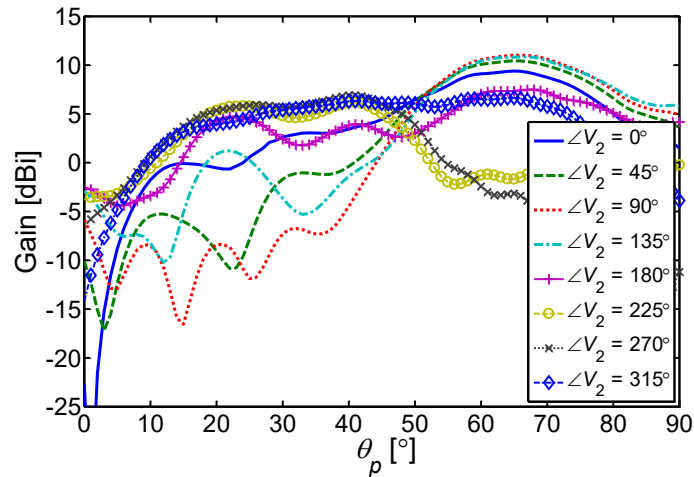


Figure 5.18: Measured gain in the $E(xz)$ -plane of the back-to-back Yagi-Uda DRA array over the full range of excitation phase angles

A complete summary of the array's scanning performance and achieved gain is given in Table 5.4. In Table 5.4 the beam-pointing angles, $\theta_p = [0^\circ, 22^\circ, 44^\circ, 66^\circ]$ are given with the required excitation phases. Also given is the achieved and required gain for the above-mentioned pointing angles.

Table 5.4: Summary of the scanning performance of the back-to-back Yagi-Uda DRA array

Beam-pointing angle, θ_p ($^\circ$)	Excitation phase, $\angle V_2$ ($^\circ$)			Gain, G (dBi)			
	FEKO	CST MWS	Measured	FEKO	CST MWS	Measured	Required
0	180	180	157.5	5.12	3.50	-2.24	0
22	240	280	247.5	6.30	5.78	5.82	0.60
44	260	300	292.5	5.91	4.81	6.61	2.53
66	140	100	106.9	11.4	10.2	11.4	6.34

Figure 5.19 then compares the gain envelope, G_{env} , for the simulated and measured gain patterns. Also shown in Figure 5.19 are the corresponding gain patterns for the beam-pointing angles shown in Table 5.4. A maximum gain of 11.4 dBi at a beam-pointing angle of $\theta_p = +66^\circ$ for an excitation phase $\angle V_2 = 106.9^\circ$ was measured. The simulated maximum gains are 11.4 dBi and 10.2 dBi for the excitation angles $\angle V_2 = 140^\circ$ and $\angle V_2 = 100^\circ$ in FEKO and CST MWS respectively. The simulated minimum gain, at zenith ($\theta_p = 0^\circ$), for a nadir pointing satellite is 5.12 dBi and 3.5 dBi for FEKO and CST MWS respectively and -2.24 dBi for the measured gain. Also shown in Figure 5.19 is the minimum required gain, normalized to zenith pointing, for a satellite in a 600 km orbit.

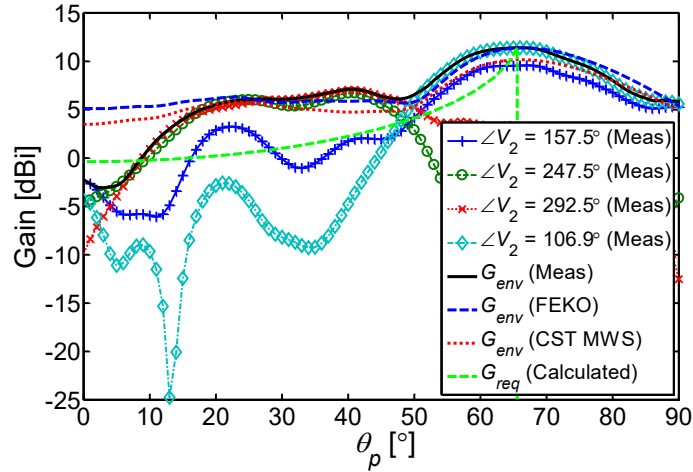


Figure 5.19: Maximum achievable gain, G_{env} , of the back-to-back Yagi-Uda DRA and required gain, G_{req} . Also shown are the measured gain patterns for the excitation angles $\angle V_2 = [157.5^\circ, 247.5^\circ, 292.5^\circ, 106.9^\circ]$ corresponding to the beam-pointing angles $\theta_p = [0^\circ, 22^\circ, 44^\circ, 66^\circ]$

The differences between the simulated and measured results in Figure 5.19 can be attributed to a combination of factors. These are, the individual amplitude and phase variations of the phase shifters and feeding network, the implementation tolerances, i.e. the ability to mount the DRA elements with their exact element spacing and not being able to guarantee their position once the array is mounted on the antenna test fixture inside the anechoic chamber. At this stage of the prototype all the DRA elements were held in position using masking tape only. Furthermore, the reduced gain at zenith is believed to be mainly attributed to the shift in the resonant frequency caused by the air gap between the DRA elements and ground plane. These dimensional tolerances can affect the far-field gain since this directly influences the coupling, active impedance and field configuration (or the mode) of the passive elements in the array.

5.6 Conclusion

In this chapter a beam steerable back-to-back Yagi-Uda DRA array was designed and implemented. The array uses mutual coupling to achieve a maximum gain of 11.4 dBi at a maximum scan angle of $\pm 66^\circ$. Increased scan angles can possibly be achieved by using additional directors or a combination of phase and amplitude excitation as shown by Lehmensiek and Khotso (2014). The gain is optimised to give an isoflux radiation pattern which results in an increase in communication time between a ground station and a spacecraft in LEO. Moreover, the approach presented here only needs one phase shifter to point to all scan angles since the patterns are symmetric around the excitation phase angle, $\angle V_2 = 180^\circ$ (see Figure 5.7). For larger CubeSats (3U and up), this ISPA implementation is most practical whilst maximizing the power capabilities of the satellite.

Chapter 6 Conclusions and Recommendations

This dissertation presents an investigative design approach for a Yagi-Uda back-to-back DRA array. This array is proposed for integration with a solar panel with the aim to conceptualise an integrated solar panel for CubeSats. The proposition is novel since transparent DRA elements are used instead of commonly used slot and microstrip patch radiators (transparent or meshed) reported in literature. The LASF35 optical glass is used due to its favourable dielectric and transmission properties.

First an overview is given on ISPAs, transparent antennas, DRAs and finally transparent DRAs. The overview systematically points out the rationale behind the ISPA approach presented here. Initially, the theory of the rectangular DRA is presented which entails using the DWM as a baseline to calculate the resonant frequency and radiation Q-factor of the fundamental TE mode. The model does not take in effect the feeding mechanism or refraction from a finite ground plane and hence the DWM results are validated with experimental results in the form of both numerical techniques and measurements. CMA was used here as a complimentary numerical technique since it gives physical insight into the resonant modes and their radiation behaviour of rectangular DRAs.

A single transparent DRA was mounted on top of a triple-junction solar cell and studied numerically and experimentally. Simulations predicted that coupling to the metallic contacts in the solar cell may cause resonances which could interfere with the DRA's operation. These unwanted resonances were not observed experimentally. In the absence of a professional solar simulator, the effect of the DRA on the solar cell was measured and showed a difference in solar efficiency of 4% between the case of a bare solar cell and the case with the solar cell with DRA placed on top. In this work it is seen that a solar cell placed between a DRA and a ground plane still operates without significant degradation in either the solar cell or the DRA's performance.

Lately much attention has been given to Electronically Steerable Parasitic Array Radiator (ESPAR) arrays implemented with DRA elements (Nikkhah et al., 2014). These arrays are characterized by low complexity since steering is accomplished without any phase shifters. A phase shift is realized though capacitive loading using varactor diodes. Furthermore, the ESPARs reported in literature achieved beam-steering limits of $\pm 30^\circ$ and $\pm 60^\circ$ when coupled

in the H-plane and E-plane, respectively. In this work, a beam-steering limit of $\pm 66^\circ$ was achieved by designing a Yagi-Uda DRA array with elements configured in the E-plane. These limits can be increased further through using more directors in the Yagi-Uda array. A satellite mounted antenna that can optimise its gain pattern as the orbital properties of the satellite change during an over-pass is highly favoured to maximise the contact time between the satellite and ground station. The gain envelope of all beam-steering angles was optimised for constant flux density at a satellite ground station thus maximizing the contact time between a satellite in LEO and a ground station.

6.1 Responses to Research Questions

- ***Is it feasible to integrate a transparent DRA with a solar panel of a CubeSat to obtain a low-profile, lightweight, moderate gain antenna?*** – This work clearly illustrates that an integrated solar panel antenna with >5 dBi (single element) or >11 dBi (for the array) is feasible. Furthermore, the antenna is of low profile which satisfies the height limitations of the CubeSat standard. The mass of a single DRA element is 2.5 g resulting in a mass of 12,5 g in total for the elements of the array. Weight can further be reduced by implementing the array directly on the CubeSat face with the only other weight contribution coming from the feeding network PCB.
- ***What transparent dielectric material is most suitable as the DRA element?*** – Here three different dielectric glass materials were considered for solar cell integration. These materials were Borosilicate K9 (Pyrex), Sapphire and LASF35 glass. It was shown that LASF35 is preferred over lower dielectric constant glass types in order to meet the size and height requirements for CubeSats. This is due to its high dielectric constant and inherent mechanical strength of LASF35.
- ***What effect does the solar panel have on the performance of the antenna?*** – Through a numerical study little degradation in the antenna performance was observed. The most critical parameter responsible for the biggest influence on the antenna's performance is the height of the DRA above a ground plane when placed on top of a solar cell. This is due to the strong dependence on the ground plane to support the internal field configuration of the fundamental magnetic dipole mode of a rectangular DRA.
- ***What effect does the antenna have on the solar panel?*** – Careful consideration was given to the choice of dielectric material to not degrade the electrical performance of the solar panel. A reduced solar cell efficiency of 4% was measured which makes the proposed LASF35 glass suitable for solar panel integration. Pyrex and Sapphire can also be used which would lead to a more optically efficient antenna at the cost of increased size.

6.2 Recommendations

Although the proof of concept was successful the solar cell efficiency tests should ideally be validated using a professional solar simulator. The use of an adhesive similar to those used for bonding solar cell coverglass should be used to ensure the DRA position and to eliminate any air gaps.

An alternative configuration for the array presented could be to feed the centre DRA element (reflector in the array presented here) then controlling the coupled currents on the parasitic elements using reactive loading. The scanning limits of such an array is yet to be investigated.

Lastly, it is worthwhile to construct a circular polarized antenna since this can be relatively easily implemented and is favoured in space communications. This was also the primary reason for choosing a square shaped DRA since dual modes for circular polarization can be easily excited.

6.3 Future Work

Expansions on this work could include implementing this concept at higher frequency bands. Although the proof of concept here is implemented at C-Band, the concept can easily be scaled to X- or Ka-band since this would produce an even more compact antenna. As mentioned above, circular polarized designs are possible by using inclined metallic strips or the use of dual orthogonal feeds. The transparent metallic material identified for future work on this topic is monolayer Graphene identified for its excellent translucency and electrical properties.

Due to the miniaturisation trend of spacecraft, multi-purpose antennas and sensors will be of importance for future space missions. At the time of this dissertation several advanced CubeSat antennas have been conceptualised and demonstrated for deep space missions (Chahat et al., 2019). These missions require high gain antennas with many implementations being reflectarrays integrated with deployable solar panels. The concept presented in this dissertation can also be extended to reflectarrays. Reflectarrays typically make use of patch radiators which limit the bandwidth of the array and by using DRA elements the bandwidth can be increased.

New dielectric glass materials are constantly being developed and these new materials with the advancements in additive manufacturing hold exciting possibilities as extensions to the concept proposed here.

Bibliography

Altair, FEKO, Suite 7.0.2, Stellenbosch, South Africa, [Online]. Available: <https://www.feko.info/>

Al-Zoubi, A.S. & Kishk, A.A. 2009. Wide Band Strip-Fed Rectangular Dielectric Resonator Antenna. *Proceedings of the 2009 IEEE Conference on Antennas and Propagation*, Berlin, Germany, 23–27 March 2009. The institute: 2379–2382.

AZUR SPACE Solar Power GmbH, *28% Triple Junction GaAs Solar Cell, Type: TJ Solar Cell 3G28C*, 2013. [Online]. Available: http://www.azurspace.com/images/pdfs/HNR_0002490-00-03.pdf

Balanis, C.A. 1989. *Advanced Engineering Electromagnetics*. 1st ed. New York: John Wiley & Sons, Inc.

Balanis, C.A. 2005. *Antenna Theory: Analysis and Design*. 3rd ed. Hoboken, New Jersey: John Wiley & Sons, Inc.

Baluja, S. 1994. *Population-Based Incremental Learning: A Method for Integrating Genetic Search Based Function Optimization and Competitive Learning*. Carnegie Mellon University, Technical Report CMU-CS-94-163.

Baquedano, E., Torné, L., Caño, P., & Postigo, P.A. 2017. Increased Efficiency of Solar Cells Protected by Hydrophobic and Hydrophilic Anti-Reflecting Nanostructured Glasses. *Nanomaterials*, 7(12): 437.

Bendel, C., Kirchhof, J. & Henze, N. 2003. Application of photovoltaic solar cells in planar antenna structures. *Proceedings of 3rd World Conference on Photovoltaic Energy Conversion*, Osaka, Japan, 11-18 May. The institute: 220–223.

Bernabeu-Jiménez, T., Valero-Nogueira, A., Vico-Bondia, F., Antonino-Daviu, E. & Cabedo-Fabres, M. 2014. A 60-GHz LTCC Rectangular Dielectric Resonator Antenna design with Characteristic Mode Theory. *Proceedings of the 2014 IEEE Antennas and Propagation Society International Symposium (APSURSI)*, Memphis, USA, 6–11 July. The institute: 1928–1929.

Burnett, B. 2000. *The Basic Physics and Design of III-V Multijunction Solar Cells*. National Renewable Energy Laboratory, Golden, Co. Available at <http://educypedia.karadimov.info/library/NREL.pdf> [20 July 2011].

Cabedo-Fabrés, M., Antonino-Daviu, E., Valero-Nogueira, A. & Ferrando Bataller, M. 2007. The Theory of Characteristic Modes Revisited: A Contribution to the Design of Antennas for Modern Applications. *IEEE Transactions on Antennas and Propagation*, 49(5): 52–68.

California State Polytechnic University. 2014. *CubeSat Design Specification, Revision 13*. Available at https://static1.squarespace.com/static/5418c831e4b0fa4ecac1bacd/t/56e9b62337013b6c063a655a/1458157095454/cds_rev13_final2.pdf [Accessed 21 October 2015].

- Chahat, N., Decrossas, E., Gonzalez-Ovejero, D., Yurduseven, O., Radway, M.J., Hodges, R.E., Estabrook, P., Baker, J.D., Bell, D.J., Cwik, T.A. & Chattopadhyay, G. 2019. Advanced CubeSat Antennas for Deep Space and Earth Science Missions: A review. *IEEE Antennas and Propagation Magazine*, 61(5): 37-46.
- Chair, R., Kishk, A. & Lee, K. 2005. Comparative Study on the Mutual Coupling Between Different Sized Cylindrical Dielectric Resonators Antennas and Circular Microstrip Patch Antennas. *IEEE Transactions on Antennas and Propagation*, 53(3): 1011–1019.
- Chaudhary, R.K., Mishra, V.V., Srivastava, K.V. & Biswas, A. 2010. Multi-layer Multi-permittivity Dielectric Resonator: A New Approach for Improved Spurious free window. *Proceedings of the 40th European Microwave Conference*, Paris, France, 28–30 September. The institute: 1194–1197.
- Choi, E.C., Lee J.W. & Lee, T.K. 2013. Modified S-band satellite antenna with isoflux pattern and circularly polarized wide beamwidth. *IEEE Antennas Wireless Propagation Letters* 12:1319–1322.
- Coulibaly, Y., Denidni, T.A. & Boutayeb, H. 2008. Broadband Microstrip-Fed Dielectric Resonator Antenna for X-Band Applications. *IEEE Antennas and Wireless Propagation Letters*, 7:341–345, 21 March.
- CST Microwave Studio, Bad Nauheimer Str. 19, D-64289 Darmstadt, [Online]. Available: <http://www.cst.com>.
- Davids, V. & Lehmsiek, R. 2014. The effects of a triple-junction solar cell on a dielectric resonator antenna. Proceedings of the 8th European Conference on Antennas and Propagation (EuCAP), The Hague, Netherlands, 6–11 April 2014, The institute: 2928–2931.
- Davids, V. & Lehmsiek, R. 2016. A beam steerable back-to-back Yagi-Uda dielectric resonator antenna array. Proceedings of the 10th European Conference on Antennas and Propagation (EuCAP), Davos, Switzerland, 10–15 April 2016, The institute: 1–4.
- Davids, V.P. & Lehmsiek, R. 2019. A steerable dielectric resonator antenna array with isoflux radiation pattern. *Microwave and Optical Technology Letters*, 61(10): 1–8.
- De Young, C.S. & Long, S.A. 2006. Wideband Cylindrical and Rectangular Dielectric Resonator Antennas. *IEEE Antennas and Wireless Propagation Letters*, 5:426–429.
- Fang, X.S. & Leung, K.W. 2014. Design of Wideband Omnidirectional Two-Layer Transparent Hemispherical Dielectric Resonator Antenna. *IEEE Transactions on Antennas and Propagation*, 62(10):5353–5357.
- Fawole, O.C. 2012. *A Multifunctional Solar Panel Antenna for Cube Satellites*. Unpublished MSc dissertation, Utah State University, Logan, Utah.
- Gao, S., Clark, K., Unwin, M., Zackrisson, J., Shiroma, W.A., Akagi, J.M., Maynard, K., Garner, P., Boccia, L., Amendola, G., Massa, G., Underwood, C., Brenchley, M., Pointer, M. & Sweeting, M.N. 2009. Antennas for Modern Small Satellites. *IEEE Antennas and Propagation Magazine*, 51(4):40–56.
- Gao, S., Rahmat-Samii, Y., Hodges, R.E. & Yang, X.X. 2018. Advanced antennas for small satellites. *Proceedings of the IEEE*, 106(3):391–403.
- Garbacz, R.J. 1965. Modal Expansions for Resonance Scattering Phenomena. *Proceedings of the IEEE*, 53(8):856–864.

- Gastine, M., Courtois, L. & Dormann, J.L. 1967. Electromagnetic Resonances of Free Dielectric Spheres. *IEEE Transactions on Microwave Theory and Techniques*, 15(6):694–700.
- Gray, D., Lu, J. W.D. & Thiel, C. 1998. Electronically steered Yagi-Uda microstrip patch antenna array. *IEEE Transactions on Antennas and Propagation*, 46(5):605–608.
- Guan, N., Furuya, H., Himeno, K., Goto, K. & Ito, K. 2007. A Monopole Antenna Made of a Transparent Conductive Film. *Proceedings of the IEEE Antenna Technology: Small and Smart Antennas Metamaterials and Applications*, Cambridge, UK, 21–23 March 2007. The institute:263–266.
- Guo, Y.X., Luk, K.M. & Leung, K.W. 1999. Mutual coupling between rectangular dielectric resonator antennas by FDTD. *IEEE Proceedings of the Microwaves, Antennas and Propagation*, 146(4): 292–294.
- Harrington, R. & Mautz, J. 1971. Theory of characteristic modes for conducting bodies, *IEEE Transactions on Antennas and Propagation*, 19(5):622–628.
- Hebib, S., Fonseca, N.J. & Aubert, H. 2011. Compact printed quadrifilar helical antenna with iso-flux-shaped pattern and high crosspolarization discrimination. *IEEE Antennas Wireless Propagation Letters* 10:635–638.
- Hesselbarth, J., Geier, D. & Diez, M.A.B. 2013. A Yagi-Uda antenna made of high-permittivity ceramic material, *Proceedings of the 2013 Loughborough Antennas and Propagation Conference (LAPC)*, Loughborough, United Kingdom, 11–12 November 2013. The institute: 94–98.
- Hodges, R.E., Chahat, N., Hoppe, D.J & Vacchione, J.D. 2017. A Deployable High-Gain Antenna Bound for Mars. *IEEE Antennas and Propagation Magazine*, 59(2):39–49.
- Huynh, A.P., Long, S.A. & Jackson, D.R. 2010. Effects of permittivity on bandwidth and radiation patterns of cylindrical dielectric resonator antennas. *Proceedings of the Antennas and Propagation Society International Symposium (APSURSI)*, Toronto, Canada, 11–17 July 2010. The institute: 1–4.
- ISIS. Antenna Systems. [Online]. <https://www.isispace.nl/wpcontent/uploads/2016/02/ISIS-Antenna-systems-Brochure-v1.pdf> [Accessed 12 May 2019].
- Issler, J-L., Gaboriaud, A., Apper, F., & Ressouche, A. 2014. CCSDS Communication Products in S and X band for CubeSats. *Proceedings of 28th AIAA/USU Conference on Small Satellites*, Utah, United States, 4–7 August. The institute: 1–7.
- Jones, R.K., Ermer, J.H., Fetzer, C.M & King, R.R. 2012. Evolution of Multijunction Solar Cell Technology for Concentrating Photovoltaics. *Japanese Journal of Applied Physics*, 51(10S): 1–4.
- Junker, G.P., Kishk, A.A., Glisson, A.W. & Kijfez, D. 1994. Effect of air gap on cylindrical dielectric resonator antenna operating in TM₀₁ mode, *IET Electronics Letters*, 30(2):97-98.
- Kajfez, D. & Kishk, A.A. 2002. Dielectric Resonator Antenna- Possible Candidate For Adaptive Antenna Arrays. Presentation at VITEL 2002, *International Symposium on Telecommunication, Next Generation Networks and Beyond*, Portoroz, Slovenia, 13–14 May 2002. Available at <http://www.ee.olemiss.edu/darko/dra-pcfaaa.pdf> [Accessed 12 August 2011].

- Khotso, P.A., Lehmensiek, R. & van Zyl, R.R. 2011. Comparison of the communication time of a high gain versus a low gain monopole-like low profile antenna on a 3-unit CubeSat, *Proceedings of the 2011 IEEE AFRICON*, Livingstone, Zambia, 13–15 September 2011. The institute: 1–4.
- Kishk, A.A. & Wei Huang. 2011. Size-Reduction Method for Dielectric-Resonator Antennas. *IEEE Antennas and Propagation Magazine*, 53(2):26–38.
- Kishk, A.A. 2002. Tetrahedron and triangular dielectric resonator antenna with wideband performance. *Proceedings of the IEEE Antennas and Propagation Society International Symposium*, Texas, USA, 16–21 June 2002. The institute: 462–465.
- Kishk, A.A. 2003. Dielectric resonator antenna, a candidate for radar applications, *Proceedings of the IEEE 2003 Radar Conference*, Alabama, USA, 5–8 May 2003. The institute: 258–264.
- Kishk, A.A. 2003. Directive dielectric resonator antenna excited by probe or narrow slot, *Proceedings of the 2003 IEEE Radio and Wireless Symposium (RWS)*, California, USA, 15–18 November 2003. The institute: 387–390.
- Kishk, A.A. 2005. Directive Yagi-Uda dielectric resonator antennas. *Microwave Optical Technology Letters*, 44(5):451–453.
- Lehmensiek, R. & Khotso, P. 2014. Steerable Back-to-Back Yagi-Uda Dipole Array. *Proceedings of the 2014 IEEE European Conference on Antennas and Propagation*, The Hague, Netherlands, 6–11 April. The institute: 1920–1923.
- Lehmensiek, R. 2012. Using the Physical Structure of a Passive Aerodynamic Attitude-Stabilization System as a Multi-Frequency Antenna on Nano-Satellites. *IEEE Antennas and Propagation Magazine*, 54(3):40–49.
- Leung, K.W., Lim, E.H. & Fang, X.S. 2012. Dielectric Resonator Antennas: From the Basic to the Aesthetic. *Proceedings of the IEEE*, 100(7):2181–2093.
- Leung, K.W., Pan, Y.M., Fang, X.S., Lim, E.H., Luk, K.M. & Chan, H.P. 2013. Dual-Function Radiating Glass for Antennas and Light Covers – Part I: Omnidirectional Glass Dielectric Resonator Antennas. *IEEE Transactions on Antennas and Propagation*, 61(2):578–586.
- Lim, E. H. & K. W. 2010. Transparent Dielectric Resonator Antennas for Optical Applications. *IEEE Transactions on Antennas and Propagation*, 58(4):1054–1059.
- Ludick, D.J, Lezar, E. & Jakobus, U. 2012. Characteristic mode analysis of arbitrary electromagnetic structures using FEKO. *International Conference on Electromagnetics in Advanced Applications*, Cape Town, South Africa, 2–7 September. The institute: 208–211.
- Luk, K.M. & Leung, K.W. (eds) 2003. *Dielectric Resonator Antennas*, Baldock, Hertfordshire, England: Research Studies Press Ltd.
- Mahmoud, M.N. 2010. *Integrated Solar Panel Antennas for Cube Satellites*. Unpublished MSc dissertation, Utah State University, Logan, Utah.
- Marcatili, E.A.J. 1969. Dielectric Rectangular Waveguide and Directional Coupler for Integrated Optics. *Bell Systems Technical Journal*, 48:2071–2102.

- Mehmood, A., Zheng, Y., Braun, H., Hovhannisyan, M., Letz, M. & Jakoby, R. 2014. Dual Band Dielectric Resonator Antenna for Hiperlan Based on Transparent Glass Material. *Proceeding of the 2014 German Microwave Conference (GeMIC)*, Aachen, Germany, 10–12 March. VDE:1–4.
- Mongia, R.K. & Bhartia, P. 1994. Dielectric resonator antennas – a review and general design relations for resonant frequency and bandwidth. *International Journal of Microwave and Millimeter-Wave Computer-Aided Engineering*, 4(3):230–247.
- Mongia, R.K. & Ittipiboon, A. 1997. Theoretical and experimental investigations on rectangular dielectric resonator antennas. *IEEE Transactions on Antennas and Propagation*, 45(9):1348–1356.
- Mongia, R.K., Larose, C.L., Mishra, S.R. & Bhartia, P. 1992. Measurement of RCS of cylindrical and rectangular dielectric resonators, *IET Electronics Letters*, 28(21):1953-1955.
- Nasimuddin & Esselle, K.P. 2007. A Low-Profile Compact Microwave Antenna with High Gain and Wide Bandwidth. *IEEE Transactions on Antennas and Propagation*, 55(6):1880–1883.
- Nelder, J.A. & Mead, R. 1965. A simplex method for function minimization. *Computer Journal*, 7:308–313.
- Nikkhah, M.R., Loghmannia, P., Rashed-Mohassel, J. & Kishk, A.A. 2014. Theory of ESPAR Design with Their Implementation in Large Arrays. *IEEE Transactions on Antennas and Propagation*, 62(6):3359–3364.
- Nikkhah, M.R., Rashed-Mohassel, J. & Kishk, A.A. 2013. Compact low-cost phased array of dielectric resonator antenna using parasitic elements and capacitor loading. *IEEE Transactions on Antennas and Propagation*, 61(4):2318–2321.
- Nikkhah, M.R., Rashed-Mohassel, J. & Kishk, A.A. 2013. High-gain aperture coupled rectangular dielectric resonator antenna array using parasitic elements. *IEEE Transactions on Antennas and Propagation*, 61(7):3905–3908.
- Okaya, A. & Barash, L.F. 1962. The Dielectric Resonator Antennas. *Proceedings of the IRE*, October. 50(10): 2081–2092.
- Petosa, A. & Ittipiboon, A. 2010. Dielectric Resonator Antennas: A Historical Review and the Current State of the Art. *IEEE Antennas and Propagation Magazine*, 52(5):91–116.
- Petosa, A. & Thirakoune, S. 2011. Rectangular Dielectric Resonator Antennas with Enhanced Gain. *IEEE Transactions on Antennas and Propagation*, 59(4):1385–1389.
- Petosa, A. 2007. *Dielectric Resonator Antenna Handbook*. Norwood, MA, Artech House.
- Petosa, A., Ittipiboon, A. & Cuhaci, M. 1999. Low Profile Dielectric Resonator Antenna Arrays for Reflector Feeds. *Proceedings of the 29th European Microwave Conference*, Munich, Germany, 5–7 October 1999. The institute: 171–174.
- Petosa, A., Ittipiboon, A., Antar, Y. & Roscoe, D. 1998. Recent Advances in Dielectric-Resonator Antenna Technology. *IEEE Antennas and Propagation Magazine*, 40(3):35–48.
- Rashidian, A. & Shafai, L. 2014. Wideband highly-efficient transparent/miniaturized antennas using clear colorless acrylic sheets for space/WLAN applications. *Proceedings of the IEEE International Symposium on Antenna Technology and Applied Electromagnetics*, Victoria British Columbia, Canada, 13–16 July 2014. The institute: 1–2.

- Ravanelli, R., Iannicelli, C., Baldecchi, N. & Franchini, F. 2010. Multi-objective optimization of an isoflux antenna for LEO satellite down-handling link. *In: Proceedings of the 18th International Conference on Microwave Radar and Wireless Communications (MIKON)*, 1–4.
- Richtmyer, R.D. 1939. Dielectric Resonators. *Journal of Applied Physics*, 10:391–398.
- Saberin, J.R. & Furse, C. 2010. Challenges with optically transparent patch antennas for small satellites. *IEEE Antennas and Propagation Society International Symposium (APSURSI)*, Toronto, ON, Canada, 11–17 July 2010. The institute:1–4.
- Schott, A.G., *New LASF35*, 2013. [Online]. Available: https://www.schott.com/d/advanced_optics/0ac4af68-8765-494c-86ad-d318bced6180/1.2/schott-lasf35-april-2015-eng.pdf
- Semouchkina, E., Semouchkin, G., Cao, W. & Mittra, R. 2002. FDTD analysis of modal characteristics of dielectric resonator antennas. *Proceedings of the IEEE Antennas and Propagation Society International Symposium*, Texas, USA, 16–21 June. The institute: 466–469.
- SiliconFarEast, *Properties of Si, Ge, and GaAs at 300K*, 2013. [Online]. Available: <http://www.siliconfareast.com/sigegaas.htm>
- Simeoni, M., Cicchetti, R., Yarovoy, A. & Caratelli, D. 2009. Supershaped dielectric resonator antennas. *Proceedings of the IEEE Antennas and Propagation Society International Symposium*, Charleston, SC, 1–5 June 2009. The institute: 1–4.
- Sun, Y., Fang, X.S. & Leung, K.W. 2015. Wideband Two-Layer Transparent Cylindrical Dielectric Resonator Antenna Used as a Light Cover. *Proceedings of the IEEE International Conference on Computational Electromagnetics*, Hong Kong, 2–5 February. The institute: 286–287.
- Tanaka, M., Suzuki, Y., Araki, K. & Suzuki, R. 1995. Microstrip antenna with solar cells for microsattellites, *IET Electronics Letters*, 31(1):5–6.
- Trueman, C.W. 1993. FDTD computation of the RCS of high permittivity cubes. *Proceedings of the 1993 IEEE Antennas and Propagation Society International Symposium*, Michigan, USA, 28 June–2 July 1993. The institute: 846–849.s
- Trueman, C.W., Mishra, S.R., Larose, C.L. & Mongia, R.K. 1994. Resonant frequencies and Q factors of dielectric parallelepipeds by measurement and by FDTD, *Proceedings of the 1994 IEEE Conference on Precision Electromagnetic Measurements*, Colorado, USA, 27 June–1 July 1994. The institute: 61–62.
- Trueman, C.W., Mishra, S.R., Larose, C.L. & Mongia, R.K. 1995. Resonant frequencies and Q factors of dielectric parallelepipeds. *IEEE Transactions on Instrumentation and Measurement*, 44(2):322–325.
- Uda, S. & Mushiake, Y. 1954. *Yagi-Uda antenna*, Sendai, Japan, Sasaki Printing and Publishing Company, Ltd.
- Vaccaro, S., Pereira, C., Mosig, J.R. & de Maagt, P. 2009. In-flight experiment for combined planar antennas and solar cells (SOLANT). *IET Microwaves, Antennas & Propagation*, 3(8): 1279–1287.
- Vaccaro, S., Torres, P., Mosig, J.R., Shah, A., Zurcher, J.F., Skrivervik, A.K., Gardiol, F., de Maagt, P. & Gerlach, L. 2000. Integrated Solar Panel Antennas. *IET Electronics Letters*, 36(5):390–391.

- Van Bladel, J. 1975. On the Resonances of a Dielectric Resonator of Very High Permittivity. *IEEE Transactions on Microwave Theory and Techniques*, 23(2):199–208.
- Van Bladel, J. 1975. The Excitation of Dielectric Resonators of Very High Permittivity. *IEEE Transactions on Microwave Theory and Techniques*, 23(2):208–217.
- Wu, B. & Hao, Y. 2014. Material Region Division and Antenna Application of Monolayer and Multilayer Graphene. *IEEE European Conference on Antennas and Propagation*, The Hague, Netherlands, 6–11 April 2014. The institute: 497–498.
- Yasin, T. & Baktur, R. 2013. Circularly polarized meshed patch antenna for small satellite application. *IEEE Antennas and Wireless Propagation Letters*, 12:1057–1060.
- Yekan, T. & Baktur, R. 2017. Conformal integrated solar panel antennas: Two effective integration methods of antennas with solar cells. *IEEE Antennas and Propagation Magazine*, 59(2):69–78.

Appendix A: Arduino Beam-Steering Sketch

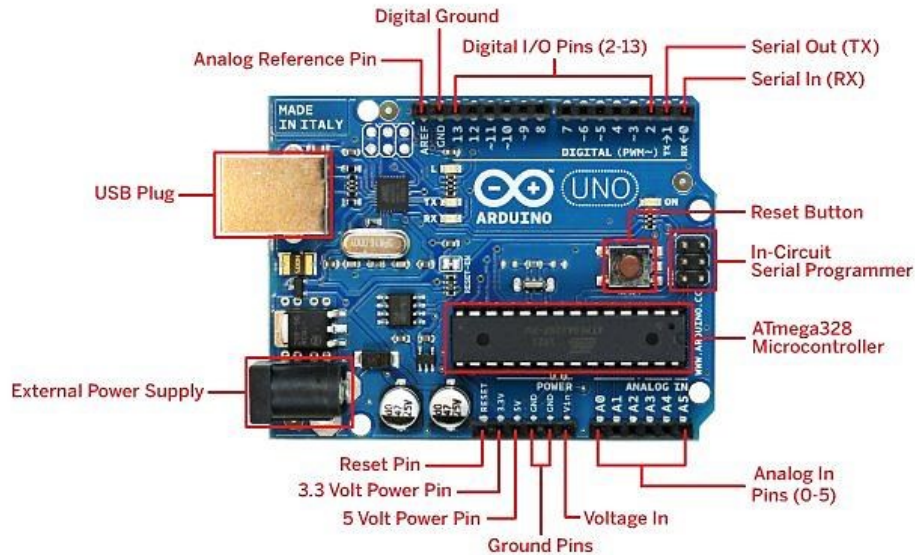


Figure A.1: Arduino UNO rev3 microcontroller board

A.1 maps_6bit

```
/* Description: This sketch address two 6-Bit digital phase shifters.
MACOM(MAPS-011008) configured in parallel mode
Phase shifter A: Beam-steering between 0 Deg <= Theta <= 90 Deg
Phase shifter B: Beam-steering between -90 Deg <= Theta <= 0 Deg
Port registers addressed directly to faster & simultaneously manipulate
the output pins. This is used in contrast to "digitalWrite" and pinMode.
PORTB address digital pins [8 to 13]
PORTD address digital pins [0 to 7]
```

```
Author: Vernon Davids
Last date modified: 04 August 2015
```

```
*/
```

```
const int baud = 9600;           // Constant and won't change (Baudrate)
int val = 0;                     // Variable that will change
int sign = 1;
int mat = 0;

byte phaseD[] = {
B00000010, // 0           deg state = 00
B00000110, // 5.625       deg state = 01
B00001010, // 11.25       deg state = 02
B00001110, // 16.875     deg state = 03
B00010010, // 22.5       deg state = 04
B00010110, // 28.125     deg state = 05
B00011010, // 33.75      deg state = 06
B00011110, // 39.375     deg state = 07
B00100010, // 45         deg state = 08
```

```

B00100110, // 50.625   deg  state = 09
B00101010, // 56.25    deg  state = 10
B00101110, // 61.875   deg  state = 11
B00110010, // 67.5     deg  state = 12
B00110110, // 73.125   deg  state = 13
B00111010, // 78.75    deg  state = 14
B00111110, // 84.375   deg  state = 15
B01000010, // 90       deg  state = 16
B01000110, // 95.625   deg  state = 17
B01001010, // 101.25   deg  state = 18
B01001110, // 106.875  deg  state = 19
B01010010, // 112.5    deg  state = 20
B01010110, // 118.125  deg  state = 21
B01011010, // 123.75   deg  state = 22
B01011110, // 129.375  deg  state = 23
B01100010, // 135      deg  state = 24
B01100110, // 140.625  deg  state = 25
B01101010, // 146.25   deg  state = 26
B01101110, // 151.875  deg  state = 27
B01110010, // 157.5    deg  state = 28
B01110110, // 163.125  deg  state = 29
B01111010, // 168.75   deg  state = 30
B01111110, // 174.375  deg  state = 31
B10000010, // 180      deg  state = 32
B10000110, // 185.625  deg  state = 33
B10001010, // 191.25   deg  state = 34
B10001110, // 196.875  deg  state = 35
B10010010, // 202.5    deg  state = 36
B10010110, // 208.125  deg  state = 37
B10011010, // 213.75   deg  state = 38
B10011110, // 219.375  deg  state = 39
B10100010, // 225      deg  state = 40
B10100110, // 230.625  deg  state = 41
B10101010, // 236.25   deg  state = 42
B10101110, // 241.875  deg  state = 43
B10110010, // 247.5    deg  state = 44
B10110110, // 253.125  deg  state = 45
B10111010, // 258.75   deg  state = 46
B10111110, // 264.375  deg  state = 47
B11000010, // 270      deg  state = 48
B11000110, // 275.625  deg  state = 49
B11001010, // 281.25   deg  state = 50
B11001110, // 286.875  deg  state = 51
B11010010, // 292.5    deg  state = 52
B11010110, // 298.125  deg  state = 53
B11011010, // 303.75   deg  state = 54
B11011110, // 309.375  deg  state = 55
B11100010, // 315      deg  state = 56
B11100110, // 320.625  deg  state = 57
B11101010, // 326.25   deg  state = 58
B11101110, // 331.875  deg  state = 59
B11110010, // 337.5    deg  state = 60
B11110110, // 343.125  deg  state = 61
B11111010, // 348.75   deg  state = 62
B11111110, // 354.375  deg  state = 63
};
byte phaseB[] = {
B00000000, // 0        deg  state = 00
B00000001, // 5.625    deg  state = 01
B00000010, // 11.25    deg  state = 02
B00000011, // 16.875   deg  state = 03
B00000100, // 22.5     deg  state = 04
B00000101, // 28.125   deg  state = 05

```

```
B00000110, // 33.75   deg  state = 06
B00000111, // 39.375  deg  state = 07
B00001000, // 45           deg  state = 08
B00001001, // 50.625      deg  state = 09
B00001010, // 56.25       deg  state = 10
B00001011, // 61.875      deg  state = 11
B00001100, // 67.5        deg  state = 12
B00001101, // 73.125      deg  state = 13
B00001110, // 78.75       deg  state = 14
B00001111, // 84.375      deg  state = 15
B00010000, // 90          deg  state = 16
B00010001, // 95.625      deg  state = 17
B00010010, // 101.25      deg  state = 18
B00010011, // 106.875     deg  state = 19
B00010100, // 112.5       deg  state = 20
B00010101, // 118.125     deg  state = 21
B00010110, // 123.75      deg  state = 22
B00010111, // 129.375     deg  state = 23
B00011000, // 135         deg  state = 24
B00011001, // 140.625     deg  state = 25
B00011010, // 146.25      deg  state = 26
B00011011, // 151.875     deg  state = 27
B00011100, // 157.5       deg  state = 28
B00011101, // 163.125     deg  state = 29
B00011110, // 168.75      deg  state = 30
B00011111, // 174.375     deg  state = 31
B00100000, // 180         deg  state = 32
B00100001, // 185.625     deg  state = 33
B00100010, // 191.25      deg  state = 34
B00100011, // 196.875     deg  state = 35
B00100100, // 202.5       deg  state = 36
B00100101, // 208.125     deg  state = 37
B00100110, // 213.75      deg  state = 38
B00100111, // 219.375     deg  state = 39
B00101000, // 225         deg  state = 40
B00101001, // 230.625     deg  state = 41
B00101010, // 236.25      deg  state = 42
B00101011, // 241.875     deg  state = 43
B00101100, // 247.5       deg  state = 44
B00101101, // 253.125     deg  state = 45
B00101110, // 258.75      deg  state = 46
B00101111, // 264.375     deg  state = 47
B00110000, // 270         deg  state = 48
B00110001, // 275.625     deg  state = 49
B00110010, // 281.25      deg  state = 50
B00110011, // 286.875     deg  state = 51
B00110100, // 292.5       deg  state = 52
B00110101, // 298.125     deg  state = 53
B00110110, // 303.75      deg  state = 54
B00110111, // 309.375     deg  state = 55
B00111000, // 315         deg  state = 56
B00111001, // 320.625     deg  state = 57
B00111010, // 326.25      deg  state = 58
B00111011, // 331.875     deg  state = 59
B00111100, // 337.5       deg  state = 60
B00111101, // 343.125     deg  state = 61
B00111110, // 348.75      deg  state = 62
B00111111, // 354.375     deg  state = 63
};
```

```

void setup()
{
  Serial.begin(baud);
  // Set Port registers D and B as outputs
  DDRD = B11111110;      // digital pins 7, 6, 5, 4, 3, 2, tx, rx
  DDRB = B00111111;      // digital pins -, -, 13, 12, 11, 10, 9, 8
}

void loop()
{
  if (Serial.available()) // Matlab or built-in serial monitor
  {
    char ch = Serial.read();

    if(ch >= '0' && ch <= '63') // If ASCII value between 0 and 63
    {
      val  =(val * 10) + (ch - '0'); // yes, accumulate the value
      mat  = val * sign ;           // set value to the accumulated value
      PORTD = B00000010;           // Set all pins low [2..7]
    }

    Else if (ch == '-') // If ASCII value between 0 and -63
    {
      sign = -1;
      mat  = val * sign ;
      PORTB = B00000000;           // Set all pins low [8...13]
    }

    else // Section for writing the phase state to specified ports
    {
      if (mat >= 0)
      {
        PORTB = phaseB[mat];      // Write to pins 8...13
      }

      else
      {
        PORTD = phaseD[abs(mat)]; // Write to pins 2...7
      }

      Serial.println(mat);
      val = 0; // reset value to 0 ready for the next sequence of digits
      sign = 1;
    }
  }
}

```